Proceedings
2011 RII LA-SiGMA Symposium

August 5, 2011
Baton Rouge, LA

Louisiana EPSCoR

Sponsored by the National Science Foundation and Louisiana Board of Regents

LA-SiGMA

Louisiana Alliance for Simulation-Guided Materials Applications

Welcome to the RII Symposium!

On behalf of Louisiana EPSCoR, I would like to welcome you to the 2011 LA EPSCoR RII LA-SiGMA Symposium. This is a great opportunity for everyone to become engaged in this trend-setting research/education initiative supported under the auspices of the National Science Foundation and the Louisiana Board of Regents. The objective of the project is to build the next generation of experimentally validated formalisms, algorithms, and codes for multiscale materials simulations; implementing them on present and next-generation supercomputers; and educating the next generation of a highly skilled workforce of materials scientists and engineers.

We are very proud of this project, a multidisciplinary initiative with participation by undergraduate/graduate students, post-doctoral researchers, and university research faculty from seven institutions across the State. I also welcome our distinguished participants and guests—individuals serving on our External Review Board, the Diversity Advisory Committee, EPSCoR Committee members, and university research administrators.

This Symposium features presentations on LA-SiGMA's achievements, a poster competition, and plenty of opportunities to network with your colleagues.

Thank you for participating in this Symposium, and I wish you all a productive and enjoyable meeting.

Michael Khonsari,
Louisiana EPSCoR Project Director and
Associate Commissioner for Sponsored Programs R&D, Louisiana Board of Regents

The research featured in this Symposium is supported by the National Science Foundation's Experimental Program to Stimulate Competitive Research (EPSCoR) under Grant No. EPS-1003897 and the Louisiana Board of Regents through its Board of Regents Support Fund.

Louisiana Board of Regents
Post Office Box 3677
Baton Rouge LA 70821-3677
225-342-4253
www.laregents.org

NSF EPSCoR Research Infrastructure Improvement (RII) Award:
2011 *LA-SiGMA* Symposium II

August 5, 2011
Thomas Jefferson Room, 1-136, Claiborne Building
1201 N. Third Street, Baton Rouge, Louisiana

Agenda

7:00 – 8:00 a.m.	Registration, Coffee & Donuts
8:00 – 8:10 a.m.	Welcoming Remarks & Introductions
8:10 – 8:30 a.m.	Overview of Project (Khonsari)
Science Drivers (SD) and CyberTools and CyberInfrastructure Group (CTCI)	
	SD/CTCI Presentations (Team presentations include 10 minute Q&A)
8:30 – 9:00 a.m.	*Electronic and Magnetic Materials* (Jarrell and Perdew)
9:00 – 9:30 a.m.	*Materials for Energy storage and Generation* (Pratt and Wick)
9:30 – 9:45 a.m.	*Break*
9:45 – 10:15 a.m.	*Biomolecular Materials* (Ashbaugh and Mobley)
10:15 – 10:45 a.m.	*Computational Tools for Multiscale Simulations* (Ramanujam)
10:45 – 11:05 a.m.	*Graphics Processing Units* (Thakur and Jarrell)
11:05 – 11:35 a.m.	*Evaluation, Assessment and Data Management* (Dunn and Stevens)
11:35 – 2:00 p.m.	Poster session - Lunch
2:00 – 2:30 p.m.	Diversity, Workforce Development, and External Engagement (Moreno, Hall, Derosa)
2:30 – 2:40 p.m.	Statewide Faculty Development (Domingue)
2:40 – 3:00 p.m.	Industrial Liaison
3:00 – 3:15 p.m.	Break
3:15 – 4:30 p.m. Simultaneous Sessions:	Breakout Sessions for SD and CTCI teams External Review Board (ERB) Deliberations Diversity Advisory Committee (DAC) Deliberations
4:30 – 5:00 p.m.	Feedback from ERB and DAC

Table of Contents

What is EPSCoR?

The Experimental Program to Stimulate Competitive Research (EPSCoR) is a federal/state partnership established in 1978 by the National Science Foundation (NSF) with the goal of stimulating sustainable improvements in the research & development (R&D) capacity of states—like Louisiana—that historically have not received significant federal R&D funding. Since its initial establishment, EPSCoR programs are now supported by seven federal agencies.

LA EPSCoR has served as the catalyst for transforming the way large-scale collaborative research is conducted in the State—from individual campuses competing for limited federal resources to one in which increased collaboration has enabled Louisiana to become more competitive for major R&D funding at the national level.

Louisiana has participated in NSF EPSCoR since 1987, and has been the recipient of several Research Infrastructure Improvement (RII) awards, culminating in the most recent award, of which the LA-SiGMA project is the major research component.

In this tightly integrated RII project, education and outreach activities are highly integrated into LA-SiGMA research component. Also included as part of our strategy is a suite of Statewide Programs for Faculty and Student Development programs that are available to all faculty members and their students and post-docs to help them become more competitive for federal funding. These include:

- Opportunities for Partnerships in Technology with Industry (OPT-IN)
- Supervised Undergraduate Research Experience (SURE)
- Pilot Funding for New Research (Pfund)
- Links with Industry, Research Centers, and National Labs (LINK)
- Travel Grants for Emerging Faculty (TGEF)
- Preliminary Planning Grants for Major Initiatives
- Planning Grants for Major Initiatives
- Grantwriting Workshops
- Faculty Expertise Database (SPINPlus, LA GENIUS, SMARTS)
- Speaking of Science (SOS) speakers' bureau

Participating Institutions

- Grambling State University
- Louisiana State University
- Louisiana Tech University
- Southern University
- Tulane University
- University of New Orleans
- Xavier University

External Review Board members

- B. Vincent McKoy, Professor of Chemistry, California Institute of Technology (ERB Chair)
- William A. Lester Jr., Professor of Chemistry, University of California, Berkeley
- Susan B. Sinnott, Professor of Materials Science and Engineering, University of Florida
- Harold Silverman, Senior Vice Provost, State University of New York System (retired)
- Valerie E. Taylor, Professor and Department Head, Computer Science, Texas A&M University

National Science Foundation EPSCoR

- Jeanne Small, NSF EPSCoR Program Director

Project Evaluators

- Cindi Dunn, Office of Educational Innovation and Evaluation - Kansas State University (external evaluator)
- Amy Hilgendorf, Office of Educational Innovation and Evaluation - Kansas State University (external evaluator)
- Judy Roth, Office of Educational Innovation and Evaluation - Kansas State University, (external evaluator)

Louisiana EPSCoR Committee members

- Les Guice (Chair), Vice President for Research, Louisiana Tech University
- Kevin Carman (Vice Chair), Dean, College of Basic Sciences, Louisiana State University
- Nicholas Altiero, Dean, College of Science and Engineering and Professor of Biomedical Engineering, Tulane University
- Diola Bagayoko, Southern University System Distinguished Professor of Physics, Southern University - Baton Rouge
- Geoffrey Cazes, Vice President, Cyber Innovation Center, Bossier City
- Henry Chu, Assistant Dean, College of Sciences and Professor, Laboratory for Internet Computing, University of Louisiana at Lafayette (DEPSCoR Representative)

- Gene D'Amour, Senior Vice President for Resource Development, Xavier University of Louisiana
- Kerry Davidson, Deputy Commissioner for Sponsored Programs, Louisiana Board of Regents
- Connie Fabré, Executive Director, Greater Baton Rouge Industry Alliance
- Robert Godke, Boyd Professor, School of Animal Sciences, LSU Agricultural Center
- Jeffrey Keller, Executive Director for Basic Research, Pennington Biomedical Research Center
- Michael Khonsari, Associate Commissioner for Sponsored Programs R&D and LA EPSCoR Project Director and Dow Chemical Endowed Chair Professor of Mechanical Engineering, Louisiana State University
- Kenneth Kratz, Director, Office of Research Services and Professor of Cell Biology and Anatomy, LSU Health Sciences Center – New Orleans (NIH IDeA Representative)
- Barry LeBlanc, President, CEO, Pamlab, L.L.C.
- Laura Levy, Associate Senior Vice President for Research and Professor of Microbiology and Immunology, Tulane University Health Sciences Center
- Sandra Roerig, Dean for Graduate Studies and Research, LSU Health Sciences Center - Shreveport
- Hilary Thompson, Professor, School of Public Health, LSU Health Sciences Center – New Orleans
- John Wefel, Professor of Physics, Louisiana State University, (NASA EPSCoR Representative)
- Scott Whittenburg, Vice Chancellor of Research and Sponsored Programs, Dean of the Graduate School, University of New Orleans
- Representative pending nomination, Louisiana Economic Development
- Mark Zappi, Dean of Engineering and Professor of Chemical Engineering, University of Louisiana at Lafayette

EPSCoR Staff

- Michael Khonsari, Project Director
- Jim Gershey, Project Administrator
- Jessica Domingue, EPSCoR Associate, Faculty Development Coordinator
- Cindy Greer, Grants and Contracts Coordinator
- Susan Jernigan, EPSCoR Associate
- Amber King, Communication Manager
- Karthik Poobalasubramanian, IT Coordinator

A Numerical Method for Simulating Hydrogen Absorption in Metal-H2 Reactors for Hydrogen Storage

Weizhong Dai, and Fei Han

Mathematics & Statistics
College of Engineering & Science
Louisiana Tech University

Abstract: We report a theoretical study on hydrogen absorption in metal-H2 reactors. In this study, we present a numerical method for simulating hydrogen absorption in a cylindrical LaNi5-H2 reactor. The method is obtained based on the modified heat and mass transfer model for the absorption of hydrogen, and its finite difference approximation in a staggered mesh. As a result, the numerical scheme is unconditionally stable and the solution is second-order accurate. Numerical results including gas and solid densities, gas velocity, gas and solid temperatures are obtained.

Keywords: Hydrogen storage, mathematical model, heat and transfer, finite difference method

1. Introduction

Hydrogen can be attained in relatively large amount at a relatively low pressure at near normal temperature in certain intermetallic alloy and under certain conditions hydride can desorb hydrogen quickly. Thus, the metal-hydrogen reaction could be a practical means of storing hydrogen. However, there are several critical issues for such way of hydrogen storage including the amount of hydrogen absorbed/desorbed, thermal stability of the hydride, hydrating/dehydrating kinetics, thermodynamic and thermophysical properties, crystal structures, surface processes like segregation, carbonization [1]. Therefore, efficient conditions to form metal alloys has been the main target for researchers.

Studying the metal-hydrogen reaction requires the knowledge of heat and mass transfer in a metal-hydrogen reactor during the absorption of hydrogen and also efficient computational tools to simulate the absorption, so that those critical parameters can be determined. There are numerous numerical and experimental studies in the literatures to study the details of hydrating/dehydrating process [1-3].

2. Mathematical model

We consider a cylindrical metal-hydride reactor as shown in Figure 1. For simplicity, we assume that the temperatures of gas and solid are the same which is local thermal equilibrium, hydrogen is an ideal gas from the thermodynamic view, the heat transfer by radiation is negligible, and hydrogen is charged with a constant pressure. As such, the differential equations governing the hydrating process are mass balance of hydrogen and metal, momentum, and energy equations.

Mass balance equations for hydrogen and solid

$$\varepsilon \frac{\partial \rho_g}{\partial t} = \frac{1}{r}\frac{\partial}{\partial r}[r\rho_g u_r + \frac{\partial}{\partial r}(\rho_g u_z)] = -\dot{m}$$

$$(1-\varepsilon)\frac{\partial \rho_s}{\partial t} = \dot{m}$$

Momentum Equation

$$\vec{V} = -\frac{K}{\mu}\overrightarrow{grad}(P)$$

Energy Equation

$$(\rho C_p)_e \frac{\partial T}{\partial t} = \frac{1}{r}\frac{\partial}{\partial r}(r\lambda_e \frac{\partial T}{\partial r}) + \frac{\partial}{\partial z}(\lambda_e \frac{\partial T}{\partial z}) - \rho_g C_{pg} u_r \frac{\partial T}{\partial r}$$
$$- \rho_g C_{pg} u_z \frac{\partial T}{\partial z} - \dot{m}[\Delta H^0 - T(C_{pg} - C_{ps})]$$

3. Numerical simulation and results

We consider a cylindrical metal-hydride reactor as shown in Fig. 1. The radius of the cylinder is 0.1 meter, and height is 0.5 meter. The radius of inlet is 0.01 meter. The staggered mesh is showen in Fig. 2.

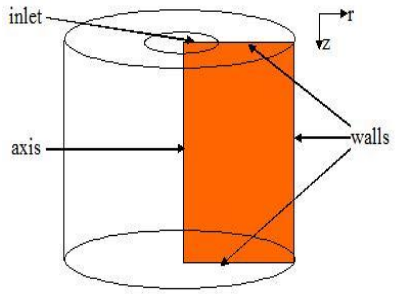

Fig 1. The considered cylindrical reactor and its two-dimensional cross-section for computation.

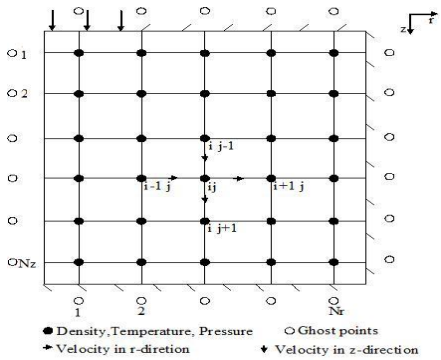

Fig 2. A staggered mesh in the computational domain.

Figure 3 shows the comparison of density of hydride, density of hydrogen gas, and temperature profiles along the line r = 0.05 m and $0 \le z \le 0.5$ m, which were obtained using three different meshes of 50 × 100, 75 × 150, and 100 × 200. It can be seen from these figures that the mesh size had no significant effect on the solution and hence the solution is considered to be grid independent and convergent.

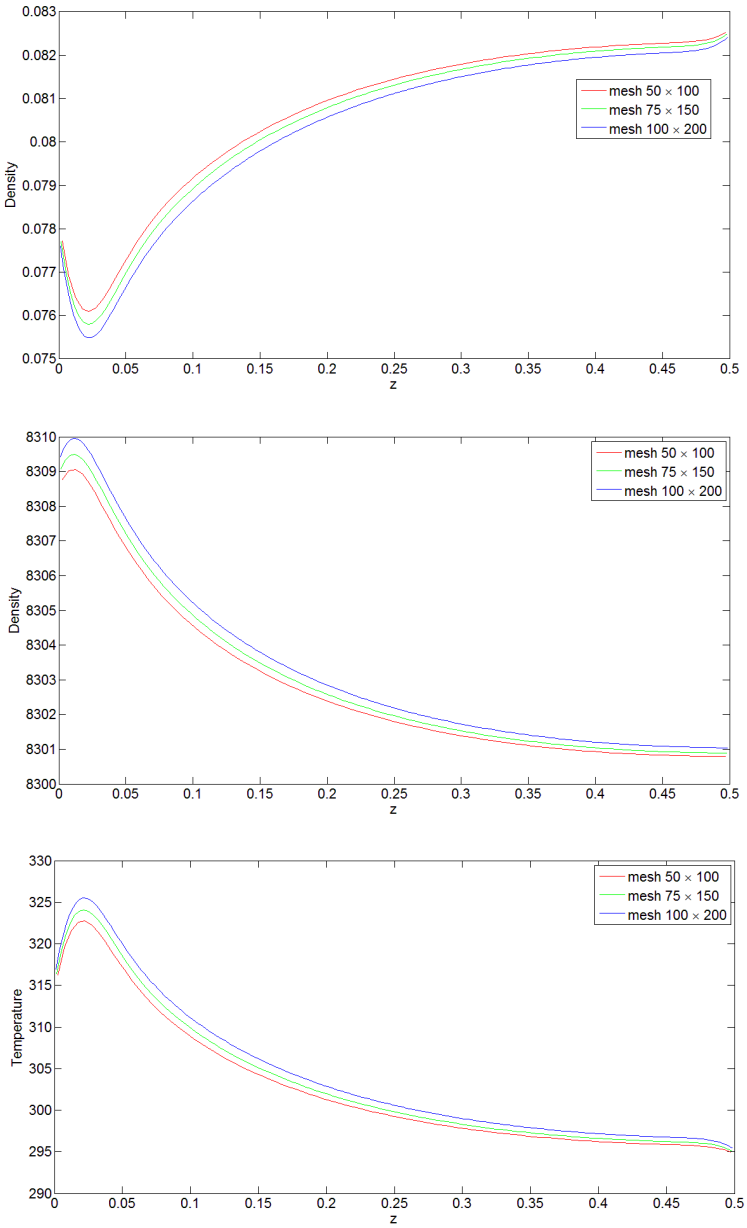

Fig 3. Comparison of (a) density of solid, (b) density of hydrogen, and (c) temperature along the line r=0.05 mm at t = 10 min, obtained using three different mesh sizes.

Fig. 4 shows contours of temperature distribution of hydride at (a) t = 10 min, (b) t = 20 min, (c) t = 30 min, (d) t = 40 min, (e) t = 50 min, and (f) t = 60 min, respectively. The maximum temperature rise is about 385 K after 1 hour, which is similar to 383 K obtained in [1]. It can be seen from the figures that the temperature rises mainly in the active reaction of hydrogen and metal.

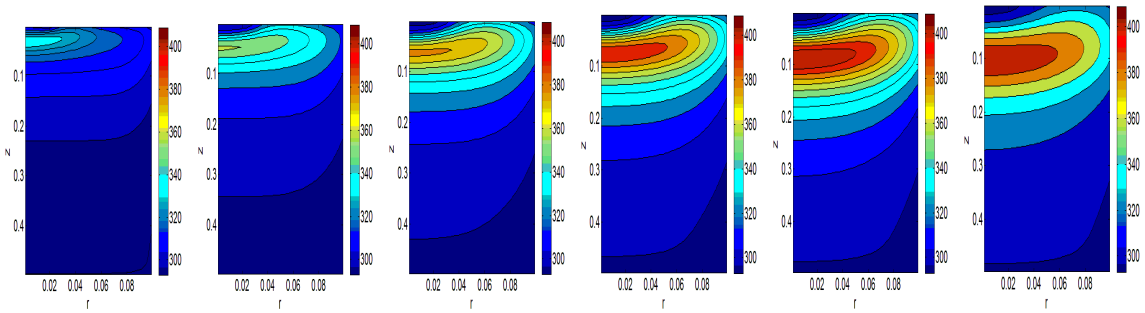

Fig. 4. Contours of temperature distribution of hydride at (a) t = 10 min, (b) t = 20 min, (c) t = 30 min, (d) t = 40 min, (e) t = 50 min, and (f) t = 60 min obtained using a mesh of 100×200.

4. Conclusion and Future Work

A second order unconditionally stable numerical scheme is developed and employed to analyze the heat and mass transfer in absorption process the metal-hydrogen tank. Further research will focus on the application of the new numerical method to develop a comprehensive computational tool including the inverse solutions to answer those critical issues mentioned in the previous section, which the current numerical methods and commercial software have not provided.

5. Acknowledgments

The current work is funded by the NSF EPSCoR Research Infrastructure Improvement (RII) Award # EPS-1003897.

6. References

[1] A. Demircan, M. Demiralp, Y. Kaplan, M. D. Mat, and T. N. Veziroglu, Experimental and theoretical analysis of hydrogen absorption in LaNi5-H2 reactors, International Journal of Hydrogen Energy, Vol. 30, pp. 1437-1446 (2005)

[2] A. Jemni and S. B. Nasrallah, Study of two-dimensional heat and mass transfer during absorption in a metal-hydrogen reactor, International Journal of Hydrogen Energy, Vol. 20, pp. 43-52 (1995)

[3] A. Jemni and S. B. Nasrallah, Study of two-dimensional heat and mass transfer during desorption in a metal-hydrogen reactor, International Journal of Hydrogen Energy, Vol. 20, pp. 881-891 (1995)

Ab-Initio and Doubly Self-Consistent Description and Prediction of Properties of Materials with Density Functional Theory (DFT)

D. Bagayoko,[1] E. C. Ekuma,[2] and L. Franklin[1]

[1]Department of Physics, Southern University and A&M College, Baton Rouge, Louisiana
[2]Department of Physics and Astronomy, Louisiana State University, Baton Rouge, Louisiana

Abstract: We present the *ab-initio*, *doubly self-consistent*, accurate, and robust description and prediction of properties of materials within the framework of density functional theory (DFT). We solve self-consistently the *system of two (2) equations* defining LDA, once a potential is chosen. The Rayleigh theorem provides a well-defined and mathematically rigorous criterion for determining the convergence of the basis set (in size and symmetry) for the description of the ground state of charge density. The calculated properties, including the band gaps, agree very well with experiment.

Keywords: Density functional theory, local density approximation, self-consistent solution of a system of equations, Rayleigh theorem, band gaps

1. Introduction

From 1964 to present, density functional theory (DFT) [1] has been the prevailing approach for the theoretical description of electronic properties of materials. In particular, following the introduction of the local density approximation (LDA) [2] in 1965, much progress has been made in constructing LDA based potentials that lend themselves to relatively simple calculations of properties of materials.

Highly encouraging results for metals [3] were followed by somewhat disappointing ones for semiconductors and insulators. Specifically, LDA potentials have led to accurate descriptions of metals while the band gaps of semiconductors and insulators have been grossly underestimated, sometimes by 30-50% or more. Explanations provided for this failure for semiconductors and insulators have included the derivative discontinuity [4-5] of the exchange correlation energy, self-interaction [6], and the neglect of non-local features of the true DFT potential as compared to LDA ones. Given that our emphasis is not on these explanations, we urge the reader to consult the pertinent review literature. *For our purposes, we underscore that while the above derivative discontinuity has been established for semiconductors and for insulators, there exists no proof that it is non-zero or non-negligible in real materials.* As for self-interaction, its correction has so far led to overestimates of band gaps of semiconductors, for the most part. The real impact of the non-local features is not settled either.

A direct consequence of the above situation for semiconductors and insulators has been the proliferation of an increasing number of schemes aimed at remedying the perceived limitations of DFT in describing semiconductors and insulators. The reader is urged to consult Bagayoko [7] for a listing of more than 10 schemes, a few of which

go beyond LDA or DFT altogether. *Several of these schemes entail adjustable parameters that preclude or diminish their predictive capability.*

The aim of this work is to describe a mathematically rigorous, physically sound, and experimentally verified method that leads to *ab-initio*, doubly self-consistent, and accurate electronic energies and related properties for atoms, molecules, clusters, nanostructures, semiconductors, and insulators.

2. Method

Our computational approach is very similar to others in two respects: The choice of an LDA potential and the use of the linear combination of atomic orbitals (LCAO). In most of our calculations, we utilized the LDA potential of Ceperley and Alder [8] as parameterized by Vosko, Wilk, and Nusair [9]. We utilize Gaussian functions to represent the radial parts of orbitals.

The key difference between our method and practices in the literature resides in the fact that we solve the system of equations defining the local density approximation. The need for solving the system of equations was clearly stated by Kohn and Sham [2]. Once a form of the LDA potential is selected, the referenced system of equations reduces to two equations:

$$\left[-\frac{1}{2}\nabla^2 + V(\vec{r}) + \int \frac{n(\vec{r}')}{|\vec{r}-\vec{r}'|}\,d\vec{r}' + V_{xc}(n(\vec{r}))\right]\psi_i(\vec{r}) = \varepsilon_i\psi_i(\vec{r}), \tag{1}$$

where $V_{xc}(n(\vec{r}))$ is a functional derivative of the exchange correlation energy with respect to the charge density $n(\vec{r})$ and

$$n(\vec{r}) = \sum_{i=1}^{N}\psi^*(\vec{r})\psi(\vec{r}), \text{ a sum over wave functions of } \textit{occupied} \text{ states only.} \tag{2}$$

In our method initially introduced by Bagayoko, Zhao, and Williams (BZW) [10], the above two equations are solved self-consistently, with the iterations for Equation (1) embedded in those of Equation (2). The iterations for the latter, for solid state calculations, start with the minimum basis set, i.e., the smallest basis set that accounts for all the electrons in the material under study. We know that the outputs of this first calculation are not correct. We perform Calculation II in which the basis set in I is augmented with one additional orbital (i.e., 2, 6, or 10 additional functions when spin and angular symmetry are accounted for). Equation (1) is solved self-consistently with this new basis set and the resulting occupied energies are compared to those from Calculation I – both numerically and graphically. In general, the two results are found to be different, indicating that the occupied energies in Calculation I had not reached their respective minima. Successive calculations are performed as described above and the occupied energies from a new calculation are compared to those of the calculation

preceding it. This process continues until one finds that Calculation (N+1) has the same occupied energies as Calculation N within the computational uncertainties (estimated to be at most 0.05 eV). Then, the outputs of Calculation N are taken as the ones describing the material under study. The basis set for Calculation N is called the *optimal basis* set [10]. Calculation (N+1) and others with larger basis sets generally lead to *unoccupied* energies lower or much lower than their corresponding ones from Calculation N, by virtue of the Rayleigh theorem, while no occupied energies from these calculations are lower than their corresponding one from Calculation N.

3. Results and Discussions

The table below succinctly shows our very recent results for work mostly funded by NSF and the Louisiana Board of Regents through LASiGMA.

	Calculation	Measurement		Calculation	Measurement
w-CdS	2.47 eV[11]	2.52 eV	zb-CdS	2.39 eV[12]	2.42 eV
w-ZnO	3.39 eV[13]	3.44eV	$NaNO_2$	3.18 eV[14]	3.14 - 3.22 eV

Calculated band gaps of selected semiconductors as compared to experimental ones

Despite the beliefs relative to perceived limitations of DFT, in general, and of LDA, in particular, the results above clearly indicate that *the physical content of doubly self-consistent LDA results* is much greater than is the case for results from single trial basis set calculation. Indeed, while not discussed here, we calculated electron effective masses, densities of states, and optical transition energies that agree with experiment for the materials shown above [11-14] and many others [7].

The success with metals is trivially explained by the fact that the absence of a gap leads to the concomitant convergence of the occupied and of the low lying unoccupied energies! For all materials with a gap (i.e., atoms, molecules, clusters, semiconductors, and insulators) the BZW method is unavoidable in obtaining the true LDA description or prediction of their properties.

4. Conclusion and Future Work

An important conclusion of this work consists of the observed fact that doubly self-consistent DFT eigenvalues have much more physical content than results from single trial basis set calculations that mostly suffer from a mathematical artifact stemming from the Raleigh Theorem. In fact, the inaccurate, unoccupied energies or bands from these calculations motivated much of the scheme development noted above. The unphysical nature of results from many single trial basis set calculations, as far as unoccupied energies are concerned, clearly appears not to apply to *true DFT or LDA eigenvalues*. LDA calculations that employ the BZW method provide *ab-initio* and accurate descriptions of materials, from molecules to solids. Further, as illustrated in the literature, they lead to first principle predictions [10] that are confirmed by experiment [7].

Clear implications of this work therefore include true molecular and band gap engineering among others. Specifically, by changing the composition of binary, ternary, and quaternary systems, one can utilize LDA-BZW calculations to inform and to guide the design and fabrication of nanostructure or semiconductor based devices.

5. Acknowledgments

Research was funded mostly by the National Science Foundation (NSF) and the Louisiana Board of Regents, through LASIGMA [Award Nos. EPS-1003897 and NSF (2010-15)-RII-SUBR] and in part by NSF (HRD 1002541), the Louisiana Optical Network Initiative (LONI, Award No. SUBR-2-10915), and NASA, through the Louisiana Space Consortium [LaSPACE, Award No. 5-27316].

6. References

[1] P. Hohenberg and W. Kohn, Phys. Rev. 136, B864 (1964).
[2] W. Kohn and L. J. Sham, Phys. Rev. 140, A1133 (1965).
[3] V. L. Moruzzi, J. F. Janak, and A. R. Williams, *Calculated Electronic Properties of Metals* (Pergamon, New York 1978).
[4] John P. Perdew and Mel Levy, Phys. Rev. Lett. 51, No. 20, 1884 (1983).
[5] L. J. Sham and M. Schlüter, Phys. Rev. Lett. 51, No. 20, 1888 (1983).
[6] J. P. Perdew and Alex Zunger, Phys. Rev. 23, No. 10, 5048 (1981).
[7] Proceedings, International Seminar on Theoretical Physics and Development, Abuja, Nigeria, August, 2008. Published in African Journal of Physics (AJP), Pages 15-35 (2009); at http://sirius-c.ncat.edu/asn/ajp/allissue/ajp-ISOTPAND/index.html
[8] D. M. Ceperley and B. J. Alder, Phys. Rev. Lett. 45, 566 (1980).
[9] S. H. Vosko, L. Wilk, and M. Nusair, Can. J. Phys. 58, 1200 (1980).
[10] D. Bagayoko, L. Franklin, G. L. Zhao, and H. Jin, J. Appl. Phys. 103, 096101(2008). See also G. L. Zhao, D. Bagayoko, and T. D. Williams. Physical Review B60, 1563, 1999 and "A Spurious Effect and LDA Prediction of the Correct Band Gap in $BaTiO_3$." D. Bagayoko, G. L. Zhao, and Troy D. Williams. Bulletin, APS, Vol. 43, No. 1, p. 846, (1998).
[11] E. C. Ekuma, L. Franklin, G. L. Zhao, J. T. Wang, and D. Bagayoko, Can. J. Phys. 89 (3), pg. 319-324 (March 2011).
[12] E. C. Ekuma, L. Franklin, G. L. Zhao, J. T. Wang, and D. Bagayoko, Physica B406, 1477 (2011).
[13] Manuscript under preparation [Available from the Bagayoko, Diola_bagayoko@subr.edu).
[14] MS Thesis of Mr. E. C. Ekuma, Department of Physics, Southern University and A&M College in Baton Rouge (SUBR), Baton Rouge, Louisiana, 70813.

Ab Initio Density Functional Theory Simulation on O_2 Molecule Adsorption on Nitrogen Edge-Saturated (10, 0) Carbon Nanotubes

Lei Zhao[1], Shizhong Yang[1], Guang-Lin Zhao[2], Shengmin Guo[3], and Diola Bagayoko[2]

[1]Department of Computer Science, Southern University and A & M College, Baton Rouge, LA70813
[2]Department of Physics, Southern University and A & M College, Baton Rouge, LA70813
[3]Department of Mechanical Engineering, Louisiana State University, Baton Rouge, LA70803

Abstract: We performed first principles spin polarized density functional theory (DFT) calculations to simulate the 10 nitrogen atoms doped at the first layer of carbon nanotubes (CNT) for dioxygen adsorption and reduction. CNTs have significant properties as catalyst in the fuel cell cathodes with nitrogen atoms doped at CNT's fringe. The bulk of rhombic N/CNT system is investigated using the Vienna Ab-initio Simulation Package (VASP) with local-density approximation (LDA) method. We also study the effect of N/CNT system on oxygen molecule reduction.

Keywords: CNT, nitrogen edge-saturated, DFT simulation

1. Introduction

Carbon nanotubes (CNT) are allotropes of carbon with a cylindrical nanostructure. The cylindrical carbon molecules have unusual properties, which are valuable for nanotechnology, electronics, optics and other fields of materials science and technology. In this work, we studied the CNT based structure as catalyst which is used for the oxygen reduction reaction (ORR) in the fuel cell cathodes. Precious platinum (Pt) catalyst is a key ingredient in fuel cells which produce electricity and water as the only byproduct from a hydrogen fuel[i]. Because of the expensive cost of Platinum, reducing the amount of Pt loading by introducing new catalysts is one of the major targets in the current research. In 2006, Ozkan and co-workers found that nitrogen-containing CNT have promising catalytic activity toward ORR [ii, iii]. In 2008, Yang and co-workers reported that the vertically aligned CNT arrays, which are functionalized through nitrogen and iron doping by a chemical vapor deposition (CVD) process, can be electrocatalytically active toward ORR [iv]. The functionalized CNT show promise properties as an alternative non-Pt electrocatalyst with a unique nanoarchitecture and advantageous materials properties for the cathode of polymer electrolyte membrane fuel cell (PEMFC).

2. Computation Method

In this work, we mainly focused on computer-based simulation. In our DFT calculations, the electronic structure properties of the nitrogen doped CNT system are studied. We used local-density approximation (LDA) in our simulation. The simulation is based on the Vienna Ab-initio Simulation Package (VASP) with the plane wave projector augmented wave (PAW) method[v, vi] basis set. In all of our calculations, the plane wave energy cutoff is fixed at 500eV. Short pieces of (10, 0) CNTs with 16 atomic rings (10 carbon atoms per ring) are included in the

simulations. We built the N/CNT model via replacing all carbon atoms at the first layer by nitrogen atoms. To achieve the representative condition of the N/CNT structure, a rhombic supercell consisting of 150 C atoms and 10 N atoms is set as 16.97 Å × 16.97 Å × 24.90 Å with the vacuum space separations between CNTs on the sides and along the tube axis direction larger than 9 Å in the simulations, which is large enough to ignore the periodic boundary condition effect. One atom which is very close to (0, 0, 0) is fixed and the rest of atoms are fully relaxed around the fixed atom in the DFT calculations. After relaxation and optimization of N/CNT system, we put one oxygen molecule up on N atoms at difference positions. The oxidation reduction of oxygen molecule at N/CNT catalyst substrate.

3. Results and Discussion

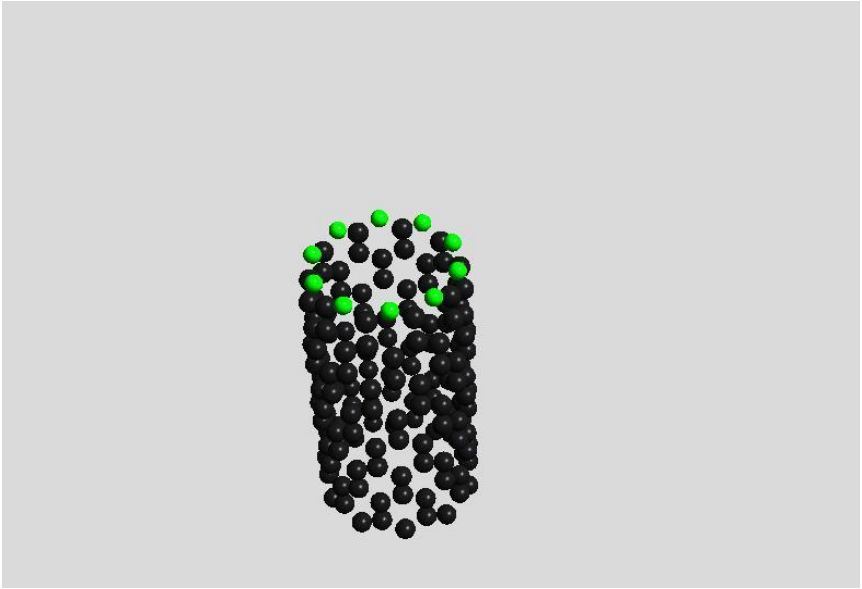

Figure 1. Nitrogen edge saturated (10, 0) CNT. The green balls stand for N atoms, the black balls stand for C atoms.

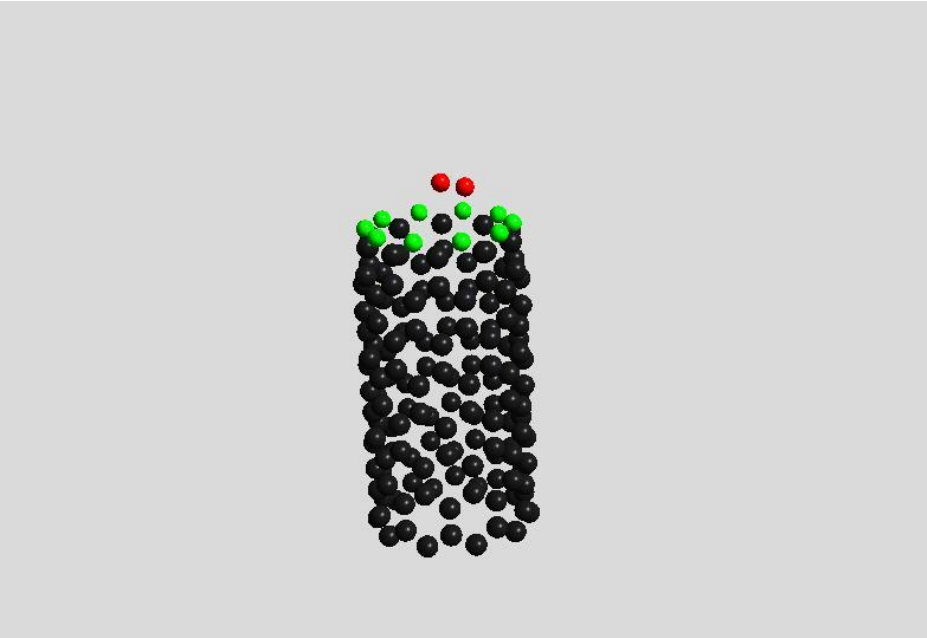

Figure 2.Oxygen molecule adsorption on (10, 0) N/CNT system. The red balls stand for O atoms, the green atoms stand for N atoms and the black atoms stand for C atoms.

Table I. The atomic distance and Bader charge of the nitrogen edge saturated (10, 0) CNT and O_2 adsorption on nitrogen edge saturated (10, 0) CNT. Q_C is the charge transfer of C atoms bonding with corresponding N atoms. The distances are in Å while the charges are in |e|, the positive number means losing electron while negative number shows gaining electron.

	$d_{N-C(}$Å)	d_{O-N}(Å)	d_{O-O}(Å)	Q_C	Q_N	Q_O
N/CNT	1.34	N/A	N/A	2.7	-2.7 ~ -2.8	N/A
O2/N/CNT	1.34	2.58	1.21	2.7~2.8	-2.7 ~ -2.8	0.06

Our simulation results are shown in Figs. 1 and 2 and Table I. Figure 1 shows the geometry structure of optimized nitrogen edge saturated (10, 0) CNT. The edge C atoms and N atoms are aligned with the other wall C atoms. No

contraction is observed in the optimized structure. This is different from the unsaturated (10, 0) CNT case, where both edges are contracted in the optimized structure. The O-O bond is in parallel with the N atom layer and with a slant angle (~ 45°) deflection from the tangential direction of the N/CNT side wall. Figure 2 shows that O_2 molecule is adsorbed on (10,0) N/CNT. From Table I, we have the distance between O and N is 2.58 Å and the charge transfer is 0.06, small enough to be ignorable, which show the physical adsorption property. The C atoms bonding with N atoms basically lose 2.7 ~ 2.8 |e| in O_2 adsorption. The N atoms gain 2.7 ~ 2.8 |e| from C the bonding atoms.

4. Conclusion

We have performed *ab initio* DFT simulation on (10, 0) N/CNT system and O_2 molecule adsorption on (10, 0) N/CNT. The O_2-N/CNT distance is about 2.6 Å. The O_2/N/CNT system is basically physical adsorption. Thus fully saturated N/CNT would be chemically non-active for the ORR process.

5. Acknowledgement:

This work is supported in part by the NSF-LASiGMA program (grant number #EPS-1003897), the LaSPACE/NASA (grant number NNG05GH22H), DOE award No. DE-FE0004734 and DE-FE0003693, and the LONI institute.

6. References:

1. [ˇ] Subramani, V.; Gangwal, S. K. Energy Fuels 22, 814 (2008).
2. [ˇ] Matter, P. H.; Ozkan, U. S. Catal. Lett. 109, 115 (2006).
3. [ˇ] Matter, P. H.; Zhang, L.; Ozkan, U. S. J. Catal. 239, 83 (2006).
4. [ˇ] Yang, J.; Liu, D. J.; Kariuki, N. N.; Chen, L. X. Chem. Commun 3, 329 (2008).
5. [ˇ] Blo¨chl, P. E. Phys. ReV. B 50, 17953 (1994).
6. [ˇ] Kreese, G.; Hafner, J. Phys. ReV. B 59, 1758 (1999).

Ab Initio Molecular Dynamics Simulation of an Uncharged Propylene Carbonate-filled Nanotube Forest

G. G. Hoffman[1] and L. R. Pratt[1]

[1]Department of Chemical & Biomolecular Engineering, Tulane University

Abstract: *Ab initio* molecular dynamics simulation of propylene carbonate in a nanotube forest shows that this filling depends sensitively on attractive dispersion interactions not satisfactorily described by standard electron density functional models. Empirical dispersion-corrected models are evidently required and those simulations are presently underway.

Keywords: propylene carbonate, AIMD simulation, nanotube forest

1. Introduction

Effective electrical energy storage materials --- batteries and capacitors --- are necessary components for systematic exploitation of carbon-neutral renewable energy resources that are intermittent, *e.g.,* solar and wind, and for regenerative energy capture from the repetitive motion of cranes, forklifts, or braking of vehicles. Recently proposed electric double-layer capacitors (EDLCs) with electrodes of aligned, single-wall carbon nanotubes can have capacitances exceeding those of conventional EDLCs.[1-3] They offer possibilities for deliberate nanoscale mechanical and chemical design. The natural goal for such capacitors would be to achieve energy densities comparable to those of current battery systems, but also to retain the traditional advantages of capacitors, namely faster response and longer cycle lifetimes.[4]

An important start in developing a molecular understanding of EDCLs based on nanotube forests has been made on the basis of classical molecular simulations.[4] Nevertheless, some characteristics of particular interest are intrinsically quantum mechanical in nature; chemical damage and *quantum* (or more properly *intrinsic*) capacitances[5] are examples of such characteristics. *Ab initio* molecular dynamics (AIMD) are thus an essential step in the development of a molecular understanding of these systems.

AIMD calculations treat electronic structure of materials on-the-fly, within molecular dynamics simulations. They are feasible for condensed matter simulation on the basis of three enabling theoretical ingredients: (i) electron density functional theory, (ii) pseudo potentials that permit the calculation to focus only on outer, *e.g.,* valence, electrons, and (iii) suitability of plane wave basis sets for dense matter simulation. AIMD calculations are several orders-of-magnitude more demanding than molecular simulations based on model classical force-fields. For computational studies of EDCLs based on nanotube forests, which require consideration of several distinct length scales, several distinct varieties of simulation calculations have to be used in concert. Results specifically of on-going classic simulation work on these systems are reported elsewhere in this Proceedings.[6]

2. Methods

Our AIMD calculations used the CPMD package (http://www.cpmd.org/), with the PBE electron density functional model, a norm-conserving pseudo-potential (NCPP), and a plane-wave basis set cut-off of 85 Ry.[7]

To assist in understanding the organization of our calculation, Figure 1 gives a typical geometry of the system simulated. Periodic boundary conditions in all three spatial dimensions includes one 80-carbon-atom nanotube (with the implied images), 10 (13 atom) propylene carbonate molecules, 210 atoms in total. This is huge on the now-conventional electronic structure size-scale, but small on the now-conventional simulation size-scale. It is not feasible with present algorithms and equipment to treat seriously larger systems by naïve simulation, and even for this size system customary thermal aging with classic molecular simulation is not a serious possibility.

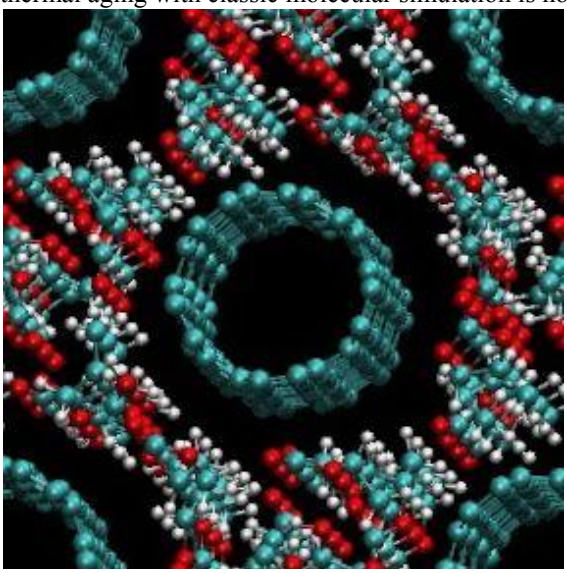

Figure 1: Configuration of the propylene carbonate-filled nanotube forest, the subject of the AIMD simulation discussed here. Four primitive images are shown here.

Because of these difficulties, we evolved a more complicated simulation protocol that is analogous to the parallel tempering algorithm,[8] now a standard feature of non-AIMD calculations. We first carried-out a standard AIMD trajectory for Δt=16ps at the high temperature of T=600K. That should permit physically-appropriate randomization of an initial configuration. From the Δt=16ps trajectory, 16 configurations were sampled uniformly. Each of those 16 configurations seeded an AIMD trajectory which was first thermal zed for 6ps at T=300K (the temperature of interest), then extended for another 6ps. Our primary analysis here utilized 12 configurations sampled uniformly from each of those last 6ps trajectories. The goal of this procedure is to obtain statistically independent structural observations. We are unaware of alternatives that might be feasible for calculations of this AIMD difficulty.

The analysis of first interest here is based on the binding energies defined by

$$\varepsilon = U(n) - U(n-1) - U(1)\,. \tag{1}$$

The distribution of binding energies ε provides the free energy of the fluid on the basis of the partition (thermal Green's) function formula

$$\exp(\beta\mu^{(ex)}) = \langle \exp(\beta\varepsilon) \rangle\,. \tag{2}$$

$\mu^{(ex)}$ is the interaction part of the partial molar Gibbs free energy of the PC fluid; the brackets indicate the thermal average. Since there can be ten (the number of PC molecules) observations of a binding energy for each configuration, this data collection scheme produces 10x12x16=1920 elementary data.

Though the natural place to start fuller statistical analyses, direct use of Eq. (2) is never naïvely successful. One example of a further analysis of this relation is the Tchebysheff bound[9]

$$\exp(\beta\mu^{(ex)}) > \exp(\beta\varepsilon)\left(1-\int_{-\infty}^{\varepsilon} p(\varepsilon')d\varepsilon'\right). \quad (3)$$

Again, this relation is not satisfactory by itself but is one element of a holistic analysis.

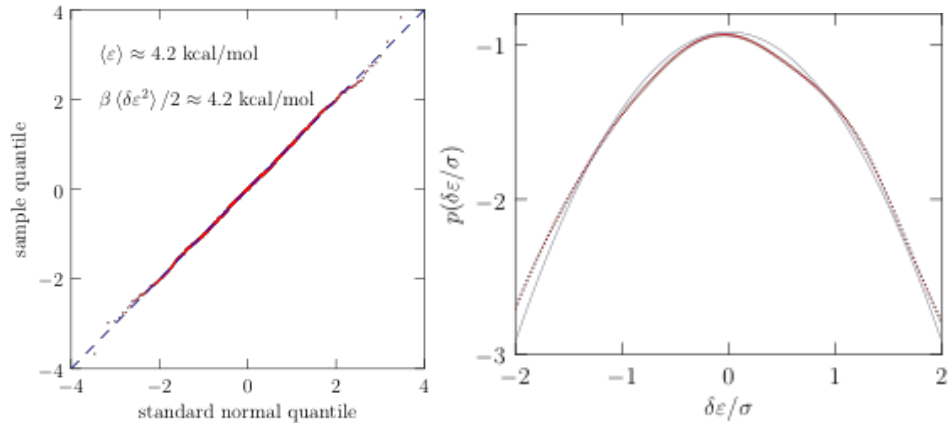

Figure 2: Distribution of binding energies. (left) The normal QQ (quantile-quantile) plot indicates that the binding energies are distributed approximately normally. (right) The Gaussian probability density of ε gives an additional, rougher indication of that point.

3. Results

The binding energies are positive and normally (Gaussian) distributed (Figure 2). Consistent with the lower bound Eq. (3) (Figure 3), this indicates that free energy for PC-filling of the nanotube forest is positive. Thus the description of attractive dispersion interactions in electron density functionals such as PBE is not satisfactorily accurate to describe the PC-filling of this nanotube forest. A simple experimental observation clinches this conclusion: the observed contact angle (37°) of PC droplets on graphite is low, indicating healthy attractive interactions between PC and graphite, and effective PC-filling of nanotube forests.[5]

4. Conclusions

Ab initio molecular dynamics simulation of propylene carbonate in a nanotube forest shows that this filling depends sensitively on attractive dispersion interactions not satisfactorily described by standard electron density functional models. Empirical dispersion-corrected models are evidently required and those simulations are presently underway (PBE-D on Kraken with teragrid support).

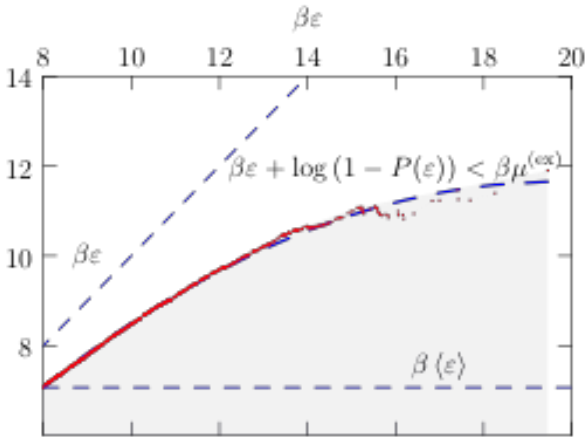

Figure 3: Tchebysheff bound on the free energy of PC-filling of the nanotube forest (the red curve), a positive value.

5. Acknowledgments

The current work is funded by the NSF EPSCoR LA-SiGMA project under award #EPS-1003897.

6. References

[1] D. N. Futaba, K. Hata, T. Namai, T. Yamada, K. Mizuno, Y. Hayamizu, M. Yumura, S. Iijima, *J. Phys. Chem. B* 110, 8035–8038 (2006).

[2] D. N. Futaba, K. Hata, T . Yamada, T. Hiraoka, Y . Hayamizu, Y. Kakudate, O. Tanaike, H. Hatori, M. Yumura, S. Iijima *Nat. Mater.* 5, 987–994 (2006).

[3] K. Hata, D. N. Futaba, K. Mizuno, T. Namai, M. Yumura, S. Iijima *Science* 306, 1362–1364 (2004).

[4] L. Yang, B. H. Fishbine, A. Migliori, and L. R. Pratt, *J. Am. Chem. Soc.* 131, 12373—12376 (2009)

[5] G. G. Hoffman and L. R. Pratt, "The intrinsic capacitance of two-dimensional electron gases" elsewhere in these Proceedings.

[6] G. G. Hoffman, R. Mariano, N. Pesika, L. R. Pratt, S. W. Rick, X. You, "Simulation of Propylene Carbonate as a Solvent for Electrochemical Double-layer Capacitors" elsewhere in these Proceedings.

[7] Other AIMD simulation codes are publically available, *e.g., Quantum Espresso* (http://www.quantum-espresso.org/). A limited amount of comparative testing persuaded us the CPMD was the most appropriate choice for us at the present time. We expect that comparative testing to continue.

[8] D. J. Earl, and M. W. Deem, "Parallel tempering: Theory, applications, and new perspectives," *Phys. Chem. Chem. Phys.* 7, 3910—3916 (2005).

[9] D. Asthagiri and L. R. Pratt, "Potential Distribution Methods and Free Energy Models of Molecular Solutions", FREE ENERGY CALCULATIONS, THEORY AND APPLICATIONS IN CHEMISTRY AND BIOLOGY, C. Chipot, and A. Pohorille (Eds.), (Springer, 2007)

Ab Initio Study of Iron Oxide Clusters and their Reactions with Phenol, 2-Chlorophenol and 4-Chlorophenol

Cheri A. McFerrin[1], Barry Dellinger[1], and Randall W. Hall[1]
Ramu Ramachandran[2] and Collin Wick[2]

[1]Department of Chemistry, Louisiana State University
[2] Department of Chemistry, Louisiana Tech University

Abstract: *Ab initio* calculations were used to study the structures and spin states of neutral iron oxide clusters, Fe_nO_n and Fe_nO_{n+1} (n=1-4). The lowest energy structures of these neutral clusters were determined using both all-electron and effective core potential basis sets and the M06 and the BPW91 density functionals. To model surface reactions on iron oxide nanoparticles, each cluster was hydroxylated followed by reaction with phenol, 2-chlorophenol and 4-chlorophenol. Reaction energies were used to determine the most likely reaction sites and Bader charge analyses were used to correlate reactivity with partial charge on iron atoms. These studies will be used as part of LA-SiGMA's Science Driver 2 to validate and direct the development of force fields capable of studying the structure of larger metal oxide particles.

Keywords: Nanoparticles, catalysts, reaction thermodynamics, charge distributions.

1. Introduction

Copper and iron oxide nanostructured particles have been shown to be particularly effective catalysts for the formation of polychlorinated dibenzo-*p*-dioxins and dibenzofurans (PCDD/F) and other pollutants during combustion processes[1]. Environmentally persistent free radicals form on combustion produced copper and iron oxide-containing nanoparticles, and these radicals have been shown to be intermediates in the formation of PCDD/F and be a possible cause of the observed health impacts of airborne fine particles.[2-6] It has been shown that the metal atoms in these nanoparticles facilitate the formation of radicals via electron transfer from a physisorbed molecular precursor to a metal atom in the cluster.[7] For this reason, we are studying the structures and reactivities of iron oxide clusters. This involves accurate density functional calculations and the development of force fields capable of allowing calculations involving metal oxide clusters containing tens to hundreds of metal atoms. LA-SiGMA's focus on accurate density functionals and force fields is a critical component of understanding the mechanism for metal oxide catalysis of PCDD/Fs.

There are relatively few experimental and theoretical studies of how copper and iron oxide clusters catalyze or mediate the formation of pollutants in combustion systems or the environment. Estimates of the relevant cluster sizes range from a micrometer down to just a few metal atoms; therefore, this work studies the structures and energetics of small iron oxide clusters as a first step toward understanding the interactions between metal oxides and free radicals.[7]

2. Methods

An all-electron basis set (6-311+G*) and one coupled to an effective core potential (LanL2DZ) along with two density functionals (M06 and BPW91) were used in these studies. Calculations were compared, where possible, to previous work on iron oxide clusters.[8] Our procedure studied the catalytic process in three steps. First the structures and energetics of Fe_nO_n and Fe_nO_{n+1} clusters (n=1-4) were determined in order to find the lowest energy spin states. Second, since water is ubiquitous in the environment, it is expected to hydroxylate the surface of metal oxide clusters; to model this, a water molecule was added in turn to each unique iron atom in a cluster with the lowest spin state. For example, there are two non-equivalent Fe atoms in Fe_2O_3. In this particular case addition of water to the more positively charged, 3-coordinate Fe atom is favored. Addition of water typically resulted in the formation of an O-H bond and the transfer of a hydrogen atom to an adjacent oxygen atom forming another O-H bond. Finally, phenol and substituted phenols were added to the hydroxylated cluster and the reaction products (water and a phenoxylated cluster) analyzed for reaction energetics and charge/spin distribution. Preliminary results for the addition of these molecular precursors indicate the number of oxygen atoms in a metal oxide cluster is directly proportional to the exothermicity of the reaction (Table 2). It has already been experimentally shown the electron affinity of the neutral iron oxide clusters increases with the number of oxygen atoms.[9]

3. Results

Figure 1 displays the optimized iron oxide clusters found using the M06/LanL2DZ model chemistry. The larger clusters are nonplanar and the coordination at the iron atoms ranges from 1-3. Table 1 displays the lowest energy spin state for each cluster for the M06 and BPW91 density functionals with the LanL2DZ ECP basis set and the 6-311+G* all-electron basis set. There is disagreement between the two functionals for the lowest energy spin state, but the geometries are similar for all model chemistries studied.

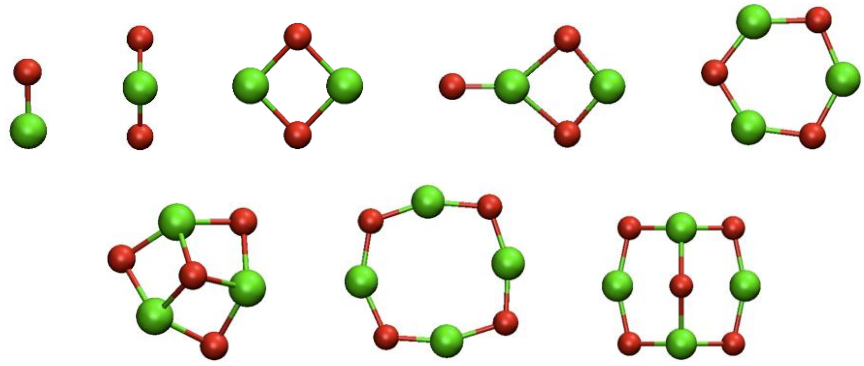

Figure 1. M06/LanL2DZ optimized clusters of Fe_nO_n and Fe_nO_{n+1}, n=1,4. Fe atoms are green; O atoms are red. The larger clusters are not planar.

Figure 2 displays the hydroxylated Fe_2O_3 cluster after migration one of the hydrogen atoms from the added water to one of the oxygen atoms of the cluster. Figure 3 displays the reaction products for the cluster shown in Figure 2 with phenol, *o*-chlorophenol, and *p*-chlorophenol. Table 2 displays the ΔE_{rxn}

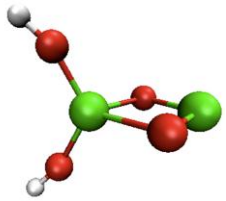

Figure 2: M06/LanL2DZ optimized cluster of Fe_2O_3 after hydroxylation and H atom migration. Fe atoms are green; O atoms are red; H atoms are white.

and the change in the Bader charge of the iron atom at which the phenol or chlorinated phenol attaches to the metal oxide cluster.

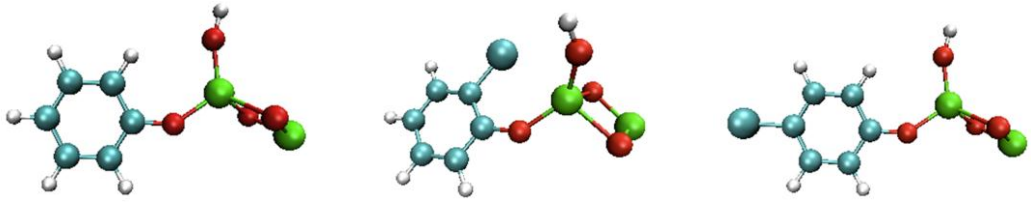

Figure 3. Reaction products of hydroxylated Fe_2O_3 with phenol, *o*-chlorophenol, and *p*-chlorophenol. Fe atoms are green; O atoms are red; H atoms are white; C atoms are light cyan; Cl atoms are dark cyan.

Table 1: Lowest energy spin state for iron oxide clusters vs. several model chemistries.

Cluster	M06/LanL2DZ	M06/6-311+G*	BPW91/LanL2DZ	BPW91/6-311+G*
FeO	5	5	5	5
FeO_2	5	5	3	3
Fe_2O_2	9	9	7	7
Fe_2O_3	11	9	7	9
Fe_3O_3	13	13	13	13
Fe_3O_4	15	In-progress	13	13
Fe_4O_4	17	In-progress	In-progress	15
Fe_4O_5	19	In-progress	In-progress	17

Table 2: Change in the Bader charge (ΔC) of the most reactive iron atom in a hydroxylated metal oxide cluster upon the addition of different free radical precursors. Energy of reaction (ΔE) in kcal-mole^{-1} between hydroxylated iron clusters and phenol (M06/LanL2DZ).

Cluster	ΔC (phenol)	ΔC (2-chlorophenol)	ΔC (4-chlorophenol)	ΔE
FeO	+.02	+.03	+.03	-1.0
FeO_2	-.03	-.03	-.02	-3.4
Fe_2O_2	-.02	+.03	-0.1	-2.3
Fe_2O_3	-.05	-.03	-.05	-3.7

Fe_3O_3	In-progress	-.10	-.05	In-progress
Fe_3O_4	+.03	+.01	+.04	-3.1
Fe_4O_4	-.03	-.27	In-progress	-1.9
Fe_4O_5	-.05	-.01	-.04	-3.2

4. Conclusion

Preliminary results for the addition of a molecular precursor to a hydroxylated cluster reveals the ΔE_{rxn} of reaction for a hydroxylated cluster with phenol or a chlorinated phenol is proportional to the number of oxygen atoms in the metal oxide cluster (Table 2). The change in Bader charges (Table 2) indicate the metal atoms at the reaction sites are, with two exceptions, slightly reduced with the addition of a radical precursor, in agreement with our hypothesis. For the case of Fe_4O_4 and 2-chlorophenol, the degree of reduction to the reactive metal center is significantly increased. This is a result of the oxidation a vicinal Fe atom (by the *o*-chlorine) as the cluster size has become large enough for secondary attractions to take place. The Bader results indicate the molecular precursors are transferring some of their electron density to the metal center resulting in a "surface-bound" radical species. It also appears the presence of an *o*-chlorine atom (in 2-chlorophenol) affects the degree of reduction, a result of the attraction between the *o*-chlorine and a vicinal Fe atom. While there is disagreement between different density functionals as to the exact spin state of some of the clusters, the calculated geometries are fairly independent of the particular functional.

5. Acknowledgments

This work supported by NSF Award Number EPS-1003897, the Louisiana Optical Network Initiative (LONI) and the LSU Center for Computational Technology. We also gratefully acknowledge helpful discussions with Dr. Gennady Gutsev.

6. References

1. Ryan, S., Wikstrom, E., Gullett, B. K., Touati, A.; Organohalogen Compd., 2004, 66, 1119-1125.
2. Dellinger, B., Pryor, W., Cueto, R., Squadrito, G., Hedge, V., Deutsch, W.; Chem. Res. Toxicol., 2001, 14, 1371-1377.
3. Dellinger, B., Pryor, W., Cueto, R., Squadrito, G., Deutsch, W.; Proc. Combust. Inst., 2000, 28, 2675-2681.
4. Shi, T., Knaapen, A., Begerow, J., Birmili, W., Borm, P., Schins, R.; Occup. Environ. Med., 2003, 60, 315-321.
5. Li, N., Sioutas, C., Cho, A., Schmitz, D., Misra, C., Sempf, J., Wang, M., Oberley, T., Froines, J., Nel, A.; Environ. Health Perspect., 2003, 111, 455-460.
6. Balakrishna, S. ; Lomnicki, S.; McAvey, K. M.; Cole, R. B.; Dellinger, B.; Cormier, S. A,; Part. Fibre Toxicol., 2009, 6, 11.
7. Vejerano, E.; Lomnicki, S.; Dellinger, B.; Environ. Sci. Tech., 2011, 45 (2), 589-594.
8. Gutsev, G. L., Khanna, S. N., Rao, B. K., Jena, P.; J. Phys. Chem. A, 1999, 103, 5812-5822.
9. Wang, L., Wu, H.; Desai, S. R.; Phys. Rev. Lett., 1996, 76 (25), 4853-4856.

Bio-Inspired Self-Healing Composites for Pressurized Gaseous Energy Storage and Transportation

Guoqiang Li[1,2] and Jones Nji[2]
[1]Department of Mechanical Engineering, Southern University, Baton Rouge, LA 70813
[2]Department of Mechanical Engineering, Louisiana State University, Baton Rouge, LA 70803

Abstract: This study investigated the effect of thermoplastic content on the self-healing efficiency of a particulate shape memory polymer (SMP) composite per the bio-inspired close-then-heal (CTH) self-healing scheme [10]. The purpose is to achieve structural-length scale healing with minimal sacrifice in structural capacity. This scheme was validated in our previous study with 6% by volume of thermoplastic content [1]. In this study, healing efficiency was evaluated at two additional thermoplastic volume fractions, 3% and 9%. Healing efficiencies of 50% and 75% were respectively achieved based on peak loads of completely fractured and healed single edged notch bend (SENB) specimens. While the increase in healing efficiency with thermoplastic content is obvious, the maximum gain in recovered load carrying capacity for the healed specimens was observed at 6% thermoplastic content. Analysis by Fourier transform infrared (FTIR) verified that the interaction between the thermoplastic additives and the SMP matrix is physical. The self-healing system has a potential to be used in the storage and transportation of pressured natural gas or hydrogen.

Keywords: Functional composites, Smart materials, Self-healing, Energy

1. Introduction

Fiber reinforced polymer (FRP) composite materials have been widely used in energy storage and transportation such as pipeline, pressure vessel, offshore oil drilling platform, riser, casing, etc., primarily due to their high specific strength/stiffness and corrosion resistance. However, excessive pressure and accidental loading may cause leaking of explosive gases such as natural gas, hydrogen, etc. If not taking care of *in situ* and in-time, the leaked gas may cause violent explosion such as the recent Gulf Oil Spill and natural gas pipeline explosion in San Francisco, California. If the natural gas pipeline and composite riser had self-healing capability, the environmental disaster, the violent explosion, and the loss of lives in the Gulf of Mexico and San Francisco would have been avoided. In addition to the storage and transportation of pressurized natural gas, hydrogen economy is one of the ultimate solutions to the nation's dependence on foreign oil, increase in greenhouse gases and global warming threats. Owing to hydrogen embrittlement, however, the existing 300,000 miles of traditional carbon steel pipelines cannot be used for hydrogen transportation. Lighter, stronger, safer, and smarter materials are urgently needed. Again, fiber reinforced polymer (FRP) composite is a viable alternative due to its inherent lightweight, corrosion resistance, and superior structural capacity. However, because hydrogen has a very low energy density, very high pressure (in excess of 100MPa for bulk storage and 14MPa for pipeline transportation) is needed in order to be economically competitive. The high pressure is a potential source for hydrogen leaking and subsequent explosion. Therefore, it is highly desired that the pipeline or storage tank can self-detect any leaking or damage and heal the damage autonomously. Self-healing technology has enjoyed continuously increasing interest in the scientific community in recent years. Since 2001, self-healing using microcapsules [2]

and hollow fiber [3] has been investigated. The liquid healing agent stored in the micro chamber can flow out after rupture of the container by the propagating crack and can heal the micro crack autonomously. However, these methods can only heal for one time. Microvascular system [4] has been developed which is capable of healing more than one time. However, this method is complex to fabricate and operate. Other methods, which need external triggering, have been explored such as thermoplastic particles (TP) [5], thermally reversible covalent bond [6], and ionomers [7]. These methods can heal cracks repeatedly. However, they, similar to the microcapsule and hollow fiber methods, are limited when they are used to heal large, macroscopic cracks. In order to repeatedly heal structural-length scale damage, a biomimetic two-step close-then-heal (CTH) scheme has been proposed by Li and Nettles [8] and Xu and Li [9], and fully explained by Li and Uppu [10]. In this approach, the macroscopic crack is first narrowed or closed through confined shape recovery of shape memory polymer matrix and then other self-healing mechanisms such as thermoplastic particles are activated to achieve molecular length-scale healing. It has been proved that the first step alone can repeatedly heal impact damage [11]. It has also been validated that external confinement can be realized in composite structures through grid stiffened composites or 3-D woven fabric reinforcement [12-14]. Also, by incorporation of thermoplastic particles in the shape memory polymer matrix, it is validated that the system can heal structural-length scale damage repeatedly, efficiently, timely, and molecularly [1]. As indicated by Li and Uppu [10], the key of using confined shape recovery for the purposes of closing macroscopic cracks is to reduce the volume during programming or training and providing external confinement during shape recovery. As discussed above, external confinement can be achieved by architectural design of structures [12-14]. For programming, it usually requires a lengthy and cost-ineffective process including several steps: heating above the transition temperature of the SMP, applying prestress or prestrain, cooling to well below the transition temperature while holding the prestress or prestrain constant, and removing the prestress [8]. Most recently, it has been found that programming or training does not necessarily need to be at temperatures above the transition temperature. It can be completed at a constant temperature well below the transition temperature, as long as the prestrain is higher than the yielding strain of the SMP. Testing and constitutive modeling suggest that this is a very fast and cost-effective method [15]. The objective of this study is to investigate the effect of the content of thermoplastic particles on the self-healing efficiency of the bio-inspired self-healing system proposed previously [1,10].

2. Experimental

The materials used in this study were the same as previously used [1], including *Veriflex* polystyrene shape memory polymer (PSMP) from Corner Stone Research Group, Inc., and a thermoplastic polymer identified as copolyester (CP) from Abifor, Inc., Switzerland. Two groups of the CP-PSMP composites, 3%CP-PSMP and 9%CP-PSMP, were fabricated by respectively dispersing 3% and 9% by volume of thermoplastic copolyester particles in the *Veriflex* shape memory polymer matrix. We used the same fabrication procedure that was detailed in our previous study [1]. The following experiments were conducted (1) DMA test to determine the glass transition temperature and viscoelastic behavior of the composites; (2) thermomechanical cycle test, particularly the confined stress recovery test and free strain recovery test; (3) preparation, programming, and three-point bending fracture test of single edge notched bend (SENB) specimens; (4) healing of fractured SENB specimens per the bio-inspired CTH scheme; (5) determination of healing efficiency through repeated fracture/healing tests; (6) SEM observation of fractured and

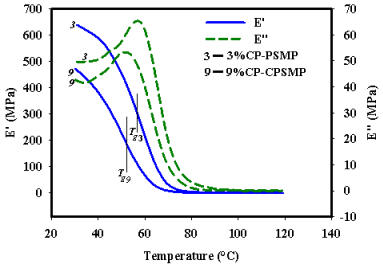

Fig. 1 DMA test results

healed surfaces; and (7) FTIR examination to determine the interaction between the CP and PSMP. Details of the test procedures and associated ASTM standards can be found in previous studies [1, 8, 9, 10].

3. Results and Discussion

Figure 1 shows typical DMA test results. It is clear that the T_g of the composites lowers as the CP content increases. Also, 80°C can be used for programming the composites because it is above the glass transition zone. Figure 2 shows typical 3D thermo-mechanical cycles of 9%CP-PSMP composite. The fully confined stress recovery ratio of the composites are 66%, 60%, and 44%, when the CP contents are 3%, 6%, and 9%, respectively. Therefore, the stress recovery functionality of the CP-PSMP composite reduces with increasing CP content. It is also seen that free strain recovery ratio is above 98% for all the specimens, suggesting good shape memory functionality of the composites. Figure 3 shows typical load deflection curves of 9% CP-PSMP. When comparing the peak bending loads of the healed specimen with the peak bending load of the original un-notched specimen, it is seen that the healing efficiency for the 3%CP composite is 51.3%, while it is about 75.0% for 9%CP composite. These healing efficiencies are significant as compared with previous results [5,16], which used about 10-40% of CPs. Figure 4 shows the peak bending load with fracture-healing cycles. Obviously, the self-healing is repeatable. The reason for the repeatability comes from (1) the programming and recovery of the PSMP matrix only experience physical changes, no chemical change is involved; and (2) the CP can be repeatedly melted and hardened. Figure 5 shows typical SEM images of the fractured surfaces of (a) a 3% CP specimen (left) and (b) a 9% CP specimen (right), after first healing and fracture cycle. It is clear that as the CP content increases, more traces of CP can be found in the fractured/healed surface. Figure 6 shows typical FTIR spectra of the PSMP, CP and the particulate composites with 3%, 6% and 9% CP contents. Careful examination shows that the spectra of the composites are a superposition of the two components (CP and PSMP). No new and significant peaks were identified, suggesting that no new functional groups or components were formed. This indicates that no chemical interactions or reactions occurred between the PSMP and CP polymers.

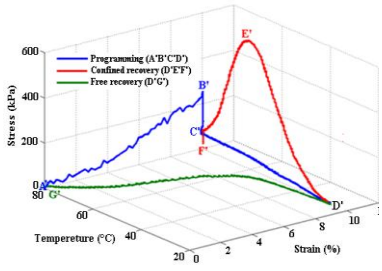

Fig. 2 Thermomechanical cycle with 9%CP

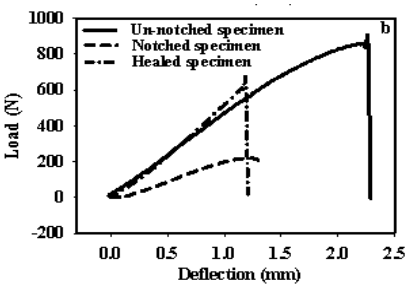

Fig. 3 Load-deflection curves with 9% CP

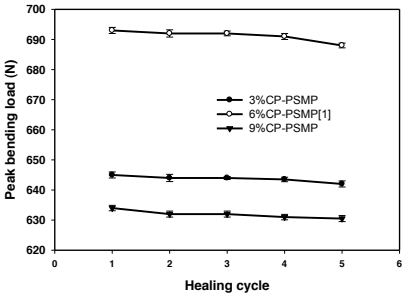

Fig. 4 Peak bending load with healing cycles

Fig. 5 Typical SEM images after healing and re-fracture

4. Conclusions

Based on the test results, it is found that as the CP content increases, the T_g reduces and the healing efficiency increases. It is also found that the composites still have very good shape memory functionality after incorporation of the CP. The self-healing is repeatable and pretty stable as the fracture-healing cycle increases. SEM observation shows that the CP has been melted during the self-healing process. FTIR test confirms that the interaction between the CP and the PSMP matrix is physical. Because of the capability for the composites to heal macroscopic cracks repeatedly and molecularly, it is expected that these composites have a potential to be used in pressurized gaseous energy storage and transportation. This will be a focus of next-step studies.

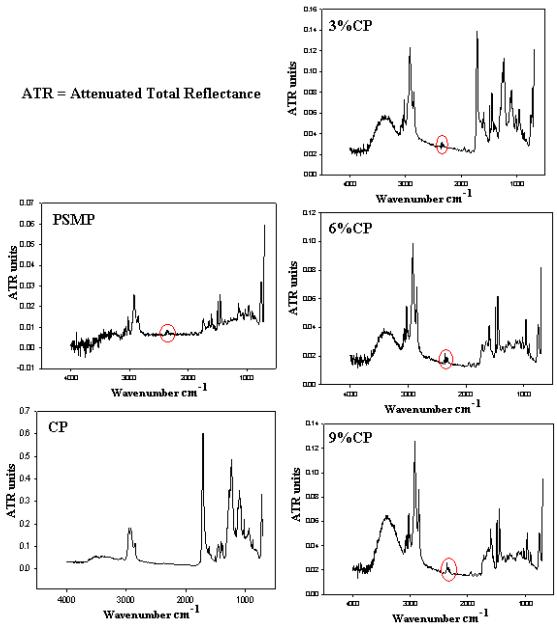

Fig. 6 FTIR spectra of CP, PSMP, and their composites

Acknowledgement:

The current work is funded by NSF EPSCoR CyberTools project under award #EPS-0701491 and by NSF CMMI 0900064.

References:

[1] J. Nji and G. Li. *Polymer*, 51: 6021-6029, (2010).
[2] S.R. White, N.R. Sottos, P.H. Geubelle, J.S. Moore, M.R. Kessler, S.R. Sriram, E.N. Brown and S. Viswanathan. *Nature*, 409: 794–797, (2001).
[3] J.W.C. Pang and I.P. Bond. *Composites Science and Technology*, 65: 1791–1799, (2005).
[4] K.S. Toohey, N.R. Sottos, J.A. Lewis, J.S. Moore and S.R. White. *Nature Materials*, 6: 581–585, (2007).
[5] M. Zako and N. Takano. *Journal of Intelligent Material Systems and Structures*, 10: 836–841, (1999).
[6] Y.L. Liu and Y.W. Chen. *Macromolecular Chemistry and Physics*, 208: 224–232, (2007).
[7] R.J. Varley and S. van der Zwaag. *Acta Materialia*, 56: 5737–5750, (2008).
[8] G. Li and D. Nettles. *Polymer*, 51: 755–762, (2010).
[9] W. Xu and G. Li. *International Journal of Solids and Structures*, 47: 1306-1316, (2010).
[10] G. Li and N. Uppu. *Composites Science and Technology*, 70: 1419–1427, (2010).
[11] G. Li and M. John. *Composites Science and Technology*, 68: 3337–3343, (2008).
[12] M. John and G. Li. *Smart Materials and Structures*, 19: (paper number 075013) 1–12, (2010).
[13] G. Li and V.D. Muthyala. *Composites Science and Technology*, 68: 2078-2084, (2008).
[14] J. Nji and G. Li. *Smart Materials and Structures*, 19: (paper number 035007) 1-9, (2010).
[15] G. Li and W. Xu. *Journal of the Mechanics and Physics of Solids*, 59:1231–1250, (2011).
[16] Hayes SA, Jones FR, Marshiya K, Zhang W. *Composites Part A - Applied Science and Manufacturing*, 38:1116–20, (2007).

CAVE-Based Visualization at SUBR

Sanjay Kodiyalam[1], Werner Benger[2], Somnath Roy[3], Sarat Paluri[4], Stephen Akwaboa[1], Michael G. Benissan[1], Sumanta Acharya[3], Partick Mensah[1], Amitava Jana[1]

Department of Mechanical[1] / Electrical[4] Engineering, Southern University
Center for Computation and Technology[2] / Dept. of Mechanical Engineering[2], Louisiana State University

Abstract: Ongoing work on visualization of *simulation data* in the CAVE at Southern's College of Engineering is described. Data from two different simulations have been visualized: (1) Streamlines and Pathlines in time-dependent 3-D velocity data from a multi-block computational fluid dynamics (CFD) simulation of a stirred tank, and (2) Temperature and heat flux in time independent 2-D data from a Fluent-based multi-scale computational heat transfer (CHT) simulation of a turbine blade cross-section and its thermal barrier coating (TBC). In both cases CAVE-based visualization helps to rapidly explore the simulation data via user operations driven by a joystick.

Keywords: Visualization, CAVE, Streamlines, Pathlines, Temperature, TBC

1. Introduction

With the increasing power of parallel and desktop machines CFD/CHT simulations are producing data on a large scale. Exploration of these datasets is challenging on account of the complex meshes used to resolve the length scales. Figure 1 shows the multi-block mesh used in the parallel CFD simulation of a stirred tank [Fig1. (a)], and the non-uniform mesh used in the CHT simulation of a turbine blade cross-section [Fig1. (b)].

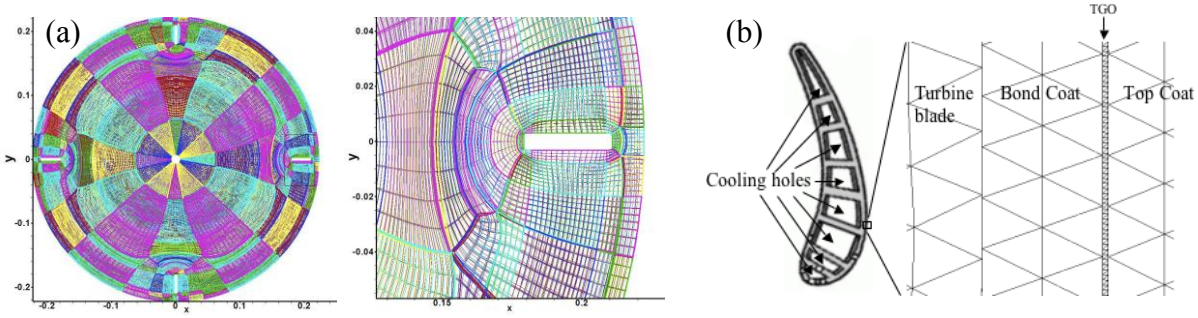

Fig. 1. (a) Top view of the 3D finite volume mesh used in CFD [1]. The mesh is composed of 2,088 blocks each of which has nodes along a curvilinear coordinate system. The mesh is complex around the baffles (enlarged view show) as these regions used to break global fluid flow to enhance mixing. (b) Schematic of a turbine blade cross-section with cooling holes in the bulk and the TBC on the surface. In CHT the entire cross-section (~5 cm) is meshed with smaller elements towards the surface to focus on the thin (~5 μm) TBC comprising of three layers: the bond coat, the thermally growing oxide (TGO), and the top coat.

One of the ways of exploring data is in a virtual reality (VR) environment. The CAVE at Southern University is a projection-based VR system that surrounds the viewer with four displays that are arranged to make

a cube with three screen-walls that are rear-projected together with down-projection onto the floor. A user wears stereo shutter glasses with a six-degrees-of-freedom head-tracking device based on which the correct stereoscopic perspective projections are calculated for each display as the user moves inside the CAVE. A second sensor and buttons in a wand held by the viewer provide interaction with the virtual environment [2].

2. Exploring multi-scale data in the CAVE: Focal point based operations [3-5]

Joystick driven operations of translation, rotation, and scaling are enabled for exploring the data. Translation and rotation are in the fixed coordinate system of CAVE where as the scaling operations are in the world (the data's) coordinate system. Rotation and scaling are around a user defined focal point (Red (white) line in Fig. 2 (3)) that is normal to the data's XY plane and through the point of the intersection of this plane with the line emanating from the joystick towards the front (Red line in Fig. 3). To keep the focal point invariant rotations are implemented after shifting the focal point to the origin of the CAVE's coordinate system. As scaling in the world coordinate system commutes with translations in the CAVE's coordinate system an explicit back translation of the focal point is carried out to keep it invariant under scaling. For the 2D datset two other types of scaling are enabled: Isotropic scaling in the world XY-plane, and scaling only along the world Z-axis. In this case view of the mesh edges is also enabled via keyboard input (Fig, 3).

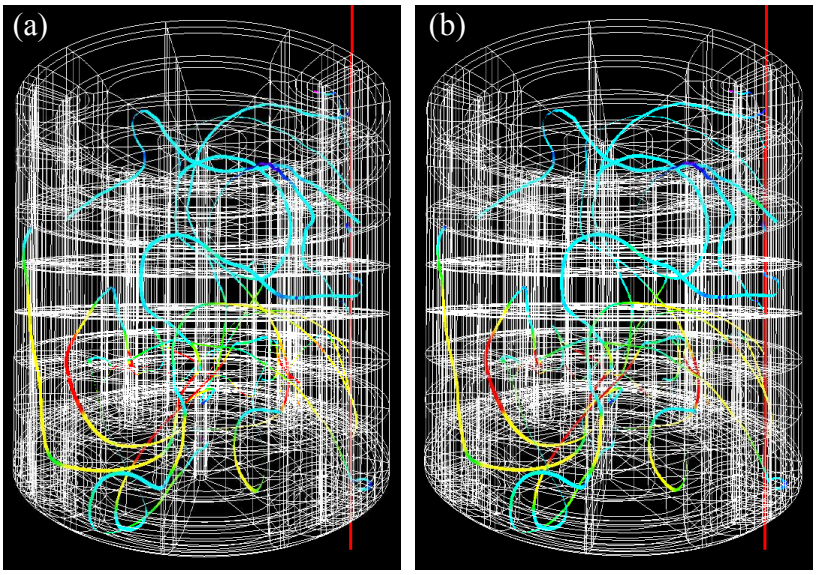

Fig. 2. Perspective right eye (a) and left eye (b) views of the stirred tank's CFD mesh together with pathlines, visualized as ribbons, originating from a vertical line emitter (red line) close to a baffle. The ribbons are color coded based on the magnitude of velocity. The normal to the pathline in the plane of the ribbon is arbitrarily chosen at the emitter. It is parallel transported along the pathline and ortho-normalized relative to the direction of the pathline at beginning of each time step. Stereoscopic viewing can be enabled via overlapping the twoo images by appropriate squinting of the eyes.

3. Visualization applications: Results

A Visual Studio based C/C++ project, using the CAVE Library 3.2, is developed for visualizing streamlines/pathlines in the CFD data of the stirred tank [3,4]. To enable quick exploration of the large stirred tank CFD dataset (2088 curvilinear blocks with a total of ~2.3 million nodes at which fluid velocity (3D) and pressure are specified for 5,699 time steps) the following steps, inspired by algorithms used in classical atomistic simulations and exploiting the time independence of the CFD mesh, are implemented [3,4]: (1) Interpolation of nodal velocity based on node-specific spherical cutoffs, (2) Reorganizing nodes as belonging to a uniform mesh of cubic regions analogous to earlier work mapping curvilinear block cells to a uniform grid [6], and (3)

Reorganized nodal data written to files in binary format analogous to the F5 format for a uniform grid [7]. These steps are completed before exploring the stirred tank dataset in the CAVE. Together with reading in only the data required for visualization [8] they have enabled rapid (~1-3 seconds) computation and display of 10 streamlines, computed with 1000 RK4 integration steps, from a user-selected seeding line (red line in Fig. 2). Pathlines on the other hand take longer (~260 seconds) due to disk access limitations that become severe when requiring to access data across 1000 time steps.

A similar Visual Studio based project is developed for visualizing the temperature in the CHT data of the turbine blade cross-section [5]. Temperature is visualized directly from its nodal values on the 2-D triangular mesh. To accentuate gradients the temperature is also encoded as height thereby making the narrow TBC region comparable in extent to the turbine blade. In addition directional lighting and reflection also helps in identifying changes in the temperature gradient (Fig. 3a).

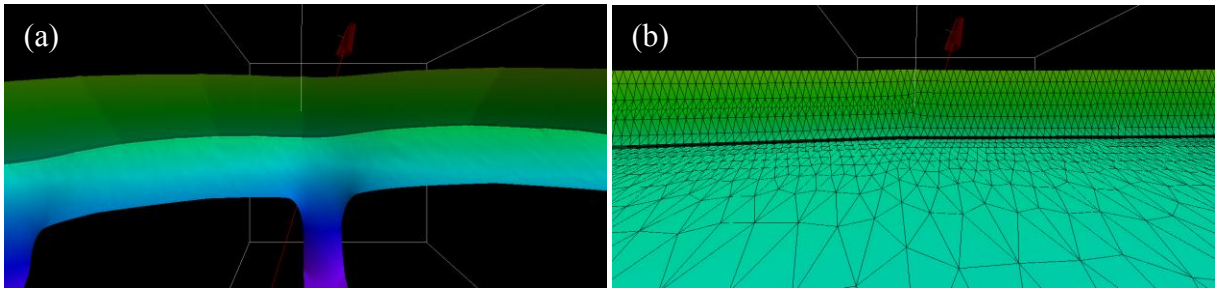

Fig. 3. (a) Close up view of a region of the TBC's top coat showing straight lines under directional lighting and reflection indicating changes in the temperature gradient. A point near one such change is made the focus followed by scaling up of the world XY plane. (b) shows an enlarged image of the corresponding view. The focal point has identified a change in the mesh structure suggesting possible dependence of the CHT temperature on this mesh feature.

4. Conclusions and Ongoing Work

Memory management via reading in only the data needed for visualization enables exploration of large (~400 GB) CFD datasets whose total size is much larger than the available RAM (64 GB) [8,3,4] on the machine used for visualization. Ongoing work is on overcoming the disk access limitation when displaying pathlines by pre-computing them on a parallel machine and reading in all of the pathlines before displaying them based on user selected seed points and temporal extent. In order for pathlines across all of the time steps (~5700 CFD time steps converted to 2850 steps due to RK4 time step = ½ the CDF time step) to be accommodated into ~75% of the available RAM they are computed from seed points as densely spaced as possible – yielding 89^3 seed points along the x,y, and z extents of the stirred tank – yielding a total of ~520,000 pathlines. The entire process of pre-computation is completed in 2.64 hrs on 64 CPU's of the LONI machine Queenbee. However, reordering of the computed output to have all steps of a pathline together required an additional 0.32 hours. This reordering can also be carried out on the machine used for visualization as a preprocessing step. Nevertheless the rapid speed of the pathline computations on the parallel machine has suggested that we may dynamically coupling parallel computations on the LONI machines to visualization in the CAVE at Southern [9]. Focal-point based operations of rotation and scaling in the 3-D visualization of the CHT data for a turbine blade cross-section can help in identifying possible mesh dependence in the computed solutions and can thereby help in evaluating mesh quality.

Visualizing the heat flux (temperature gradient x scalar conductivity) is currently in progress. We will visualize the heat flux as ribbons along lines whose tangent is the temperature gradient. We propose to follow the multi-scale nature of the mesh when integrating the equation for these lines: The temperature gradient is evaluated as a constant for each triangle in the mesh and within each the direction of the gradient is followed from the entry to the exit of the line. The integration step size therefore changes in accordance with the size of the triangle. The performance and accuracy of this algorithm will serve as a benchmark for evaluating other methods that differ in how the step size is determined.

5. Acknowledgement

The current work was funded by the NSF EPSCoR CyberTools project under award #EPS-0701491 (CyberTools), NSF DGE-0504507 (IGERT), and was made possible in part by a grant from BP/The Gulf of Mexico Research Initiative. Ongoing work is supported by LA-SiGMA (NSF EPS-1003897). We thank Sandeep Khurana, Farid Harhad, Bidur Bohara, Nathan Brener, and Marcel Ritter for their insights from related work on visualizing the stirred tank data [8] and their supportive interest in CAVE-based visualization. The Center for Energy and Environmental Studies at Southern University is acknowledged for supporting hardware upgrades to the CAVE. LONI is acknowledged for compute time under allocation loni_compviz02/03.

6. References

1. S. Roy, S. Acharya: Stirred Tank Dataset, Unpublished.
2. Dave Pape, Carolina Cruz-Neira, Marek Czernuszenko: CAVE Library version 2.6. Electronic Visualization Laboratory University of Illinois at Chicago, (1997)
3. K. Sekeroglu, S. Kodiyalam, B. Ullmer, R. Sankaran, W. Benger, S. Roy, A. Wallace, S. Acharya, A. Jana: Exploring Stirred Tank CFD Simulation Data via Tangible Interaction with Mechatronic Interface Coupled to CAVE-based Visualization. In the Proceedings of the ASEE-GSW, Session G-17, pgs. 1-7, (2010)
4. K. Sekeroglu, S. Kodiyalam, B. Ullmer, R. Sankaran, W. Benger, S. Roy, A. Wallace, S. Acharya, A. Jana: Exploring Stirred Tank CFD Simulation Data via Tangible Controlled Mechatronic Interface and CAVE-based Visualization. In the Proceedings of the Louisiana EPSCoR RII Cybertools/Science Drivers 2010 Symposium, Pgs. 49-52.
5. S. Kodiyalam, B. Mukerji, S. Akwaboa, P. Mensah, and A. Jana: Visualizing simulated Multi-Scale Data: Temperature and Heat Flux in a Turbine Blade Cross-Section and its Thermal Barrier Coating. In the Proceedings of the Louisiana EPSCoR RII Cybertools/Science Drivers 2010 Symposium, Pgs. 129-132
6. W. Benger, M. Ritter, S. Acharya, S. Roy, and F. Jijao: Fiberbundle-based visualization of a stir tank. In 17th International Conference in Central Europe on Computer Graphics, Visualization and Computer Vision, pp 117-124 (2009)
7. W. Benger: On Safari in the file Format Jungle – Why Can't You Visualize My Data? Computing in Science and Engineering-11-6, pp 2-6 (2009)
8. B. Bohara, F. Harhad, W. Benger, N. Brener, S. Iyengar, M. Ritter, K. Liu, B. Ullmer, N. Shetty, V. Natesan, C. Cruz-Neira, S. Acharya, S. Roy, and B. Karki: Evolving time surfaces in a virtual stirred tank. In Vaclav Skala, editor, 18th International Conference on Computer Graphics, Visualization and Computer Vision'2010 (2010)
9. Sarat Paluri, Proposed research for LONI Graduate Fellowship Application, May 2011.

Construction of Metal Oxide Force Fields: Preliminary Studies

Shuo Yao,[1] Joshua Slocum,[1] Collin D. Wick,[1] and B. Ramu Ramachandran,[1]
Randall Hall[2] and Cheri A. McFerrin[2]

[1]Chemistry, Louisiana Tech University, Ruston, LA 71272
[2]Department of Chemistry, Louisiana State University, Baton Rouge, LA 70803

Abstract: One of the major goals of Science Driver 2, Focus 3 of LA-SiGMA is to construct reactive force fields for studying Fischer-Tropsch reactions on metal oxide catalysts. We report on preliminary calculations undertaken in Year 1 to begin the construction of metal oxide force fields. Three metal oxides, Al_2O_3, FeO, and Fe_2O_3 are being studied at present. The current objective is to identify and develop confidence in computational protocols that can be used both for force field construction of the oxides mentioned above, and also be adapted to the development of force fields for other metal oxides of interest in the future.

Keywords: Metal oxides, catalysts, force fields, Fischer-Tropsch

1. Introduction

A major part of the La-Sigma project is to develop the computational framework to investigate the structure and reactivity of complex materials for catalytic reactions. One of these reactions is the conversion of coal, natural gas, or biomass into useable petroleum like hydrocarbons. This is of special importance for the U.S. as the former species are quite common domestically, while the latter have to be mostly imported. These reactions usually occur via a Fischer-Tropsch process, which occurs with a catalyst in which oxides of transition metals such as Fe, Co, and Ni play a major role. Beyond this important class of catalyst, one of the most common catalytic supports is alumina. To understand the catalytic process for these materials, and specifically for the case of alumina, how it behaves as a support, requires their simulation at multiple time and length scales. *Ab initio* methods are quite successful for the investigation of a few to dozens of atoms, and can bring a significant amount of insight into a variety of processes. The most catalytically active sites are often material defects, in which their structures are not well understood or predictable. Due to the fact that *ab initio* calculations investigate only a few atoms over a relatively short period of time, the likelihood of observing these defects is vanishingly small. Because of this, larger scale simulations (10,000s of atoms) that can run over much longer timescales (100s of nanoseconds) would be of significant benefit for the investigation of catalysis. These simulations can be used to efficiently identify potential defect sites, which can be further investigated via more expensive *ab initio* calculations, building a truly multiscale approach to the computational investigation of catalysis.

To carry out large scale simulations requires the development of accurate molecular models that can describe bulk solid, interfacial, and defect structures simultaneously. For alumina, many force fields have already been developed, [1-6] some of which are quite complicated. However, these have been developed to reproduce the bulk

solid structure of alumina, and are mostly based on pair-wise interactions of Al with O. A literature search suggests that very few force fields exist for iron oxides, and these have been parameterized to reproduce small iron oxide structures [7,8] for Fe(III) compounds. We are developing a new strategy to develop oxide force fields that rely on reproducing small cluster structures utilizing new state of the art density functional theory (DFT) functional, and we will also accurately describe different solid phases, and physical interactions with molecules at the surface of these. Furthermore, bonded interactions, such as bond stretching interactions between adjacent atoms and bond bending between three atoms in the solid structure, will be used. Also, many-body non-bonded interactions will be used, including van der Waals interactions, electrostatic charges and polarizable interactions. These many-body interactions are important to be able to represent the correct interactions in different environments. The described strategies should allow a transferable force field to be developed that can be especially useful in finding potential solid defects.

2. Computational Strategies and Methods

In both Al_2O3 and Fe_2O_3 the metal atom is surrounded by 6 Oxygen atoms in a distorted octahedral symmetry. The M-O bond lengths and O-M-O bond angles fall into two groups which, in Table 1, are denoted as R_1, R_2, and θ_1, θ_2, respectively. In order to reproduce this geometry by *ab initio* computations on small clusters of M and O atoms, we explored various possibilities but finally settled on geometry optimizations of $M(OH)_3(H_2O)_3$. The unit cell of FeO is a face-centered cube in which the Fe atom is in a perfect octahedral environment of six O atoms. To reproduce this structure by DFT computations, we optimized the geometries of $[Fe(H_2O)_6]^{2+}$.

Calculations on Al_2O_3 employed the hybrid exchange-correlation functional PBE1PBE of Perdew, Ernzerhof, and Burke[9] with the polarized triple-zeta quality 6-311+G(*d*,*p*) basis set. A more recent meta-hybrid functional developed by Zhao and Truhlar, M06-2X,[10] was also used for additional calculations. It was assumed (and computationally verified) that the ground electronic state of the $Al(OH)_3(H_2O)_3$ is in a singlet spin state. Calculations on Fe_2O_3 and FeO both utilized the M06-L functional of Zhao and Truhlar[10] with the polarized triple zeta 6-311+G(*d*,*p*) basis. In these cases, we examined various plausible spin states for both complexes and established that the FeO complex is a quintet in the ground state while Fe_2O_3 is a hextet. All calculations to date have been done using the Gaussian 09 software package.[11]

3. Results

The *average* bond lengths and bond angles (in the case of M_2O_3, the average for each group) for the models used for the three metal oxides are compared with crystallographic parameters in Table I. The percent errors in calculated properties are given by $|1-R| \times 100$, where R represents the ratios f_i and ϕ_i reported in Table I. For Alumina, the largest errors in bond length are about 5% and the largest error in the bond angles are about 6%. The geometry of $Fe(OH)_3(H_2O)_3$ used as a model for Fe_2O_3 results in fairly large errors (as large as 11% in bond lengths and 8% in angles) while $Fe(H_2O)_6$ turns out to be an excellent model for FeO.

Table I. Comparison of crystallographic structural parameters with *average* calculated values for the three metal oxides studied. The ratios f_1, ϕ_2, etc. give the ratio calculated/crystal for the parameter immediately to the left.

	R_1(crystal) Å	f_1	R_2(crystal) Å	f_2	θ_1(crystal) (deg)	ϕ_1	θ_2(crystal) (deg)	ϕ_2
Al_2O_3	1.852	0.973	1.972	1.05	101.2	1.06	79.6	1.04
Fe_2O_3	1.960	0.965	2.087	1.11	102.7	1.08	77.6	0.99
FeO	2.166	0.994	-	-	90.0	1.00	-	-

Relaxed potential energy surface (PES) scans have been performed to obtain the variation of energy as a function of bond lengths and bond angles for each of the metal oxides studied.

To calculate non-bonded metal-metal interactions, we are considering the types of structures shown in Figure 1. The Al_2O_3 model, i.e., $[Al_2(OH)_3(H_2O)_6]^{3+}$ is converged, and calculations in progress for the Fe_2O_3 model, i.e., $[Fe_2(OH)_3(H_2O)_6]^{3+}$ and that for FeO, i.e., $[Fe_2(OH)_2(H_2O)_6]^{2+}$. While the Al cluster is a spin singlet, the ground multiplicities of the Fe^{3+} and Fe^{2+} compounds appear to be 11 and 9, respectively, leading to some very challenging calculations.

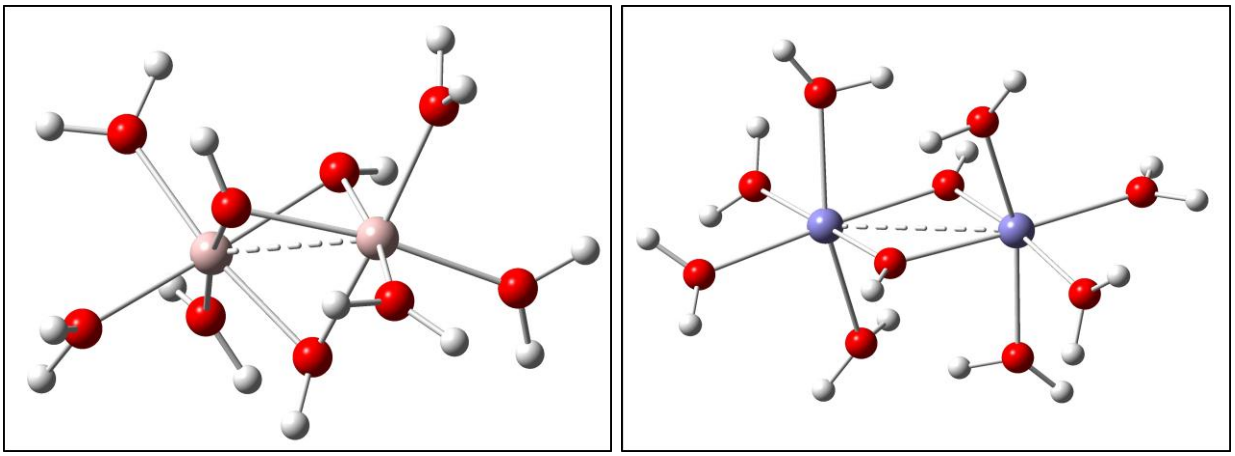

Figure 1. Structures of $[Al_2(OH)_3(H_2O)_6]^{3+}$ (left) and $[Fe_2(OH)_2(H_2O)_6]^{2+}$ (right) being used to calculate non-bonded metal-metal interactions (indicated by dashed line). The former is a singlet while the ground state of the latter appears to be $2S+1=9$.

4. Conclusion and Future Work

Computations completed thus far provide a good foundation for (a) developing force fields for the metal oxides studied, and (b) for extending these methods to other metal oxides. The geometry dependent charges will be

obtained by fitting to the electrostatic potential. In order to improve the agreement between the geometries predicted by the force field and those obtained from the crystal lattice, we will use Bowman's scaled coordinates.[12] Non-bonded metal-metal interactions will be computed from potential scans starting with the equilibrium geometries shown in Figure 1. Non-bonded O-O interactions may be taken from existing models or computed. We hope to combine the metal oxide force fields with existing force fields for interactions of CO, CO_2, H_2, CH_4, etc., to study reactions in Year 2.

5. Acknowledgments

The current work is funded by the NSF EPSCoR LA-SiGMA project under award #EPS-1003897. Grants of computer time on LONI supercomputers are gratefully acknowledged.

6. References

(1) Gutiérrez, G.; Belonoshko, A. B.; Ahuja, R.; Johansson, B. *Physical Review E - Statistical Physics, Plasmas, Fluids, and Related Interdisciplinary Topics* 2000, *61*, 2723.

(2) Adiga, S. P.; Zapol, P.; Curtiss, L. A. *Journal of Physical Chemistry C* 2007, *111*, 7422.

(3) Rosen, J.; Warschkow, O.; McKenzie, D. R.; Bilek, M. M. M. *Journal of Chemical Physics* 2007, *126*.

(4) Jahn, S.; Madden, P. A. *Condensed Matter Physics* 2008, *11*, 169.

(5) Du, J.; Benmore, C. J.; Corrales, R.; Hart, R. T.; Weber, J. K. R. *Journal of Physics Condensed Matter* 2009, *21*.

(6) Youngs, T. G. A.; Weber, D.; Gladden, L. F.; Hardacre, C. *Journal of Physical Chemistry C* 2009, *113*, 21342.

(7) Aryanpour, M.; Van Duin, A. C. T.; Kubicki, J. D. *Journal of Physical Chemistry A* 2010, *114*, 6298.

(8) Rustad, J. R.; Hay, B. P.; Halley, J. W. *The Journal of Chemical Physics* 1995, *102*, 427.

(9) Perdew, J. P.; Ernzerhof, M.; Burke, K. *Journal of Chemical Physics* 1996, *105*, 9982.

(10) Zhao, Y.; Truhlar, D. G. *Theoretical Chemistry Accounts* 2008, *120*, 215.

(11) Frisch, M. J. T., G. W.; Schlegel, H. B.; Scuseria, G. E.; Robb, M. A.; Cheeseman, J. R.; Scalmani, G.; Barone, V.; Mennucci, B.; Petersson, G. A.; Nakatsuji, H.; Caricato, M.; Li, X.; Hratchian, H. P.; Izmaylov, A. F.; Bloino, J.; Zheng, G.; Sonnenberg, J. L.; Hada, M.; Ehara, M.; Toyota, K.; Fukuda, R.; Hasegawa, J.; Ishida, M.; Nakajima, T.; Honda, Y.; Kitao, O.; Nakai, H.; Vreven, T.; Montgomery, Jr., J. A.; Peralta, J. E.; Ogliaro, F.; Bearpark, M.; Heyd, J. J.; Brothers, E.; Kudin, K. N.; Staroverov, V. N.; Kobayashi, R.; Normand, J.; Raghavachari, K.; Rendell, A.; Burant, J. C.; Iyengar, S. S.; Tomasi, J.; Cossi, M.; Rega, N.; Millam, N. J.; Klene, M.; Knox, J. E.; Cross, J. B.; Bakken, V.; Adamo, C.; Jaramillo, J.; Gomperts, R.; Stratmann, R. E.; Yazyev, O.; Austin, A. J.; Cammi, R.; Pomelli, C.; Ochterski, J. W.; Martin, R. L.; Morokuma, K.; Zakrzewski, V. G.;Voth, G. A.; Salvador, P.; Dannenberg, J. J.; Dapprich, S.; Daniels, A. D.; Farkas, Ö.; Foresman, J. B.; Ortiz, J. V.; Cioslowski, J.; Fox, D. J.; Rev. A.1. ed.; Gaussian Inc.: Wallingford, CT, 2009, p Gaussian 09.

(12) Gazdy, B.; Bowman, J. M. *The Journal of Chemical Physics* 1991, *95*, 6309.

Density Functional Theory Study of the Effect of 3*d* Transition Metals on $NaMgH_3$ Complex Metal Hydride for Hydrogen Storage Applications

Fernando Soto[1], Daniela S. Mainardi[2]

[1]Institute for Micro-manufacturing, Louisiana Tech University
[2]Institute for Micro-manufacturing, Chemical Engineering, Louisiana Tech University

Abstract: In the current research, study of catalytic additives allowed us to rationalize the effect of 3*d* elements in $NaMgH_3$ performance as hydrogen storage material. For this purpose, plane wave density functional theory (PW-DFT) calculations helped us examine bulk and surface models of $NaMgH_3$ complex metal hydrides (CMHs) with impurities from the 3*d* element block. In this respect, first-principles calculations determined the cohesive energies of pure and doped bulk/surface CMHs as well as the adsorption/substitution energies. The results demonstrate that 5 out of 7 additives in the bulk model are thermodynamically stable relative to the pure model; therefore, possible. The most favorable elements in this regard came out to be; Ti, V, and Co in that order.

Keywords: density functional theory, hydrogen storage.

1. Introduction

Recently, Mg-based hydrides have attracted attention as a hydrogen storage medium due to their light weight and low cost [1]. Several Mg-based hydrides take the perovskite structure expressed as ABH_3, where A is an alkali element and B is magnesium. $NaMgH_3$ is the only magnesium based ternary hydride with Na and it has attracted the attention as a possible candidate for hydrogen storage material because it has high gravimetric hydrogen density (6 %) and high volumetric hydrogen density (88 kg/m^3) [2]. This magnesanate has not been widely investigated as a candidate for hydrogen storage. The crystal structure of this material derives from the cubic $KMgH_3$ by an orthorhombic distortion and has a perovskite structure similar to $GdFeO_3$ [1]. It belongs to the *Pnma* space group with orthorhombic symmetry in the temperature range of 4 to 370 K [2, 3]. The primitive unit cell contains four formula units with a total of 20 atoms.

Hydrogen disassociation in this material occurs at atmospheric pressure and approximately 670 K, which is well above the operable range for on board hydrogen storage applications. Thus, $NaMgH_3$ is more thermally stable than binary MgH_2, which has a hydrogen dissociation temperature ~550 K. The dehydrogenation reaction scheme takes place in two steps [3]:

$$NaMgH_3 \rightarrow NaH + Mg + H_2 \quad (1)$$

$$NaH \rightarrow Na + \frac{1}{2} H_2 \quad (2)$$

Furthermore, dopants/catalysts are usually mixed with the hydride by mechanical ball milling, which introduces defects and impurities. However, much research still needs to be done in order to determine appropriate catalysts, study the existence of stable intermediate phases and their crystal structure, and understand the kinetics. Much insight can be gained from first principles simulations for the purpose of designing alloy catalysts.

2. Computational Methods

2.1 Bulk Calculations

In this study, we use the first principles pseudopotential total energy method through the generalized gradient approximation (GGA) calculations with the Perdew and Wang (PW91) functional as implemented in the CASTEP® module [5] of the Materials Studio® software by Accelrys, Inc. [6] to study bulk and surface models of $NaMgH_3$. Spin-polarized calculations on Fe-, Ni-, and Co-doped systems show no significant effect to be created energetically, with respect to the non-spin polarized calculations. Hence, further conducted geometry optimization calculations were spin-unpolarized, and the cut-off energy was 400 eV with a fine k-point mesh in all cases.

We created hydride models alloyed with $3d$ block transition metals to investigate their effects on the energetics of bulk/surface of $NaMgH_3$ systems. The alloying elements substitute one Na atom at a center lattice location of each structure, resulting in a concentration between 5.65 and 7.57 at.%. Afterwards, bulk hydrides and surface slabs relaxed entirely in terms of all atomic degrees of freedom to obtain the ground-state energy system. After complete relaxation of the systems was obtained, single-point energies were calculated for the optimized structures. Since the main aim of this work is to illustrate which transition metals are most effective in improving the kinetics and thermodynamics of the prototype $NaMgH_3$ system, calculation of cohesive energies (ΔE_{coh}) of the doped systems were calculated according to equation (3).

$$\Delta E_{coh} = E_{TOT}(Na(X)MgH_3) - [NE\,(Na) + NE(Mg) + NE(H) + E(X)] \quad (3)$$

Where E_{TOT} is the total energy of the system, N is the number of atoms, E(Na) is the energy of a free neutral atom of Na, E(Mg) is the energy of a free neutral atom of Mg, E(H) is the energy of a single hydrogen atom and E (X) is the energy of a free neutral transition metal X.

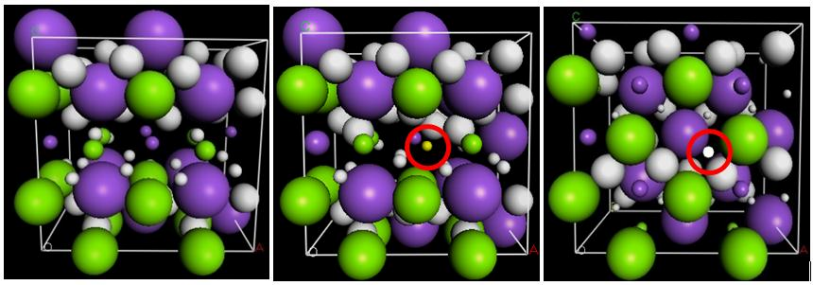

(a) (b) (c)

Figure 1. $NaMgH_3$ 2x1x2 Supercell consisting of five f.u. (a) pure model, (b) Ti_{sub}@Na in model, and (c) Vac_{sub}@Na in model.

2.2 Surface Calculations

Besides the studies regarding bulk doped $NaMgH_3$ systems, we considered the adsorption/substitution behavior of Ti on the $NaMgH_3$ (001) surface. Accordingly, the calculations were performed for surface structures with a slab width of 2x1x2, and a gap of approximately 5 Å at the top of the $NaMgH_3$ surface. Moreover, k-point sampling is performed at the gamma point only. Doping on the surface structure proceeded in two distinct steps: first, one is

the substitution adsorption, in which the dopant replaces a Na atom at the center lattice location of the uppermost layer of $NaMgH_3$ (001) surface. The second form of adsorption in the on-top of surface adsorption.

The substitutional/adsorption energy calculation for the (001) surface proceeds via the following equation:

$$E_{add} = E_{coh}\frac{(X\mathrm{NaMgH_3})}{N} - E_{coh}\frac{(\mathrm{NaMgH_3})}{N} \quad (4)$$

Where N is the total number of atoms in the model and X is the transition metal added to the system.

3. Results and Discussion

The equilibrium cell parameters a, b and c of pure $NaMgH_3$ are 5.48, 7.68 and 5.40 Å, respectively. A brief comparison with experimental values showed that; these calculated values are of 0.20 % different than the initially set unit cell dimensions, which is a strong indication of the good agreement between the computational and experimental results.

3.1 Bulk

Next, the primary goal in calculating the cohesive energy energies for each alloyed system was to investigate the effect of $3d$ block elements in the stability of the system. Modification in $NaMgH_3$ models took place via addition of selected impurity elements X (where X can be any element from $3d$ block: Sc, Ti, V, etc) to the desired $NaMgH_3$ model. The cohesive energy of the pure model served as the reference value; thus, any energy above 0 eV is stable. It is interesting to note that several elements added as dopants in the $NaMgH_3$ structure are thermodynamically stable and; therefore, appealing for further consideration.

In this respect, Ti, V, Sc, Co, Ni and Cu in the decreasing order, are the most favorable elements with respect to the cohesive energy of the pure system (Figure 2). For instance, the cohesive energy due to the presence of the Ti dopant is 2.89 eV more favorable than the pure case where no dopants are available. Meanwhile, the removal of a Na ion from the pure model is 3.95 eV less preferred than the pure model. Also, V is 2.64 eV more energetically favorable, Sc has a value of +2.16 eV, and for Co and Cu those values are +1.62 eV and +0.62 eV respectively. On the other hand, Zn and Mn where found to be unfavorable in this system with cohesive energies of -2.58 eV and -0.68 eV, respectively.

Finally, it should be pointed out that; the cohesive energies of these $3d$ block elements in the bulk follow a strong correlation with the cohesive energies of their metallic elements counterpart. Thus, a high cohesive energy value of the metallic element helps to predict a high cohesive energy value in the bulk model. Such prediction helps to identify additional elements that could improve on the effect of $3d$ block transition elements on $NaMgH_3$.

3.2 Surfaces

Next, DFT calculations were conducted on five (001) surface models : Ti @ Na lattice site, Ti @ hollow site, Ti @ top of Na lattice site, Ti @ top of hollow site, and Ti @ Mg site. It is possible to observe the preferred Ti dopant site in terms of the substitutional/addition energy relative to the pure surface model. In this regard, possible formation of $TiMg_xH_x$ complexes was systematically investigated.

From our calculations, Ti @ Hollow site and Ti @ Na site are the preferred sites for the dopant in this system. Ti @ Hollow site has a cohesive energy of +5.47 eV and Ti @ Na site has a cohesive energy value of +4.60 eV. Furthermore, Ti @ Mg shows a more favorable cohesive energy value than Ti @ Top sites with values of +4.23

eV and +3.22 eV, respectively. Simulation results also showed that it is more favorable to remove a hydrogen atom from a doped model than from the pure model, with values of +3.05 eV and –3.46 eV, respectively. Thus, for subsequent calculations only the most favorable models will be tested.

4. Conclusion and Future Work

The cohesive energies of the 3*d* block elements in the bulk follow a strong correlation with the cohesive energies of their metallic elements counterpart. From the cohesive energy calculation on surface models, we conclude that dopants at the hollow and Na lattice sites are the most favorable sites for dopant locations in the $NaMgH_3$ system. Thus, future studies will have more emphasis on those models. Finally, Ti @ Na lattice site shows a possible Ti-Mg_4H_6 complex formation upon completion of geometry optimization. In the same manner, Ti @ Hollow site shows a possible $TiMg_5H_7$ complex formation; thus, showing an increased association of the bond lengths when compared to the Ti@ Na lattice site model.

It is worth mentioning that the Ti placed @ the hollow site of $NaMgH_3$ ejects a Na ion from its lattice site. This phenomenon will be further investigated to determine the role that it plays in desorption of H from the system. Furthermore, as a second step in the research program, the role of 3*d* transition metals such as Ti in the improved dehydrogenation kinetics of $NaMgH_3$ needs to be understood. Reactants and products will be optimized using DFT codes within the GGA approximation to determine the reaction barrier height for the first reaction. Reaction pathways will be determined through transition state search using LST/QST methods.

5. Acknowledgments

The current work is funded by LA-SiGMA, grant #EPS-1003897.

6. References

[1] Lovvik, O.M; Swang, O.; “Crystal structures and electronic structures of alkali aluminohexahydrides from density functional calculations.”J. Alloys. Compd. 2005. 404. 757-761.

[2] Aguayo, A; Singh, D.J.; “Electronic Structure of the complex hydride NaAlH4.”Phys. Rev. B. 2004. 69.103-108.

[3] Alapati, S. V; Johnson, K. J.; Scholl, D. S. “Identification of Destabilized Metal Hydrides for Hydrogen Storage Using First Principles Calculations.” J . Phys. Chem. B. 2006. 110. 8769-8776.

[4] Perdew, J.P. and Wang Y.;“Accurate and simple analytic representation of the electron-gas correlation energy.” Phys. Rev. B. 1992.45. 13244-13249.

[5] M. D. Segall, P. J. D. Lindan, M. J. Probert, C. J. Pickard, P. J. Hasnip, S. J. Clark, M. C. Payne;"First-principles simulation: ideas, illustrations and the CASTEP code." Journal of Physics: Condensed Matter. 2002.14.2717-2743.

[6] Accelrys, "Materials Studio®," 4.0 ed. San Diego: Accelrys Software, Inc., 2006.

[7] Klaveness, A.; Swang, O.; Fjellvag, H.; “Formation enthalpies of $NaMgH_3$ and $KMgH_3$: A computational study.” Europhys. Lett. 2006. 76. 285-290.

Development of Force Field for Span80 Using A*b Initio* Calculations

B. Thakur[1], K. Ratnayake[2], H. Ashbaugh[3], D. Moldovan[4]

[1]CCT and LONI Institute, Louisiana State University
[2]Chemistry Department, Louisiana State University
[3]Chemical and Biomolecular Engineering Department, Tulane University
[4]Mechanical Engineering Department, Louisiana State University

Abstract: Enhanced drug delivery is an important research area for the pharmaceutical industry. Drug delivery methodologies, such as those based on drug encapsulation into micelles, have shown promising characteristics and warrant further investigations. The understanding of self-assembly of Span80 into micelles is an important step in the development of drug encapsulation based on this relatively non-expensive amphiphile. Such studies can be carried out effectively at the atomistic level by using specialized simulation packages such as AMBER, GROMACS and CHARMM. Unfortunately, the accuracy of such simulations is determined by the accuracy of the force fields used to describe the inter-atomic interactions between molecular species comprising such a simulation system. Widely used force fields such as AMBER-ff03 and GROMOS53a6 are well suited to describe the interactions in certain molecular systems such as lipids, proteins, nucleic acids, etc. When the parameterization for the molecule of interest is not available in database one needs to develop the force field from scratch. The focus of the present study is to develop a parameterization of the force field for Span80.

Keywords: GROMACS, GROMOS, AMBER, Span80

1. Introduction

For most novel molecules, like Span80, the parameters extracted from the existing force field databases such as AMBER-ff03 and GROMOS-53a6 [1] are in general not reliable. AMBER uses GAFF (General AMBER force field) [2] to build topologies for small organic molecules. However, the parameters are not always reliable for novel molecules. Unlike AMBER, GROMACS does not always provide topologies. An alternative to using the well-established force fields is to obtain an initial guess topology by employing web-based servers like PRODRG and Automated Topology Builder (ATB) [3]. In our study, we prefer to use GROMACS as it is freely available and readily allows modifications to the parameters.

2. Calculations

In the present work the parameterization of Span80 was done in a manner that is compatible with the GROMOS-53a6, the most recent version of GROMOS force field. An initial geometry was obtained using Gaussview (see

figure 1), then we followed with preliminary energy minimization step using AMBER package to obtain a relaxed starting geometry. To reduce the computational effort in the quantum calculations the Span80 molecule was truncated by removing the tail part. It should be mentioned that the parameters for the atomic groups in the tail part can be easily obtained from lipid and alkane topologies; and do not require any optimization. The resultant molecule, shown in figure 2, is adequate for optimizing the relevant dihedral and angular force field parameters. In this study all calculations for force field parameters were performed on this reduced Span80 fragment (see Figure 2). Next we give a brief description of the ab-initio calculations.

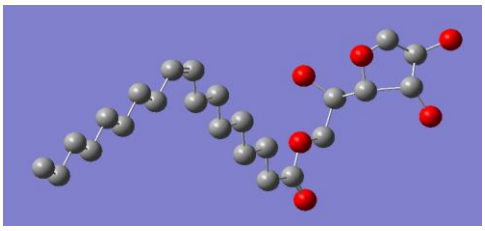

Figure 1: Geometry of Span80. Head consists of a five member ring.

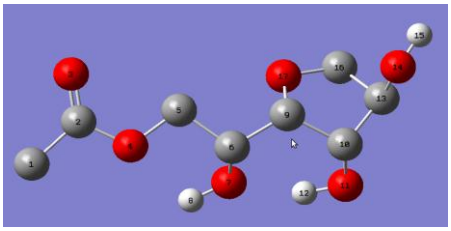

Figure 2: Head region of the Span80. The tail was removed to reduce the computational burden for ab-initio calculations.

Ab-initio calculations

Ab-initio calculations were done using Gaussian-09 package. HF/6-311 G(d) basis set was used to do a relaxed PES scan. The most relevant dihedral angle is the one connecting the ring part of Span80 to the rest of the molecule and it is determined by the following four atoms C5-C6-C9-C10 (c.f. figure 2). A simple relaxed scan around this dihedral still presents some difficulties due to a strong coupling with the configurations of the ring and the orientations of the three neighboring hydroxyl groups, O7-H8, O11-H12, and O14-H15. As a result, a full scan around the dihedral fails to provide an accurate torsional profile as the molecule gets easily stuck in a local minimum. The local minima are determined largely by the change in the orientation of the hydroxyl groups. To avoid this unphysical behavior, we have proceeded with a multi dihedral scan, whereby, the two hydroxyl groups on the ring are rotated by 360^{o}. in intervals of 60^{o}, for every value of the torsion angle D[C5-C6-C9-C10]. The O7-H8 group does not vary significantly, hence its rotations were not considered. This significantly increases the amount of calculations as 36 calculations are required for every scan step of the dihedral angle. However it provides a very satisfactory description of energy profile. In future, we aim to improve the ab-initio calculations by redoing single point energy calculations on geometries obtained from the scan using MP2 or higher theory.

MD calculations

Molecular geometries are extracted from the output of the Gaussian scan. This serves as a starting point for MD calculations. Molecule geometries are used to perform single point energy calculations with GROMOS-53a6 force field. However, same ab-initio calculations can be used to reparametrize other force fields.

Charges

There are many ways to determine the partial charges on the molecule. Typically, charges may be obtained from the literature, but they do not always conform to the geometry of the molecule. Instead, reliable BCC and Mulliken charges are be obtained from MOPAC and Gaussian calculations, respectively. Mulliken charges, from the basis set we use, turn out to be slightly larger than BCC charges. Moreover, BCC charges seem to carry the right partial charges for the hydroxyl groups. Hence, for now, we have preferred to use BCC charges. In Table 1, we have listed BCC and Mulliken charges for the united-atom structure in fig. 2.

Bond and Angle parameters

Bond stretching parameters are taken as such from the literature by searching equivalent atom groups. These do not have a great impact on the overall dynamics related to micellization. Angle bending parameters for most of the tail and well known functional groups are also taken from the literature. Bending parameters for the carbon and the hydrogen on the ring need to be modified in conjunction with the dihedral parameters to obtain the best energy fits across all geometric configurations. Without it, conformation changes of the ring might not be accurately reproduced. Since a 3D structure from Span-80 and the knowledge of its confirmations is not available from experiments or from literature, we have proceeded with a minimal change to the bending parameters as well.

Atom	BCC charge	Mulliken charge			
C1	0.08	0.04	C10	0.25	0.33
C2	0.64	0.57	O11	-0.59	-0.73
O3	-0.53	-0.45	H12	0.42	0.47
O4	-0.47	-0.47	C13	0.14	0.13
C5	0.26	0.34	O14	-0.59	-0.69
C6	0.18	0.27	H15	0.4	0.43
O7	-0.61	-0.74	C16	0.21	0.35
H8	0.42	0.45	O17	-0.41	-0.5
C9	0.19	0.2			

Table 1: Table showing a comparison of BCC and Mulliken charges from MOPAC and Gaussian calculations respectively

Torsional parameters

As mentioned earlier, a multi dihedral scan provides the best resource for energy minimization across various conformations. The main torsion D[C5-C6-C9-C10] is rotated in steps of 5^o. For every scan step, the two hydroxyl groups are rotated through 360^o in intervals of 60^o. Single point MD calculations are then run on the structures extracted from the relaxed scan. These calculations are then run iteratively with different values of the torsional parameters to obtain the best fit to all structures. At this point we have neglected structures with energy greater than 15 kcal from the minimum energy. In a more rigorous approach all configurations will be used to fit the energy profile, using appropriate Boltzmann weights. In figure 2, we have plotted energies obtained from

Gaussian ab-initio calculations against those obtained using AMBER and GROMOS-53a6 force field. Only a single configuration of O11-H12 and O14-H15 hydroxyl groups is represented in the Fig 3. Parameter fitting has to be done over all 36 configurations corresponding to different torsional angles for these OH groups.

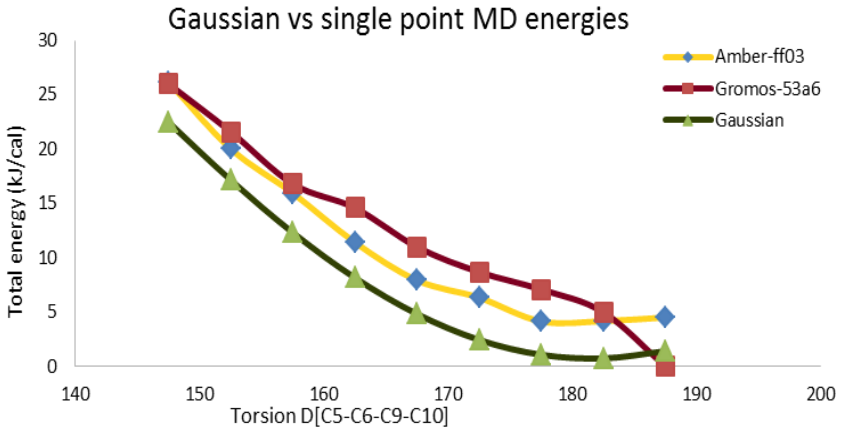

Fig 3:

Figure 3: Total energies from a relaxed PES Gaussian scan are compared against single point energies from GROMOS-53a6 and Amber-ff03. Molecule geometries used for the MD calculation were extracted from the Gaussian log files.

3. Summary and Conclusion

We have developed and tested an efficient method for re-parameterization of novel molecules like Span80. Further improvements can be made by using higher level of theory for *ab-initio* calculations. Next we plan to exhaustively apply this method to obtain optimum topologies for Vitamin E and other important biological relevant amphiphiles such as bile salts, for which topologies cannot be reliably obtained from the established force filed databases.

4. Acknowledgments

The current work is funded by the NSF EPSCoR LA-SiGMA project under the award #EPS-1003897. The computations were performed using Gaussian-09 and AMBER packages on LONI clusters.

5. References

[1] C. Oostenbrink, A. Villa, A. E. Mark and W. F. V. Gunsteren, A biomolecular force field based on the free enthalpy of hydration and solvation: The gromos force-field parameter sets 53a5 and 53a6. *Journal of Computational Chemistry*, 25(13), 2004, 25, 1656-1676.

[2] J. Wang, R. M. Wolf, J.W. Caldwell, P.A. Kollman and D. A. Case, Development and testing of a general amber force field, *Nature* 464(7286), 2010, 199.

[3] A. W. Schuettelkopf and D. M. F van Aalten, *Acta Crystallograpgica*, D60, 1355 (2004).

Diffusion in Confined Geometries

Divya Narayan Elumalai[1], Pedro Derosa[1,2], Kirill Arapov[1], Yuri Lvov[1]

[1]Institute for Micromanufacturing, Louisiana Tech University
[2] Department of Mathematics and Physics, Grambling State University

Abstract: Nanotubes show exceptional properties that make them promising candidates for applications that require the transport of fluids or the storage of Molecular systems. In order to implement potential applications, transport properties and interactions such as adsorption, and diffusion must be understood. Experimental results show a delayed diffusion of anticorrosive agents form halloysite nanotubes. In order to understand the reason as to why this occurs, it is important to study the nature of the mechanisms that either inhibit or encourage diffusion through these nanostructures. Addressing each interaction involved individually using simulations helps us successfully model the diffusion of particles through nanotubes as a function of the interaction between the diffusing particles and the nanotube walls.

Keywords: Diffusion, Nanotubes, Nanostructures, Halloysite, Sustained Release, Corrosion Inhibitors

1. Introduction

A wide variety of applications and characteristics of nano structures have been studied to date, interesting applications have been designed and developed using nanotubes. Experiments based on the slow diffusion or the change on the diffusion rate of molecules or entities loaded into nanotubes in different media, are now of a common nature in wide ranging fields. Applications ranging from the prolongation of the rust coatings on metal tubes in extremely hazardous environments to the selective delivery of anti cancer drugs to specific cancer cell types are but few of the application that have been explored [1,2]. In is our endeavor in this paper to present some experimental data on diffusion through clay nanotubes and to present a model that explains the interactions that occur during the process of diffusion to help us better understand the mechanisms of diffusion in these regimes. This study also attemps to explain two totally opposing experimental observation on the diffusion in nanotubes. Studies with clay nanotubes predict a slow out-diffusion of drug molecules from the nanotube interiors in a paper by one of us [5], whereas carbon nanotubes exhibit an extremely fast out-diffusion of water molecule described in a paper by Holt et al [6]. This apparent disparity of phenomena serves to enhance the complex nature of the problem. In this study the approach has been to study the effect of a number of interactions between particles and nanotube on the diffusion as a way to elucidate what could be responsible for such behavior.

2. Experimental Procedure

Halloysite clay tubes are aluminum-silicate hollow cylinders with a length of ca 1 μm, an outer diameter of 50 nm and a lumen of 15 nm. These nanotubes are used for loading and sustained release of corrosion inhibitors. We demonstrate that the nanotubes entrap anticorrosion agents in the inner lumen and release them in the coating defect points where they are exposed to humid environment. Inhibitors may be retained inside the tubes doped into the paint for infinitely long periods. The inhibitors are released in the coating defect spots with initial bust to suppress the corrosion process, followed by 20-50 hours curing. Longer release can be achieved through tube openings stopper formation. A sustain corrosion protection in simulated sea water over 6 months was demonstrated. Mechanisms of slowing release from halloysite are studied in terms of nano-pore controlled release. The self-healing effect in the metal coating doped with inhibitor loaded halloysite nanotubes is studied in-situ with the scanning vibrating microelectrode technique monitoring the corrosion spots anodic activity. Doping of paint with 5 % of halloysite nanotubes not only adds anticorrosion functionality but also increases the strength and hardness of the coating. Assembly of the stoppers at the tube's ends further perfects these nanocontainers but also needs simulation support to achieve viable outcomes. By variation of internal fluidic properties and creation of smart caps at the tube ends it is possible to develop a wide range of release rates. In this transformative research, we focus on novel coating material with integrated nano and micro features, and it will be available in tons which is unique for nanotechnologies. All suggested processes are "green"; occur in aqueous solutions and under mild conditions. When the most efficient chromate based anticorrosion coatings are forbidden because of their carcinogenic effects, development of smart nanocontainers for efficient environmentally friendly chelate agents (e.g. benzotriazole) is especially important.

2.1 Simulations

A Monte Carlo model implementing a forced random-walk algorithm is used to model the diffusion of particulate entities from the nanotubes. In this study the diffusion of particles in tubular nanostructures is modeled as a function of the interaction between particles and the nanotube walls; it is hypothesized that the delay in the diffusion rate is not overtly dependant on particle-particle interaction in the confined interiors of nanotubes but rather due to a strong interaction between the nanotube walls and the particles. Our algorithm generates combinations of the most probable motion of the particles in the nanotubes which are then streamlined to predict the diffusion paths and times. The overall energy of the system is calculated with contributions from particle-wall and particle-particle interactions. The wall-particle interactions are modeled by summing up the contributions from dipole-charge interactions, shielded Columbic interactions coupled with Van Der Waals interactions at short distances. Particle-particle interactions are modeled primarily by taking into consideration columbic interactions, Van Der Waals contributions are also considered. The shielding is introduced by implementing a modified Debye-Huckel screening model.

The results from the experiments conducted on halloycite nanotubes are presented in figure 1. As can be seen there is a delay in diffusion or release of the anticorrosive agents from the nanotubes. The reason for this delay is what the simulations have tried to study and explain.

3. Results and Discussions

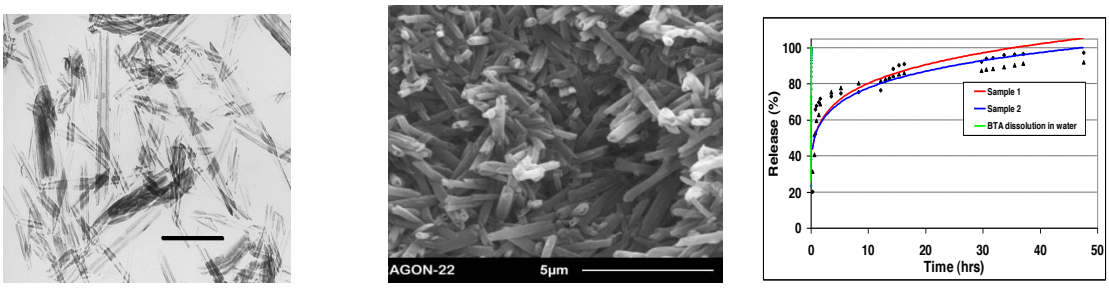

Fig.1 a & b) TEM and SEM images of halloysite nanotyubes , and c)-Benzotriazole release profiles from two halloysite samples from different batches compared with its almost instantaneous powder dissolution -green curve (water, pH 6.5)

For fixed values of temperature, particle size and maximum jump distance, for a repulsive interaction between the particles and the wall, the particles experience a squeezing effect. The smaller the nanotube radii the faster the diffusion when compared to the larger radii. Figure 2a shows that the slope of the mean square displacement curves decrease with an increase in radius. This implies that as the tube radius is smaller, the diffusion rate increases, in that sense this is a squeezing effect. The thinner nanotubes push out the like charges faster. There is more repulsion experienced by the particles when the radius is smaller. In Figure 2 b) the mean square displacement curves for attractive interaction between the walls of the nanotubes and the paricles in show. The effect in this case is the opposite the smaller radii the smaller the the slope of the mean square displacement, indicating that the diffusivity is smaller. This could explain the experimental findings, a strong particle-wall attraction, keep the particle near the wall and prevent them from diffusing as fast as when freee diffusing. The smaller the tube the larger the effect.

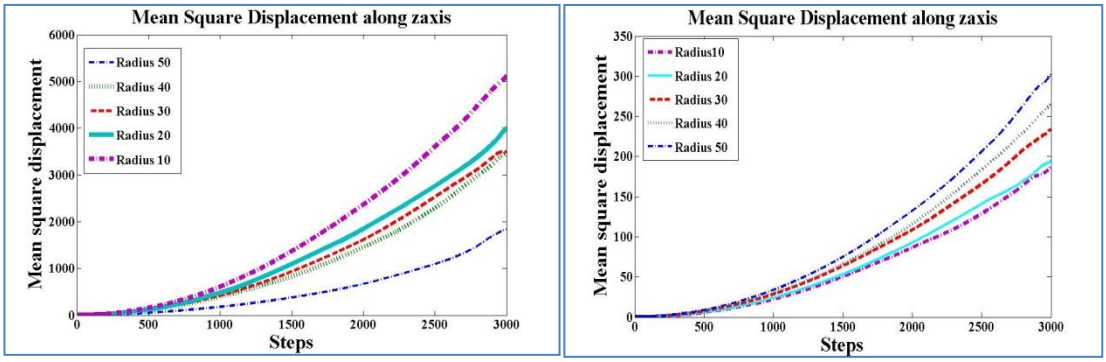

Fig.2 a) Mean square displacement curves along the axis of the tube for repulsive interactions between the wall and the particles for different radii. b) Mean square displacement curves along the axis of the tube for attractive interactions between the wall and the particles for different radii.

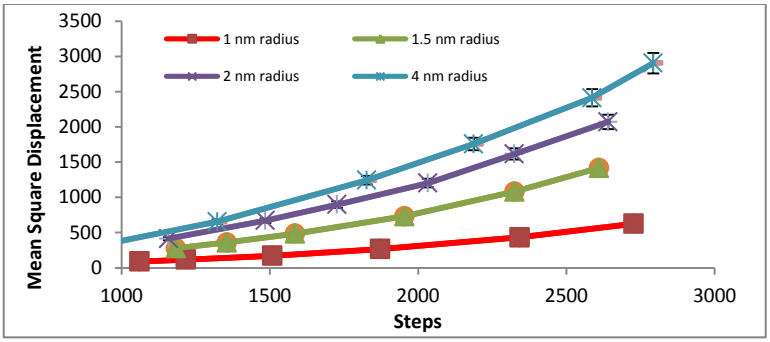

Fig.3. Changing particle size keeping all other factors fixed.

4. Conclusion

Experimental results show a marked delay in diffusion of Benzotriazole from halloysite when compared to instantaneous powder dissolution. Simulation studies show that a particle-wall attraction lead to a delay in the diffusion of species, i.e. the rate of diffusion is decreased. A simple coulombic interaction, shielded by a dielectric media seems to be enough to explain the diffusion delay. On the other hand, a repulsive coulombic interaction between the particles and the wall, leads to a clear increase in the diffusion rate, this is probably explaining the second set of experimental results, showing a fast diffusion in carbon nanotubes. This proof-of-concept work laid out the ground for furthers studies aiming and not only understanding the diffusion but controlling its rate, a proposed use is drug delivery, further study is expected to lead to a recipe where the diffusion rate can be then controlled as needed, this is fundamental for the successful use of this technology for the controlled release of drugs.

5. Acknowledgments

The current work is funded by the NSF EPSCoR LA-SiGMA project under award #EPS-1003897.

6. References

[1] E. Abdullayev, Y. Lvov, Ch. 3 in book: "*Active Coatings Based on Nanocontainers,*" Eds. D. Shchukin, H. Möhwald, Wiley Publ., London, Berlin, 2011.

[2] K.F Teker, *et al., NanoBioTechnology,* Vol. 1, No. 2, 171-182 Jun. 2005.

[3] J. Chłopek, *et al., Carbon*, Vol. 44, Issue. 6, 1106-1111, May 2006.

[4] S. Prentner, *et al., Blood*, 4-7, Apr. 2009.

[5] J.K. Holt, *et al.*, *Science*, 312(5776): 1034-7, 19 May 2006.

[6] R. R. Price, B. P. Gaber, Y. Lvov, *J. Microencapsulation,* Vol. 18, No. 6, 713-722, Nov. 2001

[7] E. Abdullayev, Y. Lvov, ***J. Materials Chemistry***, Vol. 20, 6681-6687, 2010,

[8] D. Liu, D. Dai, Y. Lvov, ***J. Computational Theoretical Nanoscience*****,** Vol. 8, 168-178, 2011.

Electronic Structure of Charged Single-Walled Carbon Nanotubes

Gary G. Hoffman and Lawrence R. Pratt

Department of Chemical & Biomolecular Engineering, Tulane University

Abstract: The electronic structure of a series of capped carbon nanotubes of different lengths and charges was investigated. For a given length, the energy as a function of charge is used to deduce the capacitance of the structure and, using the dependence of this quantity on the length, an estimate for the capacitance of a macroscopic nanotube is deduced. These results are compared with those for similarly shaped classical conductors, indicating that the electrical behavior of these carbon nanotubes is well described with a classical model.

Keywords: Single-walled carbon nanotube, electronic structure, capacitance

1. Introduction

A method for synthesizing carbon nanotubes was reported[1] in 1991. The unusual mechanical and electrical properties of these structures have prompted proposals for their use in novel electronic devices[2]. Single-walled carbon nanotubes have narrow diameter, can be packed tightly,[4] and carry electrical currents at high densities.[3] These characteristics support the suggestion that they be used as high specific surface area electrodes for *supercapacitors*.[5]

A non-zero charge on these nanometer-scale electrodes should to influence the properties of the nanotubes and this report studies those effects. The electronic structure was computed for finite-length, capped nanotubes and the charge distribution and energy dependence analyzed. The dependence of the energy on charge was used to estimate the intrinsic capacitance of these structures and the dependence on length used to extrapolate these results to macroscopic length tubes.

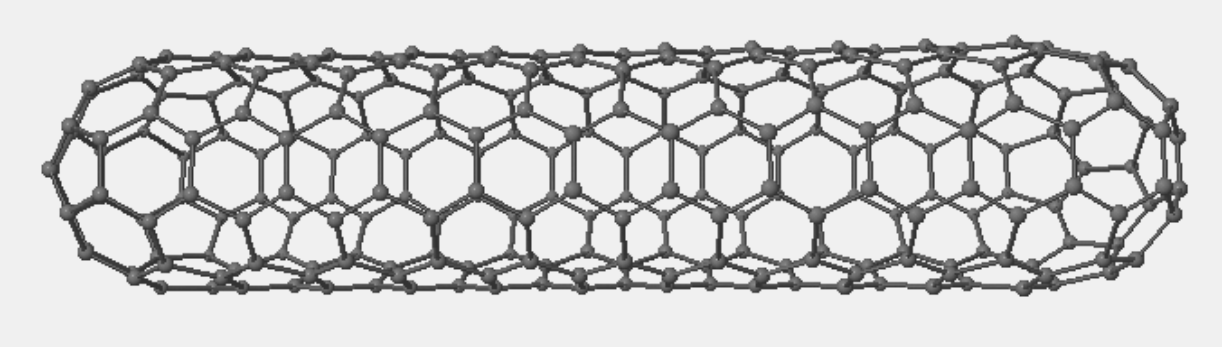

Figure 1: The capped 200-atom nanotube structure.

Calculations on charged, finite-length, capped nanotubes have been reported elsewhere in the literature.[6-9] Those studies, however, used the local density approximation (LDA) and did not study more than one length of nanotube. The current study uses a generalized gradient approximation and looks at a range of nanotube lengths.

We studied various lengths of (5,5) carbon nanotube, ranging from 120 to 300 atoms, each end being capped with hemi-buckyball (Figure 1). Electronic structure calculations were performed with *Gaussian 03*[10] using the PBE density functional[11] and the 3-21G split-valence basis set.[12]

2. Results

Figure 2 presents the average atomic charges for several cases along the 160-atom capped nanotube.

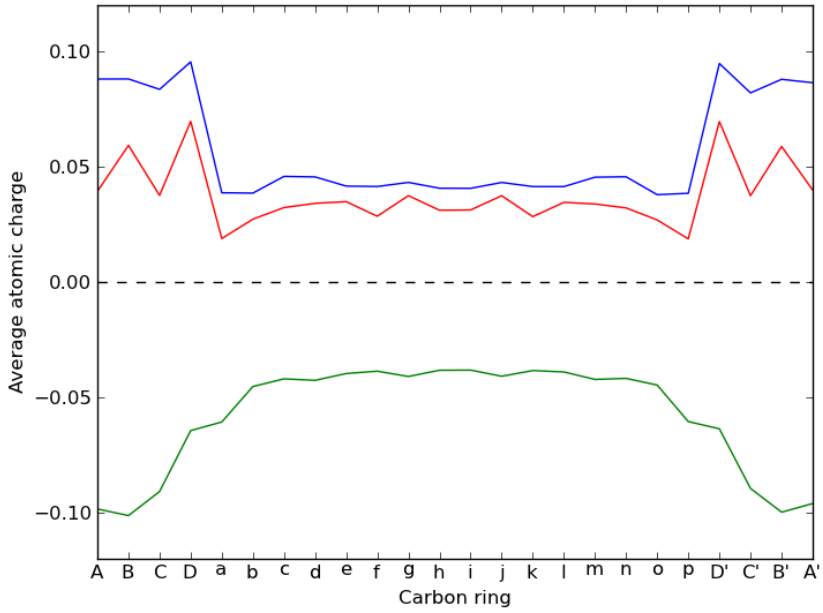

Figure 2: Average atomic charges along the 160-atom capped nanotube. The blue curve corresponds to a total charge of +12 for the system and the green curve corresponds to a total charge of -12. The red curve corresponds to a total charge of +8.

The charges along the tube portion, *a* through *p* in the figure, remain fairly constant, showing noticeable deviation only on the rings closest to the caps. The caps typically have a larger magnitude average atomic charge than the tube portion, as might have been predicted based on classical electrostatics.

The energies of these structures, when plotted *vs.* charge, are very well fit by quadratic curves for all nanotube lengths (Figure 3). In addition to the quadratic dependence, it is found that the minimum energy for all structures occurs for a negative charge. That is, these structures tend to be electronegative. This behavior has been observed in other calculations reported in the literature.[9]

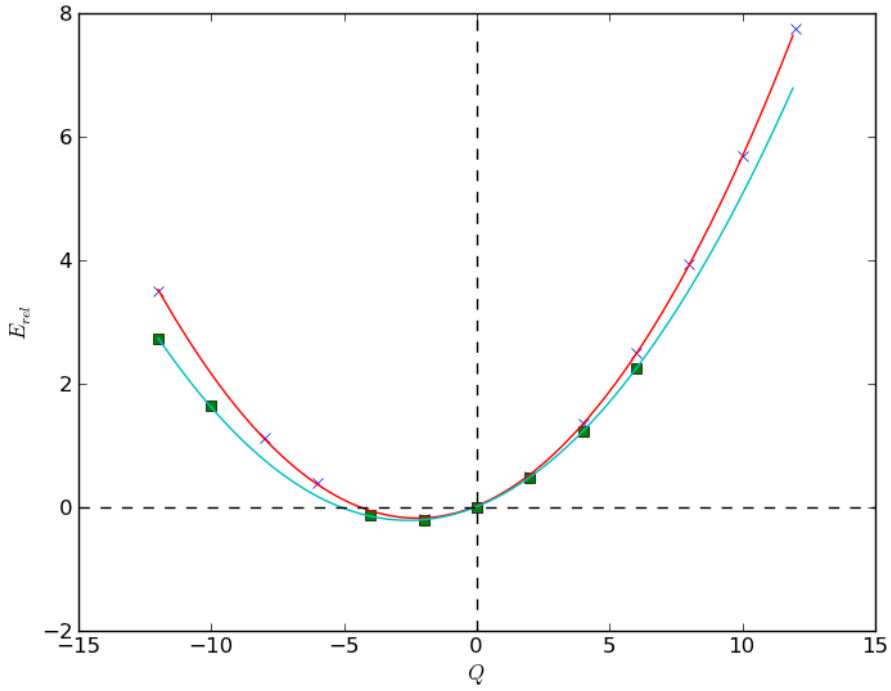

Figure 3: Energy of the capped nanotube, relative to the neutral system, as a function of total charge. This plot shows the data for the 120-atom nanotube (blue crosses) and the 180-atom nanotube (green squares). Least squares quadratic fits are also shown.

A quadratic dependence of the energy on charge is a characteristic exhibited by classical conductors[13] and is associated with the capacitance of the object. Table 1 includes the capacitances, $C^{(q)}$, computed from quadratic fits to the computed energies. Also included in the table are the classical capacitances, $C^{(c)}$, of ellipsoidal conductors constructed to have the same lengths as the capped nanotubes as well as the same surface area. The values are all close to those for the nanotubes, being within 5-7%. This suggests that the capacitance properties of the capped nanotubes should be described well by the corresponding classical conductor.

These data can be extrapolated to macroscopic dimensions. The nanotube contribution to the energy should be linear in nanotube size and this linear contribution should provide a capacitance per unit length of nanotube. An analysis of the data yields the result of $C_n = 12$ F/g. The electronegativity of the nanotube is retained in the mac-

roscopic limit as well. The atomic charge at the energy minimum maintains a value of -0.007 to -0.008 in units of electron charge.

TABLE 1: Capacitances of the capped nanotubes, $C^{(q)}$, based on fits of the energy to a quadratic dependence on the charge compared with the capacitances of ellipsoidal conductors, $C^{(c)}$, of comparable dimensions.

# atoms	$C^{(q)}$ (10^{-20} F)	$C^{(c)}$ (10^{-20} F)
120	7.552	6.993
140	7.990	7.405
160	8.390	7.821
180	8.831	8.207
200	8.965	8.599
300	10.982	10.447

3. Conclusion

Electronic structure calculations indicate that the carbon nanotubes are electronegative and have capacitances comparable to those for classical conductors of similar shape and size; the capacitance behavior of these structures can be well modeled by classical electrostatics.

The electronegativity is retained in extrapolation to macroscopic length, suggesting that macroscopic nanotubes are highly electronegative. The intrinsic capacitance of a macroscopic length single-walled nanotube is estimated to be $C_n = 12$ F/g.

4. Acknowledgments

The current work is funded by the NSF EPSCoR LA-SiGMA project under award #EPS-1003897.

5. References

[1] S. Iijima, *Nature* 354, 56-58 (1991).
[2] C. Dekker, *Phys. Today* 52, 22-28 (1999).
[3] F. Léonard, *The Physics of Carbon Nanotube Devices*, (William Andrew, Norwich, 2009).
[4] D. N. Futaba, *et al.*, *Nature Materials* 5, 987-994 (2006).
[5] Y. Zhu, *et al.*, *Sciencexpress* 12 May 2011, DOI:10.1126/science.1200770 (2011).
[6] L. Lou, P. Nordlander, and R. E. Smalley, *Phys. Rev. B* 52, 1429-1432 (1995).
[7] C. Kim, B. Kim, S. M. Lee, C. Jo, and Y. H. Lee, *Appl. Phys. Lett.* 79, 1187-1189 (2001).
[8] J. Luo, L.-M. Peng, Z. Q. Xue, and J. L. Wu, *Phys. Rev. B* 66, 115415 (2002).
[9] J. Luo and J. Wu, *Science in China, Ser. G Phys., Mech. & Astron.* 47, 685-693 (2004).
[10] Gaussian 03, Revision E.01, M. J. Frisch *et al.*, Gaussian, Inc., Wallingford, CT}, 2004.
[11] J. P. Perdew, K. Burke, and M. Ernzerhof, *Phys. Rev. Lett.* 77, 3865-3868 (1996).
[12] J. S. Binkley, J. A. Pople, and W. J. Hehre, *J. Am. Chem. Soc.* 102, 939-947 (1980).
[13] J. D. Jackson, *Classical Electrodynamics, Third Edition*, (John Wiley & Sons, Inc., New York, 1999).
[14] W. R. Smythe, *Static and Dynamic Electricity, Third Edition*, (McGraw-Hill Book Co., New York, 1968), pp. 121-124.

First Principle Study of Electronic Properties of Rutile Titanium (IV) Oxide

E. C. Ekuma[1], J. Moreno[1, 2], M. Jarrell[1, 2], and D. Bagayoko[3]

[1]Center for Computation & Technology, Louisiana State University, Baton Rouge, LA 70803
[2]Department of Physics & Astronomy, Louisiana State University, Baton Rouge, LA 70803
[3]Department of Physics, Southern University and A&M College, Baton Rouge, LA 70813

Abstract: We present *ab-initio* and self-consistent calculations of the electronic structure and related properties of titania. We utilized a local density functional (LDA) potential and the linear combination of atomic orbital (LCAO) formalism. Using the the Bagayoko, Zhao, and Williams method, we solved self-consistently both the Kohn-Sham equation and the equation giving the ground state charge density in terms of the wave functions of the occupied states. We predict a calculated, indirect, optical band gap (cBMin –vBMax) of 2.95 eV, from Γ to *R*, for rutile TiO_2.. We found a slightly larger, direct band gap of 3.05 eV, at the Γ point, in excellent agreement with experiment. We discuss the electronic energies, with emphasis on the low-laying conduction bands and the band gaps.

Keywords: DFT-LDA, BZW method, ab-initio self-consistent calculations, TiO_2, Band gap.

1. Introduction

Rutile Titanium (IV) oxide (TiO_2) is the most stable among its several polymorphs. Its electronic properties have been extensively studied for the past several decades, owing to its great potential, technological applications. TiO_2 has been used as transparent conducting oxides, in resistive memories, in spintronic devices, and in photo-catalysis for solar energy utilization [1-2].

Computational studies of rutile TiO_2 (Titania) have had difficulty in reproducing some important parameters that are accurately determined by experiment. For instance, previous band structure calculations mostly reported band gaps that disagree with experimental results.

One of the earliest theoretical studies of the band structure of Titania was the linear combination of muffin-tin orbitals (LCMTO) work of Kasowski and Tait [3]. These authors found a direct band gap of 3.25 eV. Grunes et al.[4], using the extended Haeckel tight-binding method, predicted a direct band gap of 2.80 eV. From the mid-1980s to present, several other theoretical computations have followed the ones above [5-6]. In summary, the LDA results for the band gap of rutile TiO_2 range from 1.67 eV to 3.25 eV while the experimentally measured ones are from 3.0 eV to 3.10 eV.

We aim to employ the Bagayoko, Zhao, and Williams (BZW) method to calculate the band gap and other electronic properties of rutile TiO_2. The mathematical rigor of the method and the confirmation of our earlier successful predictions of band gaps and other properties of semiconductors [7] indicate that this work could shed light on the electronic properties of TiO_2.

2. Method

Our computational method employed the linear combination of atomic orbitals (LCAO). In this approach, the unknown wave function for the solid state calculation is written as a linear combination of atomic orbitals. These orbitals are generally exponential or Gaussian functions resulting from self-consistent calculations of energy levels of the atomic species that are present in the solid under study. We use Gaussian functions and refer to that rendition of LCAO as the linear combination of Gaussian orbitals (LCGO).

We employed the local density potential (LDA) of Ceperley and Alder [9] as parameterized by Vosko, Wilk, and Nusair [10]. In all our computation, no shape approximation on either the potential or the charge density is made. The computational error for the valence charge was 5.3×10^{-5} per valence electron. The self-consistent potential converged to a difference of 10^{-5} after about 60 iterations. We utilized the electronic structure calculation package developed at the Ames Laboratory of the US Department of Energy (DOE), in Ames, Iowa [11]. Our self-consistent calculations were performed at the room temperature experimental lattice parameters of a = 4.59373 Å and c = 2.95812 Å, with u = 0.3053 [12].

The distinctive feature of our calculation consists of the implementation of Bagayoko-Zhao-Williams (BZW) method [8]. With this method, the system of equations defining LDA is solved self-consistently, as required by the derivation of LDA [13]. Upon the selection of an LDA potential, this system reduces to two equations which are that of Kohn and Sham and the one giving the ground state density in terms of the wave functions of the occupied states.

We performed self-consistent calculations of the electronic properties of Ti^{2+} and O^{1-} to obtain the inputs for the solid state calculations. The Brillouin zone (BZ) integration for the charge density in the self-consistent iteration were carried out using 60 special k points, with proper weights, in the irreducible Brillouin zone. The energy eigenvalues and eigenfunctions were subsequently calculated at 141 special, weighted k points to produce the band structure. We employed 147 weighted k points in the irreducible BZ of rutile TiO_2, to generate the energy eigenvalues for the electronic density of states computations using the linear, analytical tetrahedron method [14].

3. Results and Discussions

Following the BZW method, we performed successive, self-consistent calculations of the electronic properties of TiO_2. A total of six self-consistent calculations, beginning with the one employing the minimal basis set, were carried out. The optimal basis set was that of Calculation IV. Figs. 1 and 2 show the electronic energies and the total density of sates, respectively.

From Fig. 1, we see that the minimum of the conduction band occurs at the R point while the maximum of the valence band is at the Γ point, resulting in a predicted, fundamental, indirect gap of 2.95 eV. Our calculated direct band gap of 3.05 eV, at the Γ point, is only larger by 0.10 eV. These results somewhat corroborate experimental reports of direct and indirect transitions that are nearly degenerate [15-16]. Our calculated, direct gap of 3.05 (i.e., 3.046 eV) is in excellent agreement with experiment. Also, our calculated peaks in the total density of state (DOS) (see Fig. 2), for the valence band, are found to agree with experiment [17].

A distinctive feature of the electronic band structure is that it consists of groups of bands that are well separated. This feature is apparent in both Fig.1 and Fig. 2. The lowest laying valence bands are mostly of O-2s character, with a little hybridization with the Ti-p and Ti-s states. The conduction band minimum at the Γ point consists of two energetically close bands. The calculated energy difference between these two bands is only 0.12 eV, in agreement with the 0.11 eV separation observed by Persson and da Silva [18].

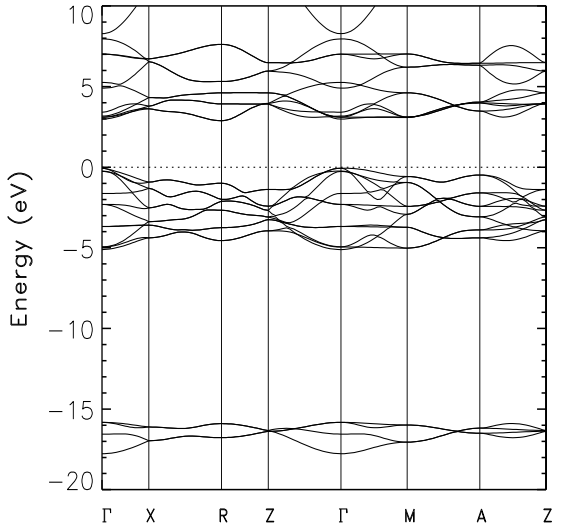

Fig. 1. The calculated, electronic energy bands of rutile TiO_2 as obtained with the optimal basis set. The calculated direct band gap of 3.05 eV is practically the same as the experimental one. (i.e., 3.0 eV to 3.10 eV). The minimum, indirect gap, from Γ to R, is 2.95 eV. The horizontal, dashed line indicates the position of the Fermi energy (E_F) which has been set equal to zero.

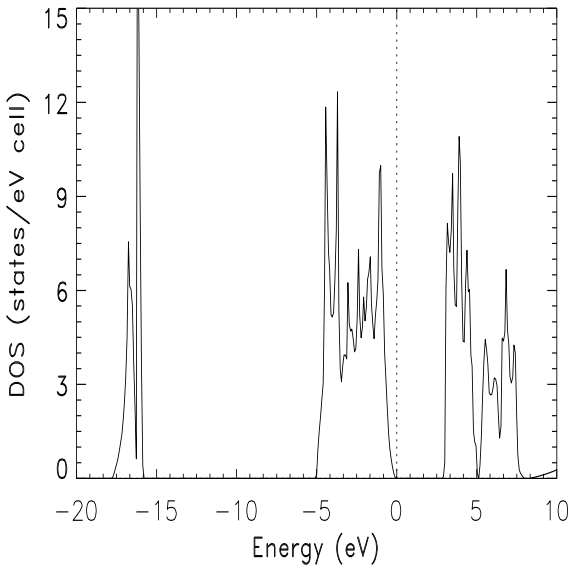

Fig. 2. The total density of states (DOS) of rutile TiO_2, as obtained from the bands shown in Fig. 1. The vertical, dashed line indicates the position of the Fermi energy (E_F) which has been set equal to zero.

4. Conclusion

We performed first principle, self-consistent calculations of the electronic and related properties of rutile TiO_2 within density functional theory (DFT), using a local density approximation potential. We utilized the linear combination of atomic orbitals (LCAO) formalism. Our ab-initio, self-consistent LDA-BZW calculations led to ground state electronic and related properties that mostly agree with experiment. Specifically, the calculated, direct band gap of 3.05 eV, at the Γ point, is in excellent agreement with experimentally reported values in the range of 3.0 to 3.10 eV. We found a calculated, indirect, fundamental gap of 2.95 eV, from Γ to R, for rutile

TiO_2. We expect the energy bands in Figure 1 to enable future comparisons with experimental measurements, from optical absorption to X-ray studies of the semi-core states.

5. Acknowledgement

This work was supported by the National Science Foundation (Award Nos. 0754821, EPS-1003897, and NSF (2010-15)-RII-SUBR) and the Louisiana Optical Network Initiative (LONI, SUBR Award No. 2-10915).

6. References

[1] Y. Furubayashi, H. Hitosugi, Y. Yamamoto, K. Inaba, G. Kinoda, Y. Hirose, T. Shimada, and T. Hasegawa, Appl. Phys. Lett. 86, 252101 (2005).

[2] M. Fujimoto, H. Koyama, M. Konagai, Y. Hosoi, K. Ishihara, S. Ohnishi, and N. Awaya, Appl. Phys. Lett. 89, 223509 (2006).

[3] R. V. Kasowski and R. H. Tait, Phys. Rev. B 20, 5168–5177 (1979).

[4] L. A. Grunes, R. D. Leapman, C. N. Wilker, R. Hoffmann and A. B. Kunz, Phys. Rev. B 25, 7157–7173 (1982).

[5] F. Labat, P. Baranek, C. Domain, C. Minot, and C. Adamo, J. Chem. Phys. 126, 154703 (2007).

[6] M. M. Islam, T. Bredow, and A. Gerson, Phys. Rev. B 76, 045217 (2007); G. Shao, J. Phys. Chem. C 112, 18677–18685 (2008).

[7] E. C. Ekuma, L. Franklin, G. L. Zhao, J. T. Wang and D. Bagayoko, Can. J. Phys., 89, 319-324 (2011).

[8] D. Bagayoko, G. L. Zhao, J. D. Fan and J. T. Wang, J. Phys.: Condens. Matt. 10, 5645 (1998). Also see G. L. Zhao, D. Bagayoko, and T. D. Williams, Phys. Rev. B. 60, 1563 (1999).

[9] D. M. Ceperley and B. J. Alder, Phys. Rev. Lett. 45, 566 (1980).

[10] S. H. Vosko, L. Wilk, and M. Nusair, Can. J. Phys. 58, 1200 (1980).

[11] B. N. Harmon, W. Weber, and D. R. Hamann, Phys. Rev. B. 25, 1109-1115 (1982).

[12] Inorganic Crystal Structure Database (ICSD), NIST Release 2011/1.

[13] W. Kohn and L. J. Sham, Phys. Rev. 140, A1133 (1965).

[14] G. Lehmann, and M. Taut, Phys. Status Solidi 54, 469-477 (1972).

[15] G. Lu, A. Linsebigler, and J. T. Yates, J. Chem. Phys. 102, 4657 (1995).

[16] H. Tang, H. Berger, P. E. Schmid, F. Lévy, and G. Burri, Solid State Comm. 23, 161 (1977).

[17] S-D. Mo and W. Y. Ching, Phys. Rev. B 51, 13023 (1995).

[18] C. Persson and A.F. da Silva, Appl. Phys. Letts. 86, 231912 (2005).

First Principles Simulation on the $K_{0.8}Fe_2Se_x$ High Temperature Structural Superconductor

Rui Guo,[1] Shizhong Yang,[1,2*] Ebrahim Khosravi,[1] Guang-Lin Zhao,[3] and Diola Bagayoko[3]

[1]Department of Computer Science/LONI, Southern University and A&M College, Baton Rouge, LA 70813
[2]LONI Institute, Louisiana State University, Baton Rouge, LA 70803
[3]Department of Physics, Southern University and A&M College, Baton Rouge, LA 70813

Abstract: Since the synthesis of the first ones in 2008, iron-based high temperature superconductors have been the subject of many studies. This great interest is partly due to their higher, upper magnetic field, smaller Fermi surface around the Γ point, and a larger coherence length. This work is focused on $A_xFe_2Se_2$ structural superconductor (FeSe, 11 hierarchy; A=K, Cs) as recently observed. ARPES data show novel, electronic structure and a hole-free Fermi surface which is different from previously observed Fermi surface images. We use *ab initio* density functional theory to simulate the electronic structure of the novel superconductor $A_xFe_2Se_2$. We compare this electronic structure with those of other Fe-based superconductors. We discuss possible explanations for the hole-free Fermi surface.

Keywords: $K_xFe_2Se_2$, superconductor, simulation

1. Introduction

Since their discovery in 2008, iron-based high temperature superconductors have continued to attraction growing attention. Till now, several types of SCs have been synthesized, (e.g., $BaFe_2As_2$, LaFeAsO, $Sr_3Sc_2Fe_2As_2O_5$). Functionally, these iron related SCs can be divided into two main groups: [i] Iron pnictide series (FeP_n, where P can be replaced by As or Bi) and iron chalcogenide (FeX, where X can be replaced by Se or Te).
For the FeP_n series, several types of structures are known. They include ternary 111, 122 type structure, [2] quaternary 1111 type structure, and quinary 32225, 42226 type structure. Simple 111 or 122 type structure usually a tetrahedral solid, is easy to synthesize and to dope. In contrast, for typical 32225 or 42226 series, the crystal and electronic structures are very complicated.

The iron chalcogenide type structure is the topic of our research and is discussed below. A typical AFe_2Se_2 sample [i, 3] is considered to be the most heavily doped with electrons [4, 5] among all the iron based superconductors that have been synthesized to date. More specifically, AFe_2Se_2 has a $BaFe_2As_2$-like crystal structure, but its chemical components are Fe-Se (11 type). [5, 6, 7]

Angle resolved photo emission spectroscopy (ARPES) results [8] for $K_xFe_2Se_2$ structure SC show a hole free, pure electron Fermi surface. The importance of studying this material theoretically resides in part in the fact that many hypotheses are based upon features of the materials, i.e., interband scattering and Fermi surface nesting. Previous

studies have shown that iron based SCs have a Fermi surface with hole in the zone center, with electrons gathered in the corner, thus the s± pairing symmetry mechanism [9] is to be questioned.

Normally, hole-doping and atom deficiency are considered to be the most probable causes of the superconductivity. [3, 6, 10, 11] Many experiments support this conclusion. To gain some insight about the novel SC structure, we performed computational simulation on $K_{0.8}Fe_2Se_2$ SC structure using density functional theory. We first introduce the method we used. We subsequently present and discuss our simulation results and we provide a short conclusion.

2. Method

We performed first principles density functional calculations using the projector augmented wave (PAW) method, taking the relativistic effects into account. [12, 13] The exchange-correlation interaction was described by the local density approximation (LDA). The Vienna ab-initio simulation package (VASP) [14, 15, 16, 17] was used in these calculations. The 3s, 3p, and 4s electron states of potassium (K) atoms were treated as as valence states. For the iron (Fe) atom, the 3d and 4s states constituted the valence states, while the 4s and 4p were the valence states of selenium (Se). The core electron states were treated as those of free atoms, in a frozen core approximation. We used a super-cell approach that included 13 K atoms, 32 Fe, and 32 Se atoms. All the atomic coordinates and unit-cell volumes were relaxed in the first principles DFT calculations. We implemented spin-polarized electron density calculations. With the plane-wave energy cutoff at 350 eV, the calculated total energies converged to the order of about 0.01 meV. The residue forces on all the atoms were less than 10 meV/Å. In the super-cell method, we used a 2×2×1 and Monkhost grids in the k space sampling for all the doping concentrations. The Bader charge [18] was calculated for all three types of atoms.

(a)

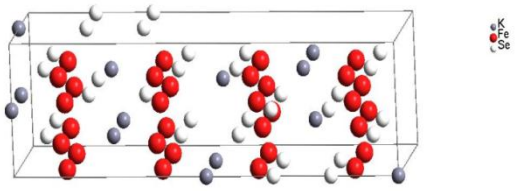

(b) (c)

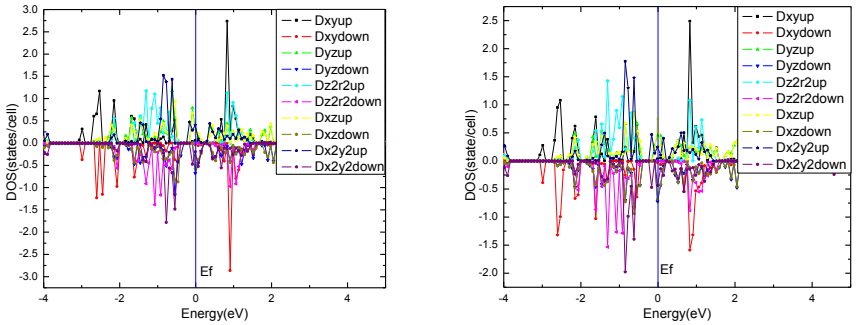

Figure 1. Supercell used in our simulation with 13 K, 32 Fe, and 32 Se atoms. The grey balls stand for K atoms, red balls for Fe atoms, and white balls for Se atoms. The optimized cell size is: 7.44 Å × 7.46 Å × 25.69 Å. (b) and (c) shows the d orbital density of states of Fe atoms with maximal positive and negative magnetic moment on first and third layer of Fe atoms, respectively.

Our original starting structure is from the $ThCr_2Si_2$ type *I4/mmm* crystal structure. The $K_{0.8}Fe_2Se_2$ was extended to $K_{13}Fe_{32}Se_{32}$ with 3 K atom vacancies in the unit cell (see Fig. 1 (a)) to get closer structure while keeping the computational expense moderate.

3. Results and discussion

We have fully relaxed the supercell $K_{13}Fe_{32}Se_{32}$ crystal structure, including atomic coordinates, cell shape, and cell size. The optimized equilibrium cell is measured as 7.44 Å × 7.46 Å × 25.69 Å. The overall cell shape is only slight distorted from the original, orthogonal one. The total number of electrons in the system studied is 539. The Bader charge transfer are about +0.8 |e| for K atoms, with 0.01 |e| fluctuation, +0.4 |e| for Fe atoms, with 0.02 |e| differences, and -0.7 |e| ~ - 0.8 |e| for Se atoms. Since K atoms are good electron donors for doping, we can think of K doping as an efficient electron controller designing and making samples novel SC materials.

From our simulated magnetic moment analysis, we see that the s and p components of the Fe atoms change very little while the d components change significantly from an Fe layer to another and within the same Fe layer. We can see from Figure 1 (b) and (c) that the d_{yz}, d_{xz}, and $d_{x^2-y^2}$ density bands have shifted along the energy axis by much larger values in (b). This shift has also been extended down, both below and above the valence band, showing a strong spin fluctuation, an indication of a possible strong spin-orbital coupling. The magnetic moments of the third layer Fe atoms fluctuate from near neutral to - $0.03\mu_B$ (down spin), while the maximal magnetic moment, $0.19\ \mu_B$ (up spin), is on Fe atoms in the first Fe layer. The strong magnetic moment fluctuation is caused by the K vacancies, which is directly involved in tuning the superconductivity features in the experiments mentioned earlier.

4. Conclusion

We have performed first principles computer simulation on the recently discovered $K_{0.8}Fe_2Se_2$ SC structure. Our results indicate that the K vacancies in the crystal distort the final equilibrium configuration. The Bader charges of the three component element atoms fluctuate very little. The magnetic moments of K and Se atoms are not as evident as those of Fe atoms. The magnetic moments of the third layer Fe atoms fluctuate from near 0 μ_B to -0.03μ_B (down spin), while the maximal magnetic moment (0.19 μ_B, up spin) is on the Fe atoms in the first layer of Fe. Thus, the magnetic moment fluctuations in different layers and within the same layer of the Fe atoms may play an important role in the novel high temperature iron-based superconductivity.

5. Acknowledgement

The work was funded in part by the NSF-LASiGMA program (Grant No. EPS-1003897 and No. NSF(2010-15)-RII-SUBR), NASA/LEQSF (2009-2012)-Phase3-03, LaSPACE/NASA (Grant number NNG05GH22H), DOE (Award Nos. DE-FE0004734 and DE-FE0003693), and the LONI institute.
* Email: shizhong_yang@subr.edu

6. Reference:

[1] I. R. Shein and A. L. Ivanovskii, arXiv, **1012**, 5164v1 (2010).
[2] C. Chao and J. H. Dai, *Chinese Phys. Lett.*, **28**, 057402 (2011).
[3] T. Shimojima *et al*., *Science*, **332**, 564 (2011).
[4] Y. Zhang, *et al*., *Nature Materials*, **10**, 273 (2011).
[5] J. A. Wilson, *J. Phys. Condens. Matter*, **22**, 203201 (2010).
[6] I. A. Nekrasov and M. V. Sadovskii, *JETP Letters*, **93**, 166 (2010).
[7] Hiroki Nakamura, *J. Phys. Soc. Jpn*., **78**, 123712 (2009).
[8] Y. Zhang, *et al*., *Nature Materials*, **10**, 273, (2011).
[9] J. Guo, *et al*., Phys. Rev. B, **82**, 180520 (2010).
[10] J. J. Ying *et al.*, *New J. Phys.,* **13**, 033008 (2011).
[11] G. F. Chen, *et al*., Chin. Phys. Lett., **25**, 3403 (2008).
[12] G. Kresse, D. Joubert, *Phys. Rev. B*, **59**, 1758 (1999).
[13] P. E. Blöchl, *Phys. Rev. B*, **50**, 17953 (1994).
[14] G. Kresse, J. Hafner, *Phys. Rev. B*, **47**, 558 (1993).
[15] G. Kresse, J. Furthmüller, *Comp. Mater. Sci*., **6**, 15 (1996).
[16] G. Kresse, J. Furthmüller, *Phys. Rev. B*, **54**, 11169 (1996).
[17] VASP 2010 manual, see website: http://cms.mpi.univie.ac.at/vasp/.
[18] R.F.W. Bader, Atoms in Molecules—A Quantum Theory, Oxford University Press, Oxford, 1990.

GPGPU Computing: Massively Parallel Accelerated Science

C.W. Moore[1], D.Z. Poliakoff[1], J. Caprino[1], S. Abu Asal[1], K.R. Rajagopalan[1], S.-X. Yang[2], E.C. Ekuma[1], S. Feng[1], Y. Fang[1], C. J. Thomasson[1], A. Papke[1], S. Hall[2], K.-M. Tam[1], S. Pathak[1], B. Thakur[1], S.L. Whittenburg[4], K. Tomko[5], J. Moreno[1,2], R. Hall[1,3], M. Jarrell[1,2]

[1]Center for Computation and Technology, Louisiana State University
[2]Department of Physics and Astronomy, Louisiana State University
[3]Department of Chemistry, Louisiana State University
[4]Department of Chemistry, University of New Orleans
[5]Ohio Supercomputing Center, Columbus, Ohio

Abstract: Advances in both the capabilities and programmability of heterogeneous computing systems has enabled the investigation of new complex problems through use of GPU parallel accelerators. This report describes the current GPU code development of algorithms of use to material scientists by the LA-SiGMA GPU group. In bringing these algorithms to the public domain, the LA-SiGMA project will lead new discoveries in materials science.

Keywords: Materials Science and Chemistry, Heterogeneous Computing.

1. Introduction

A recent trend of augmenting clusters with parallel accelerators, such as GPUs, has pushed a new realm in computational heterogeneity that requires a change in the design of parallel codes to fully exploit the inclusion of these new architectures. This push towards general purpose GPU computing has already been made at national leadership machines. The Keeneland cluster at NCSA will feature 360 GPUs and the replacement for Jaguar at NCCS, Titan, will be capable of over 20 PFLOPs of performance, enhanced with Kepler GPUs. An element of the LA-SiGMA project is to train computational scientists to take advantage of the new accelerator technology of these national leadership machines to participate in research of international relevance. Codes developed by the LA-SiGMA GPU group within a variety of material science fields. A workspace, jointly funded by the Center for Computation and Technology (CCT) at LSU and LA-SiGMA, with desktops outfitted with NVIDIA FERMI GPU cards has been in use for developing these codes which will be ported to a new cluster at LSU where one quarter of the nodes of a new LSU cluster will contain three M2090 TESLA GPU cards each.

2. General Purpose GPU (GPGPU) Computing

GPU accelerators provide a large enhancement to performance, providing cluster level performance in a desktop. In short, they devote more transistors to arithmetic logic units rather than to flow control and cache, achieving high performance by sheer number of concurrent calculations and high bandwidth to many fast shared memories [1]. The GPU is streaming processor Single-Instruction Multiple Data (SIMD) architecture. Where a modern CPU has up to six fast cores, each with its own fast memory (cache), GPUs have sets of many cores sharing

fractions of the CPU cache amount. This intuitively seems like a disadvantage, but it has the advantages of a shared memory model. Each core has registers similar to those on a CPU. Finally, the CPU cannot directly write to the GPU memory; any data movement must happen through the PCI-E bus. See Fig 1 for a summary of the architecture.

GPU programming has significant differences from traditional CPU programming. As a consequence of the SIMD architecture, a steep performance penalty occurs if different cores execute operations of different computational complexity [1], and so the GPU offers the most acceleration for applications that are perfectly parallel. With the limitation in memory size, careful memory management is required to fully exploit the fast shared memory and reduce global graphics memory traffic [2]. The programmer must ensure enough concurrent operations occur to fully use all of the GPU's cores. Finally, the computational power is so much greater than the memory speed that data reuse is critical.

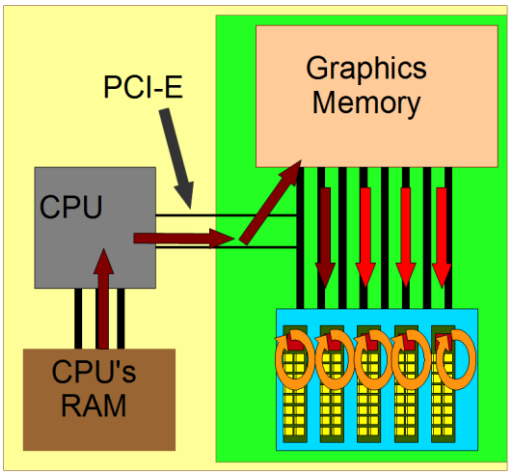

Fig. 1 Structure of a GPU accelerated CPU. The CPU communicates with the GPU via a PCIe bus. The GPU is organized into streaming processors each with tens of cores and 64 K of fast on-chip memory. The streaming processors each have high bandwidth to the global device graphics memory.

3. The Codes

The codes being developed include Hirsch-Fye quantum Monte Carlo, density matrix renormalization group, parallel tempering Monte Carlo, Monte Carlo simulations in open ensembles, Finite-Difference Time-Domain, and variational Monte Carlo.

Hirsch-Fye Quantum Monte Carlo. HFQMC [3] is primarily used as the impurity or cluster solver in Dynamical Mean Field Theory or its cluster extensions [4,5]. Proposed moves of each Markov process (MP) are cheap to make, but the full update of the Green function, a real square matrix, is an expensive rank-1 update. This update incurs as many FLOPs as memory accesses with little data reuse: impractical for a GPU implementation. To address this problem, updates are delayed or blocked together, and the full update is now a matrix product of

accumulated thin rectangular matrices that achieves much better performance through large data reuse. There is also a performance penalty associated with proposing a move in one MP while updating in another. To avoid this, moves are proposed until each of the MPs has accumulated 32 acceptances. The Green function matrix is then updated fully concurrently for each MP.

Variational Monte Carlo. VMC [6] is a powerful tool to study strongly correlated systems. A wavefunction containing adjustable parameters is assumed, and the energy of the system is minimized with respect to these parameters. A typical VMC calculation involves the use of concurrently executing Monte Carlo simulations. The outputs (e.g. energy and its gradient) are averaged, and the result is sent to a minimization routine. Inside each Markov process, several algebraic operations can be accelerated by using GPUs [7]. Moreover, several Markov processes can be concurrently executed using techniques of concurrent execution with CUDA. To handle branching efficiently, Markov tasks are to be broken into two CUDA kernels: one to propose a move and another for doing matrix updates for accepted moves. The propose kernel is called first, and then the update kernel is called to work only on the tasks with accepted moves while the propose kernel is called again for tasks with rejected moves.

Parallel Tempering Monte Carlo. PTMC [8] reduces the equilibration time of Monte Carlo simulations of magnetic materials which fail to develop long range magnetic ordering, but exhibit slow relaxation. Simulations of these puzzling materials have problems with long equilibration times and so will benefit from the speed-up provided by the GPU. The major bottleneck of this simulation is memory accesses. A multi-spin coding technique processes multiple Ising spins into one long integer, and so fits 14 replicas in one multiprocessor, eliminating many memory transactions and achieving better space utilization. Current implementation uses a pre-generated table of random integers read from the global device memory. This code will be optimized via a balanced computation to memory accesses ratio, using global memory to texture memory pre-fetching, awareness of the texture cache for random table look up, and utilizing shared memory as much as possible.

Grand Canonical Monte Carlo. GCMC simulations are used to simulate systems with fluctuating particle number [9-12]. In these simulations, the fluctuation of particle number is achieved via particle insertion/deletion moves, which are the most crucial and computer-intensive type of moves. Successful insertions of new particles are difficult in solids, glasses, and dense liquids. Efficient simulation requires the rapid "pre-screening" of potential insertion sites; for this the GPU architecture should be extremely useful. The pre-screening on particle insertions can be performed as independent parallel tasks with a reduction at the end of the screening. This makes open system simulation codes ideal targets for GPU enhancement.

Density Matrix Renormalization Group. DMRG [13] is a many-body approximation which describes the ground state properties of various lattice models, molecular systems, and even nuclear structure [14]. DMRG works by partitioning the complete Hilbert space into sites and iteratively adding them. It implements a reduced density matrix based truncation to prevent the system from growing exponentially, shrinking the Hilbert space at the cost of increasing the number of iterations [15]. The computationally expensive part of DMRG is the diagonalization of the Hamiltonian and the transformation of the operator space, after every addition step. A Lanczos based procedure is ideally suited for the diagonalization, with the matrix-vector product calculated in parallel. Transformation involves independent rotations of components of a tensor and can also be done in parallel. Both these routines are highly parallel and offer many fold speed-up via GPU accelerated modules.

Coupled FDTD-Micromagnetic-Landau-Devonshire Simulations. Finite-Difference Time-Domain (FDTD) method is a discretization of Maxwell's equations which can model the response of multiferroic materials to both applied electric and magnetic fields. For multiferroic materials, the ferromagnetic response of the material must be included via the Landau-Lifshitz equations. In multferroic materials alignment of the magnetic spins creates a magnetically-induced strain that induces an additional electric field polarization in the sample. This polarization is modeled via a Landau-Devonshire thermodynamic potential which is included as a self-consistent term in the FDTD simulation. The FDTD method is inherently parallel and so is well suited to GPU acceleration.

4. Conclusion

Like the development of CPU multicore technology, the addition of GPU accelerators has allowed for new computational problems to be tackled, but great care must be taken in the design of codes to take full use of the new architecture. This heterogeneous trend of computing has been endorsed by national leadership clusters, as they incorporate new parallel accelerators and other special hardware to push PFLOP performance. Clearly, future research in computational materials science will have to make use of these new technologies and consider them in both algorithm design and code implementation. The LA-SiGMA GPU group is developing public domain GPU accelerated codes that will enable new discovery by scientists in the collaboration.

5. Acknowledgments

We thank D. Koppelman, and J. Ramanujam, for useful conversations. This work is funded by the NSF EPSCoR LA-SiGMA project under award #EPS-1003897.

6. References

[1] NVIDIA CUDA Programming Guide ver. 2.3. NVIDIA.
[2] Kirk, D.B. and Hwu, W.W. *Programming Massively Parallel Processors.* Elsevier Inc. 2010
[3] J. E. Hirsch and R. M. Fye. Phys. Rev. Lett., 56:2521 -2564, 1986.
[4] W. Metzner and D. Vollhardt. Phys. Rev. Lett., 62:324–327, 1989.
[5] Th. Maier, M. Jarrell, Th. Pruschke, and M. Hettler. Reviews of Modern Physics, 77:1027–1080, 2005.
[6] D. Ceperley, G. V. Chester, and M. H. Kalos. Phys. Rev. B, 16:3081–3099, 1977.
[7] R. Nath , S. Tomov, and J. Dongarra. LNCS, 6449:83-92, 2011.
[8] CJ Geyer. Markov chain monte carlo maximum likelihood, computing science and statistics: Proc. 23rd symp. Interface, page 156, 1991.
[9] J. M. Rodgers, M. Webb, and B. Smit. J. Chem. Phys., 132:064107, 2010.
[10] S. S. Han, S.-H. Choi, and W. A. Goddard. J. Phys. Chem. C, 114:12039-12047, 2010.
[11] A. K. Singh, J. Lu, R. S. Aga, and B. I. Yakobson. J. Phys. Chem. C, 115:2476-2482, 2011.
[12] N. Rai, Neeraj and E. J. Maginn. . J. Phys. Chem. Lett., 2:1439-1443, 2011.
[13] S. R. White. Phy. Rev. Lett., 69:2863–2866, 1992.
[14] Letters from the past- a prl retrospective, http://prl.aps.org/50years/milestones. Phy. Rev. Lett., 2008.
[15] U. Schollwock. Rev. Mod. Phys., 77:259, 2005.

Hybrid MD-Continuum Simulation Methodology for Biomolecular Systems: LAMMPS-ANSYS/Fluent Coupling Implementation

K. Fattah-Hesary[1], N. Kim[2], S-H. Ko[2], B. Novak[1], S. Jha[2], D. Moldovan[1], and D. Nikitopoulos[1]

[1]Mechanical Engineering Department, LSU
[2]Centre Center for Computational & Technology, LSU

Abstract: A coupled CFD-MD scheme for simulating multi-scale (micro- and nano-) fluidic systems has been further developed. The coupling process involves three domains i.e. CFD, MD and an overlap hybrid region. A commercial continuum code, ANSYS/FLUENT is employed for the continuum part of the simulation, and LAMMPS is adopted for the MD part. Coupling schemes and data interfaces are implemented in ANSYS/FLUENT using its User Defined Function (UDF) capability. In the overlap region a file-based information exchange method is applied between atomistic and continuum fluidic information to define boundary conditions for the continuum region and the appropriate constraint for the atomistic one. This has set the stage for exchange of required information between the two pure regions. We validated our hybrid solution package by simulation of a sudden-start Couette flow. The results of the Couette flow simulation show quantitative agreement with results from analytical solutions. This work will leverage force-field development efforts also under the LaSiGMA grant to enable multi-scale simulations involving interactions between biomaterials for which such force-field are unknown.

Keywords: Computational fluid dynamics, Molecular dynamics, Hybrid, LAMMPS, FLUENT.

1. Introduction

Many interesting and significant phenomena in processes involving both purely biological and hybrid non-bio/bio systems occur at material interfaces and on the molecular level, while influenced by more "bulk" processes taking place on a much larger scale. Bio-molecules, such as mononucleotides or DNA fragments, interacting with natural, or functionalized/chemically modified wall surfaces in bio-analytical mixed-scale (micro/nano) fluidic instruments is a relevant example involving both bio and non-bio materials. To design such systems one must understand and resolve molecular interaction processes at material interfaces while resolving bulk transport and this necessitates the coupled simulation capabilities pursued by the present work.

The hybrid continuum and molecular dynamics (MD) approach is a simulation method which adopts the continuum hypothesis in capturing macroscopic features of a flow field and details atomistic inter-molecular interactions on interfaces of different materials by using the MD approach. This type of multiscale methods should have both the efficiency of the continuum model and the accuracy of the molecular model when necessary. Several hybrid methods of this kind have been proposed in recent years which based on the information exchanged in overlapping region can be categorized into two main classes: 1) Exchanging velocity [1]: The velocity from the continuum model is imposed on the particle dynamics in the overlapping region, and the particle

dynamics provides the velocity boundary condition for the continuum model. 2) Exchanging fluxes [2]: the fluxes of conserved quantities, including the mass flux, momentum flux and energy flux, are exchanged in the overlapping region.

In this paper we present a hybrid simulation by coupling a commercial continuum code, ANSYS/FLUENT, and an open source molecular dynamics code, LAMMPS, that builds on aforementioned works. The continuum solution is obtained by numerically integrating Navier-Stokes equations using ANSYS/FLUENT with the boundary information from MD implemented in ANSYS/FLUENT using its User Defined Function (UDF) capability. MD simulations were performed by using a modified version of LAMMPS which is a classical molecular dynamics open-source code in C++ developed by Sandia National Labs [3]. Modifications applied to LAMMPS include applying constrained dynamics which is imposed from solution of continuum part. A sudden-start Couette flow is used to test the approach and validate the results with respect to analytical solution.

2. Hybrid Method

Incompressible Navier-Stokes equations and the continuity equation are used to solve the flow in continuum region are written as,

$$\frac{\partial \vec{u}}{\partial t} + \vec{u} \cdot \nabla \vec{u} = -\frac{1}{\rho} \nabla p + \nu \nabla^2 \vec{u} \tag{1}$$

$$\nabla \cdot \vec{u} = 0 \tag{2}$$

where u is the fluid velocity, p is the pressure and $\nu = \mu/\rho$ is the kinematic viscosity. These equations are solved numerically using fractional step method which is suitable for transient incompressible flows.

In the MD simulation the interatomic interactions are described by the Lennard-Jones potential as follows,

$$U^{LJ}(r) = 4\epsilon \left[\left(\frac{\sigma}{r}\right)^{12} - \left(\frac{\sigma}{r}\right)^{6} \right] , \tag{3}$$

where r is the separation distance between atoms, ϵ is the characteristic binding energy and σ is the characteristic length, representing the molecular diameter. The potential is truncated at $r = r_c = 2.2\sigma$ and shifted to zero for computational efficiency [4].

The Verlet scheme is used for time integration of the interacting particles equation of motion to find the particles trajectories. For time integration we use time step $\Delta t = 0.001\tau$ here, where $\tau \equiv \sqrt{(\frac{m\sigma^2}{\epsilon})}$ is the Lennard-Jones characteristic time unit and m is mass of an atom.

3. Results and Discussion

We consider a sudden-start Couette flow which has been studied widely for the validation of a hybrid molecular-continuum solver [1,3]. The Lennard-Jones fluid is confined between two parallel walls at $y = 0$ and $y = 52.1\sigma$ with periodic BC's imposed along x and z axes. We consider two different cases: 1) MD region on stationary

(bottom) wall and continuum region on moving (top) wall 2) Continuum region on stationary (top) wall and MD region on moving (bottom) wall. No-slip boundary conditions are imposed on the wall at the continuum level and the wall-fluid molecular interaction parameters are chosen such that yield a no-slip condition at walls in atomistic region. At constant temperature of $T = 1.1\epsilon/k_B$ and density $\rho = 0.81\sigma^{-3}$ the fluid is in a well-defined liquid phase with dynamic viscosity of $\mu = 2.14\epsilon\tau\sigma^{-3}$ [4].

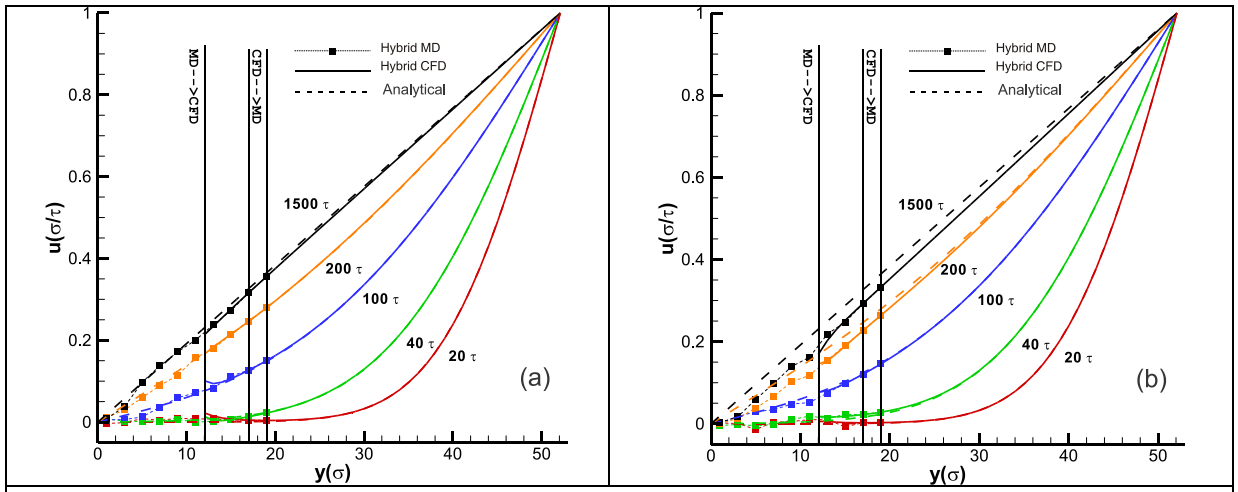

Fig 1. Velocity profiles at different times in CFD-MD hybrid simulation of sudden-start Couette flow with atomistic region on stationary (bottom) wall at two different value for the wall-fluid intermolecular interaction: *(a)* $\epsilon^{wf} = 0.6\epsilon$ and *(b)* $\epsilon^{wf} = 10\epsilon$

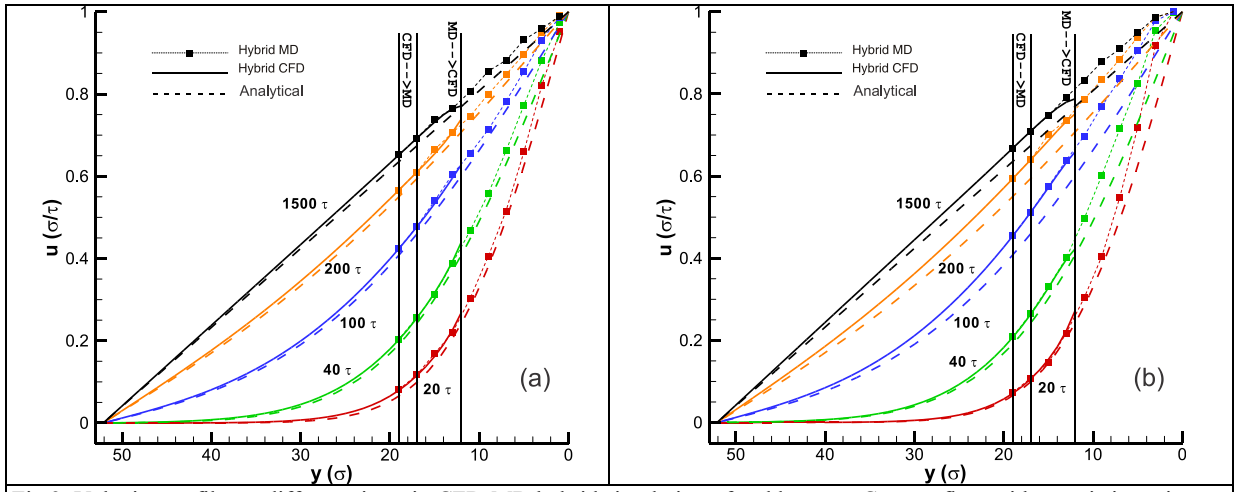

Fig 2. Velocity profiles at different times in CFD-MD hybrid simulation of sudden-start Couette flow with atomistic region on moving (bottom) wall at two different value for the wall-fluid intermolecular interaction: *(a)* $\epsilon^{wf} = 0.6\epsilon$ and *(b)* $\epsilon^{wf} = 10\epsilon$.

The results of the hybrid simulations of Couette flow for two different hybrid arrangements, one with MD on stationary wall and the other with MD on moving wall are shown in Figs 1 and 2, respectively. Two different fluid-wall molecular interaction parameters are used and presented for each arrangement. Initially, the mean fluid velocity is zero and at $t = 0$ the upper wall (Fig. 1), or the lower wall (Fig. 2), is impulsively set in motion at a constant velocity of $U = 1\ \sigma/\tau$ while the other wall is held stationary. The figures show the velocity profiles at different times from the initiation of the impulsive motion of one of the plates. At the latest times, the steady linear velocity profile is observed. It is obvious from Fig 1 (b) and Fig 2 (b) that the influence of the strong molecular interaction of the fluid with the wall material permeates into the continuum flow domain. The conditions of the problem are such that the continuum and pure MD solutions over the entire domain are both valid when interaction with both wall surfaces is consistent with a no-slip condition.

4. Conclusion

A multiscale method for hybrid simulations of MD and CFD was presented. Navier-Stokes equations are solved where continuum assumption is accurate and MD simulations are used where atomistic description is important. MD and CFD are coupled via a flux continuity imposed in an overlap region. ANSYS/FLUENT is used for continuum simulation and LAMMPS adopted for MD region. Coupling schemes and data interfaces were implemented in ANSYS/FLUENT using its User Defined Function (UDF) capability and LAMMPS was modified to include constraining the dynamics of fluid particles required for coupling in vicinity of the MD-continuum interface. The present hybrid implementation was validated by simulation of a sudden-start Couette flow. The results of the Couette flow simulation show quantitative agreement with results from analytical solutions.

5. Acknowledgments

This work is supported in part by NSF-EPSCoR, Award # EPS-1003897 (LA-SiGMA). Computational resources were provided by LONI and HPC@LSU.

6. References

[1] X. Nie, S. Chen, W. E and M. O. Robbins, A Continuum and Molecular Dynamics Hybrid Method for Micro- and Nano-Fluid Flow, J. Fluid Mech. 500, 55 (2004).

[2] R. Delgado-Buscalioni and P. V. Coveney, Continuum-Particle Hybrid Coupling for Mass, Momentum, and Energy Transfers in Unsteady Fluid Flow, Phys. Rev. E 67, 046704 (2003).

[3] S. Plimpton, Fast Parallel Algorithms for Short-Range Molecular Dynamics, J Comp Phys, 117, 1-19 (1995).

[4] S. T. O'Connel and P. A. Thompson, Molecular Dynamics-Continuum Hybrid Computations: A Tool for Studying Complex Fluid Flows, Phys. Rev. E 52, 5792 (1995).

Learning Network Using Mechatronics and Measurement Experiments

Sarat Paluri[1], Kazim Sekeroglu[1], Amitava Jana[2]

Department of Electrical Engineering[1]/ Mechanical Engineering[2], Southern University and A&M College

Abstract: Ongoing work on learning network at Southern's College of Engineering is described. This is done by considering two experiments namely 1) "Stress, Strain and Vibration Analysis of a Cantilever Beam System", and 2) "Nonlinear control system". A remote laboratory is developed for the students to interact with the experiments from anywhere. Also, we discuss on developing different domains namely simulation, experimentation and graphical interpretation for making the students understand the experiments easily.

Keywords: Remote Laboratory, LabView, Simulation.

1. Introduction

In the fast growing generation of computer and internet technology, experiments can be accessed remotely, monitored and controlled through complex and hybrid systems like remote laboratories [1]. In the present scenario, a remote laboratory is monitored and controlled over the Internet with the help of a Web browser.

Here, we are going to design an integrated remote laboratory platform that enables the instant access to real lab experiments, employing real hardware and real instrumentation to multiple users enabling the students to understand the experiment much clear and reduce the gap between theory and practice [2].

2. Development Of IT Infrastructure For Remote Experimentation

A communication infrastructure is necessary for the experiments to interact with the different types of computers and software could easily be integrated from a remote desktop computer with minimal effort via internet. In addition, network axis cameras will be integrated with the experimental workstations to view the experiments from the remote locations. To achieve these goals, the communication architecture will be divided into three layers via the internet [2].

3. System Architecture

The experiment is implemented using a data acquisition card and an experimental setup. LabVIEW performs the communication between the server in the lab and the data acquisition card with the controller module as shown in Figure 1.

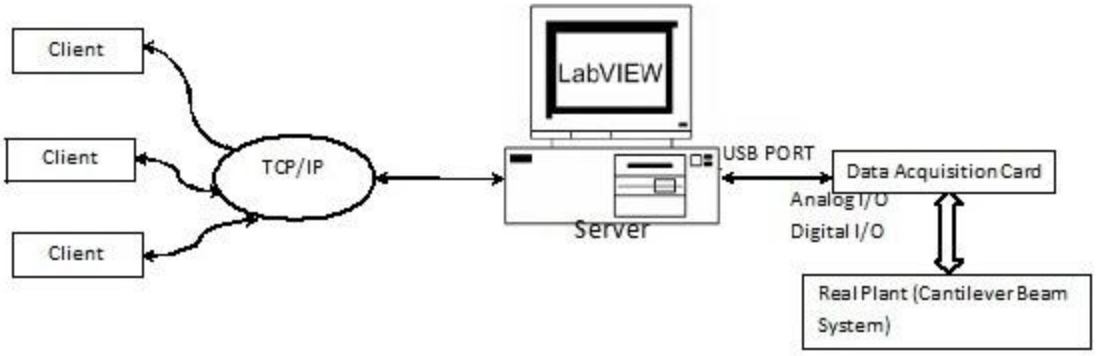

Fig. 1 Remote Laboratory Block Scheme Using Data Acquisition Card [1].

4. Simulation and Graphical Interpretation of Online Experimentation

Suitable graphical interpretation and simulation software will be developed so that the student can move back and forth to easily understand the experiment and make learning easy. The Figure 2 shows the three conventional worlds of engineering analysis which are used extensively to complement research and education.

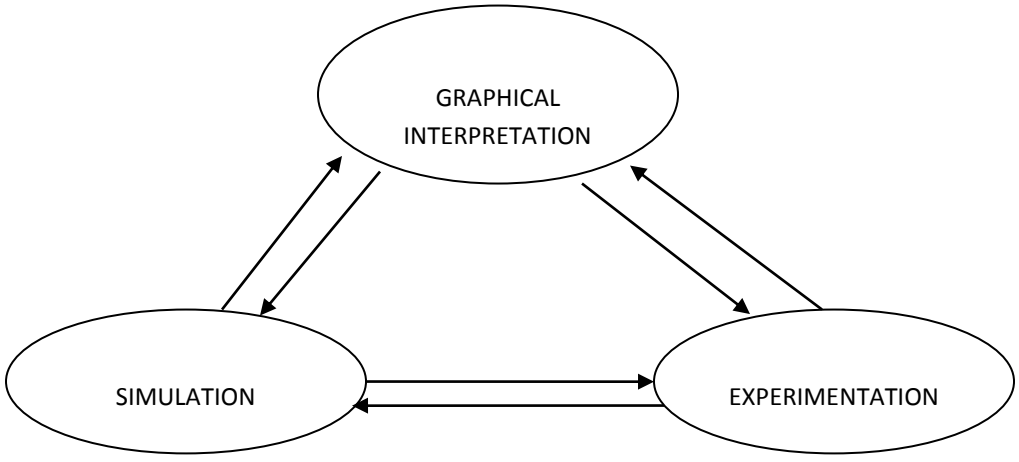

Fig. 2 Network of Engineering Analysis [2].

5. Experimental Setups

a) Material Testing

We are in the process of analyzing the forced vibrations of the continuous cantilever beam, the phenomena of resonances, the phase of the vibration signal and to obtain the fundamental natural frequency and damping ratio of the system, and compare the results with theoretically calculated values [2].

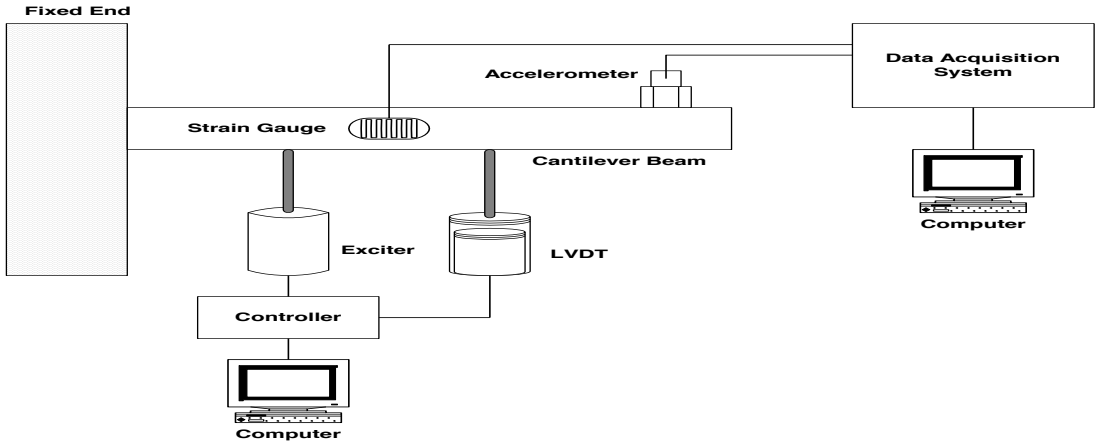

Fig. 3 Experimental Set up Of the Cantilever Beam [2]

b) Nonlinear Control System

We are in the progress of developing a nonlinear control system experiment work station namely balance beam system. Due to the complexity of the balance beam system different levels of laboratory exercise can be provided for different levels of education, and also different laboratory classes such as measurement, control or mechatronics laboratory. The basic problem of the balance beam system is to balance a beam containing two fluid tanks, one at each end, by pumping the fluid back and forth from the tanks. The Figure 4 shows the 3D model of the fluid beam balancing system. Control will be implemented on a personal computer via a data acquisition card connected to buffering and signal conditioning circuitry located on a custom made printed circuit board [3].

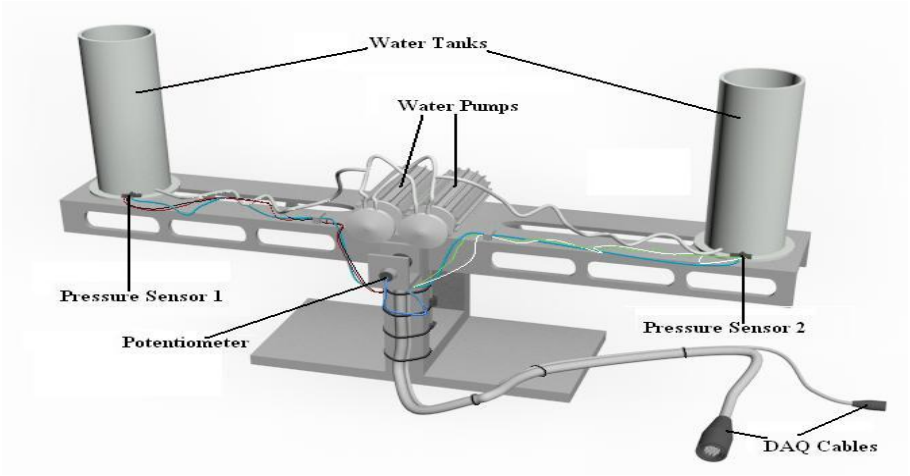

Fig. 4 3D model of balance beam system

6. Acknowledgement

Ongoing work is supported by LA-SiGMA (NSF EPS-1003897).

7. Conclusion and Ongoing Work

Hence, using the Stress, Strain and Vibration Analysis of the Cantilever Beam System and balance beam as a nonlinear control system, the students have the opportunity to learn the experiment using the different options of the remote experimentation in a crystal clear way. Presently, we are working on developing a communication infrastructure that is necessary for having the choice to run any one of many experiments (Remote Lab).

8. References

[1] S. Uran, D. Hercog and K. Jezernik, "Remote Lab Experiment RC Oscillator for Learning of Control", pp. 1-8, International Journal of Online Engineering, (2006).

[2] Sarat Paluri, Kazim Sekeroglu, Mustafa Harun Yilmaz and Amitava Jana, "Web-based Experimentation for Efficient Learning.", pp. 1-6, ASEE, Houston, Texas (2011).

[3] A.jana, P.H. Yang, D.M. Auslander, and R.N. Dave "Real Time Neuro-Fuzzy Control of a Nonlinear Dynamic System" NAFIPS'96 Proc. Of Biennial Conference the North American Fuzzy Information Processing Society Berkeley, CA. , June 20-22, 1996.

Many Big Jobs on Distributed Cyberinfrastructure

Rajib Mukherjee[1], Hideki Fujioka[2], Abhinav Thota[3], Shantenu Jha[3] and Thomas C Bishop[1]

[1]Department of Physics and Chemistry, Louisiana Tech University, Ruston, LA 71272
[2]Center for Computational Science, Tulane University, New Orleans, LA 70118
[3]Center for Computation and Technology, Louisiana State University, Baton Rouge, LA 70803

Abstract: Molecular modeling has emerged as an essential tool in our understanding of material properties at the nanoscale. This approach often requires simulating ensembles of a given system to properly sample structural and dynamical properties. Here we demonstrate how thousands of high-performance simulations can be efficiently managed in a distributed cyberinfrastructure such as LONI using a tool we developed calls ManyJobs. ManyJobs is a light-weight, portable set of python scripts that runs on shared resources such as LONI or the TeraGrid, as well as, departmental clusters and individual user resources. Using an all atom study of nucleosome positioning as model problem we demonstrate how such high-throughput high-performance simulations can be achieved.

Keywords: HPC, HTC, Distributed Computing

1. Introduction

Historical trends suggest that the capabilities of today's top 500 supercomputers become readily accessible to individual researchers in 5-7 years. Thus, IBM researchers [1] predict that Peta^2 (petaflop by petabyte) scale resources will be widely available by 2015. Peta^2 machines are ideal for conducting many medium to large scale molecular dynamics simulations, defined here as systems consisting of 100,000 to 1,000,000 atoms and total simulations times on the order of microseconds. Effectively utilizing such widely distributed computational power will enable researches to conduct the extensive sampling required for ensemble based analysis methods. However few tools currently exist for this explicit purpose. Tools employed for Folding@home and the condor workflow management tools are not designed to support the level of high performance computing achievable with these machines (I.e. tightly coupled parallel computations involving 10 to 10,000 cores) . The simulation approach presently used by many scientific groups severely limits their ability to use multiple resources in an efficient manner. The most common method used to tackle the problem of running a large number of computationally intensive jobs is to use a single high-performance computing machine and submit each job to the queue using the local PBS [4] or other queuing tools. Even if the queue dependency options are utilized, the researcher spends significant time manually intervening and must contend with potentially long queue waiting times or move data to another resource. To overcome these obstacles, we have thus developed a pilot job based tool called ManyJobs for efficient utilization of distributed resources. At the beginning of a run, ManyJobs submits job requests to the queue manager of all computing resources listed by the user. The requests are issued from a central ManyJobs database which could be hosted on a local workstation or one of the computing resources. Once a queued job starts, ManyJobs assigns it a task and submits another job request to keep the workflow active. Upon job completion the task status is registered with the ManyJobs database. The process repeats until all computational tasks in the database are finished. The ManyJobs database is capable of managing task dependencies such that

multiple simulation threads can run concurrently. ManyJobs is written in Python and utilizes 'ssh' for the communication between the ManyJobs database server and the head/computing nodes of the cluster resources. We have utilized ManyJobs to conduct 24 all atom molecular dynamic simulations of the nucleosome ranging in duration from 16 ns [2] to 100ns. Each of the 1,056 ManyJobs tasks was a 1ns simulation in NAMD of a solvated protein-DNA complex containing ~150,000 atoms. The number of simulation cores chosen for a simulation task varied, depending on the resource capabilities, and ranged from 32 to 192 cores. We are now utilizing a more robust implementation of ManyJobs, called BigJobs, to simulate 336 nucleosomes each for 20 ns to achieve a total study time of nearly 7μs (6,720 tasks)

2. Scientific Problem: The Computational Requirements

To investigate nucleosome positioning, we are conducting an all atom molecular dynamics simulation study of 336 independent fully solvated nucleosomes. Each nucleosome is represented by ~158,000 atoms and each trajectory is a 20 ns simulation. Each of the 20 ns trajectories is divided into twenty tasks where each task is a 1 ns long simulation of a given nucleosome. We thus have 6,720 tasks to perform. The total project represents 6.7 micro seconds of nucleosome dynamics and ~25TB of data. Using NAMD, this project requires approximately 4 million hours of CPU time and could be completed in approximately 2 months on a dedicated supercomputer containing only 3,000 cores. A simple scheme to automatically batch queue the tasks using 224 CPUs per task, would require ~2 years to complete the project. To achieve our project in reasonable time, we need to scale up, out and across various resources. We have modified the NAMD-G [3] scheme to effectively utilize widely distributed resources and obtained a workable solution for problems of this size. These techniques can be applied to any logically-distributed (ensemble-based) simulations.

2.1 Limitations of a Single Job Submission

Jobs in supercomputers are generally submitted manually as independent jobs, one at a time, to the queuing system either as a remote job from the user's desktop via SSH, or directly by logging into each resource and submitting the job locally. Each job has a specific task to perform which is determined when the job is submitted. When the computations in a job are dependent on another job, the user can specify dependency options like the PBS provided '-W depend= *dependency_list*' on the batch queuing system. This method is not suitable for running a large number of dependent tasks on multiple resources because the batch queues of different resources cannot communicate with each other. Thus we cannot distribute M set of N dependent task (i.e. N simulation threads) to R number of resources efficiently.

2.2 Pilot-job Based Job Submission

A key to ManyJobs is the pilot-jobs concept. A pilot-job is a job submitted to the queue without any specific task or tasks assigned to it. The computations to be executed are pulled (or pushed) from a task database after the pilot-job becomes active. Thus, pilot-job acts as a container job and it may run one or many tasks as sub-jobs. Once a container job gets the required resource allocation from the queue manager, the pilot-job can in turn distribute the resources among many sub-jobs as desired or dedicate all resources to a single sub-job. A pilot-job has a waiting

time like any other job request, but once it is active the resources can be utilized as needed. We need to keep a central job status database through which each job on different resource must communicate.

2.3 Many Jobs

We developed a prototype of an ssh-based pilot-job, called ManyJobs written in python (>=2.4). SSH is used for communication so the ManyJobs user has to set up authentication keys (Figure 1) for automatic logins. First, ManyJobs simulation manager (shown as running on the user's desktop) submits multiple jobs on multiple resources using SSH. The simulation manager manages the data-base of task descriptions. When a job becomes active in any of the resources, it pulls one or more tasks from the ManyJobs database. At present, the job pulls a single task for simulation. When the task is completed, the ManyJobs manager submits a new job onto the resource. If a task is set to depend on other possibly incomplete tasks, the dependent task won't be assigned until the first task is done. If there are no tasks ready to run but still remaining tasks that depend on other incomplete tasks, the job is finalized without pulling any tasks and the submission of new job requests is suspended. The submission of additional job requests resumes when a running task completes and more tasks become ready to run. Most shared resource centers have queuing policies that limit the number of concurrent job requests by a single user. Therefore, it may be more efficient, to bundle multiple tasks into a single pilot-job, i.e. the BigJob, sub-job concept.

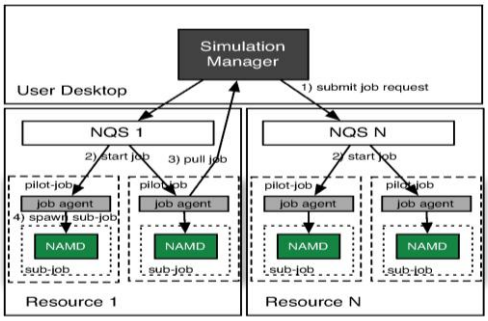

Fig 1 ManyJobs Architecture

3. Experiments and Results

For the computational experiment displayed below, we have distributed a set of 30 nucleosome simulations each of 10ns duration, i.e. 300 tasks, across five LONI sites and the TeraGrid resource, Lonestar. For data storage and handling, we have used PetaShare as a central data storage resource. ManyJobs is used to manage the 30 threads. On each LONI resource we request four separate jobs, each of 64 cores, at any given moment. On Lonestar we request seven separate jobs, each of 192 cores at any given moment. Various attributes of a resource determine the optimal choice of limit cores and job request. Figure 2 demonstrates how ManyJobs distributed the 300 tasks over the six computing resources after the experiment was initiated at Time=0 (hr). Each colored-rectangle represents an actual task. The vertical and the horizontal axes indicate which resource ran a given task and when the task ran, respectively. The length of each rectangle thus represents the duration of the task in real time. The Lonestar rectangles are shorter because more cores were requested. We achieved almost uninterrupted run times on both Eric and Oliver. These results underscore the long delays that can be encountered, because of wait times or machine failures, if a user simply chooses a single resource and commits all simulations to that resource. While the black arrow highlights the time savings that can be obtained by the dark red thread as it moves from Louie to

Lonestar to Eric and finally to Painter. By moving the simulations to where ever the resources became available, this thread was able to finish with nearly zero downtime.

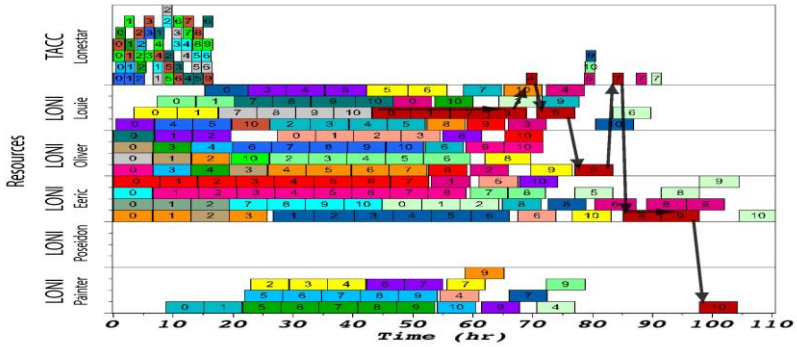

Fig 2 Tasks distributed over six supercomputers by ManyJobs. The rectangles with same color are tasks in the same thread, i.e. the simulations of one color are time dependent. The number in each rectangle represents the sequence number of the tasks within a thread.

4. Conclusion

High throughput simulations of large number of tasks in multiple supercomputers using regular batch submission of single jobs require constant manual intervention and book keeping. The complexity of the process can be significantly reduced and efficiency can be increased by the use of pilot-job implementations that run across multiple machines. We have successfully implemented ManyJobs in LONI environment, on select TeraGrid sites. As our results show the use of ManyJobs in distributed cyberinfrastructure provides a promising environment to support the execution of thousands of high-performance simulations. The various advantages include a reduced time-to-solution (higher throughput) compared to when a single resource is used and less user intervention in the job management and distribution process. ManyJobs can be successfully extended to any locally maintained clusters on the network and has now been adapted to work with gsi-ssh as well as ssh for data communications.

5. Acknowledgments

Bishop, Mukherjee and Jha are funded by the NSF EPSCoR LASiGMA project under award #EPS-1003897 for the computational effort. Hideki Fujioka funded by LONI institute support. Scientific part of the project is supported by NIH(R01GM076356) to T. C. Bishop.

6. References

[1] K. Jordan, keynote speaker at 8th Annual Rocky Mount Conf. of Intl. Society Comp. Biology \url{http://www.iscb.org/rocky10-program/agenda

[2] R. Mukherjee, T C Bishop, "Nucleosomal DNA Kinked or Not Kinked: Self Healing Material," Submitted

[3]M. Gower, J. Cohen, J. Phillips, R. Kufrin, and K. Schulten. Managing biomolecular simulations in a grid environment with namd-g. In Proceedings of the 2006 TeraGrid Conference, 2006., 2006.

[4]DEC 19 1997. R. Henderson and D. Tweten. Portable Batch System: External Reference Specification. Technical report, NASA Ames Research Center, 1996.

Molecular Dynamics Simulation of Self-Assembly of Span80 into Micelles and Their Interaction with Vitamin E

Jieqiong Lin[1], Kai Xia[1], Brian R. Novak[1], Cristina E. Sabliov[2] and Dorel Moldovan[1]

[1]Department of Mechanical Engineering, Louisiana State University, Baton Rouge, LA 70803
[2]Biological and Agricultural Engineering Department, Louisiana State University Agricultural Center, Baton Rouge, LA 70803

Abstract: Using realistic all-atom inter-atomic interaction models we present large-scale molecular dynamics (MD) simulation of Span80 surfactant self-assembly in water at concentrations above the critical micelle concentration. We investigate the kinetics of aggregation by starting from random solutions of Span80 molecules and letting the systems evolve along their natural pathways during the aggregation. At intermediate surfactant concentration of 0.25 M, in a simulation system containing 125 Span80 molecules, the system evolves into a single spherical structure (possible a micelle) in about 20 ns. The self-assembly of the surfactant molecules takes place in three stages: the fast first stage (~1ns) consists in aggregation of the surfactant molecules in small clusters; the second stage is a ripening stage in which the larger clusters grow at the expense of the smaller ones and the third stage (the slow stage) involves diffusion and coalescence of larger micelles. We also report additional MD simulation results delineating with atomistic details the mechanism of passive absorption and entrapping of alpha-tocopherol (vitamin E) into Span80 micelles.

Keywords: Molecular dynamics, Span80, Alpha-tocopherol (vitamin E)

1. Introduction

Surfactant molecules are very important in a wide variety of processes such as biological, as in molecular transport across cell membranes, commercial as in detergents and stain removers, and industrial as in emulsion polymerization. Their unique properties come from their amphiphilic nature, i.e., each molecule contains both a hydrophilic and a hydrophobic part. When dissolved in water, above certain concentration, termed critical micelle concentration (cmc), surfactants self-assemble into mesoscopic aggregates such as micelles, vesicles or bilayers. Span 80, known also as sorbitan monooleate, is a relatively cheep, molecular heterogeneous, nonionic surfactant that is widely used as food emulsifier, in oral pharmaceuticals, or in cosmetic industry. Span 80 can also be used as oil-soluble emulsifier and in synthesis of vehicles for drug delivery. In this study, we performed molecular dynamics studies to investigate the mechanism of spontaneous aggregation of Span80 molecules into larger structures (micelles) and how the alpha-tocopherol (vitamin E) molecule was absorbed and entrapped in a pre-formed Span80 micelle.

2. Simulation methodology

Molecular dynamics simulations were performed with GROMACS 4.0 package with periodic boundary conditions applied in all directions. The force field parameters for bonded and non-bonded interactions for Span80 and alpha-tocopherol were generated by PRODRG2.5 server [1]. The water was modeled as simple point charge (SPC) [2]. All simulations were carried out at a constant pressure of 1.0 atm using a Beredsen barostat [3]and semi-isotropic coupling. The temperature was held constant at 300K. All bond lengths were constrained by using the LINCS algorithm[3] or the SETTLE[4] algorithm for the waters. For short range non-bonded interactions, GROMACS uses a twin range cutoff. The cutoff of 1.0 nm was used for both Lennard-Jones and electrostatic interactions (updated every 10 steps). The long-range electrostatic interactions were treated using the particle mesh Ewald (PME) algorithm[5, 6] We used a time step of 2.0 fs.

Two simulation systems were investigated; one contains 125 Span80 molecules and the other one 512. In addition to the amphiphiles the two simulation system contain 24,000 and 109,000 water molecules respectively. In both systems the initial configuration was generated by placing the Span80 molecules randomly throughout the simulation box. We also report additional MD simulation results delineating with atomistic details the mechanism of passive absorption and entrapping of alpha-tocopherol (vitamin E) into Span80 micelles.

3. Results

The three snapshots in Figure1 illustrate the spontaneous aggregation process of 125 Span80 molecules into a single spherical micelle during the simulation. For clarity the water molecules are not shown. Red spheres are used to represent the hydrophilic head groups and yellow lines represent the hydrophobic tail groups. Figure 1(a) shows the initial structure with Span80 molecules uniformly distributed in water; figure 1(b) shows an intermediate stage during aggregation in which several small aggregates are present. Finally these small aggregates coalesce and form a single spherical micelle (figure 1(c)).

Figure 2 depicts the self-assembly process in a larger system consisting of 512 Span 80 molecules. The Span80 molecules aggregate in 7 micelles of similar sizes in about 9 ns.

Figure 3 depicts with atomistic details the mechanism of passive absorption and entrapping of an alpha-tocopherol (vitamin E) molecule into a preformed Span80 micelle. In the initial structure the vitamin E molecule was placed at a distance of about 0.8 nm away from the surface of the micelle. Our simulation results indicate that the incorporation of vitamin E into the pre-assembled Span80 spherical micelle occurs spontaneously. The entrapping mechanism involves a two-step process where first the hydrophobic tail of the vitamin E molecule is incorporated into the surface of the micelle followed by reorientation and penetration of the tail into the tails region of the micelle.

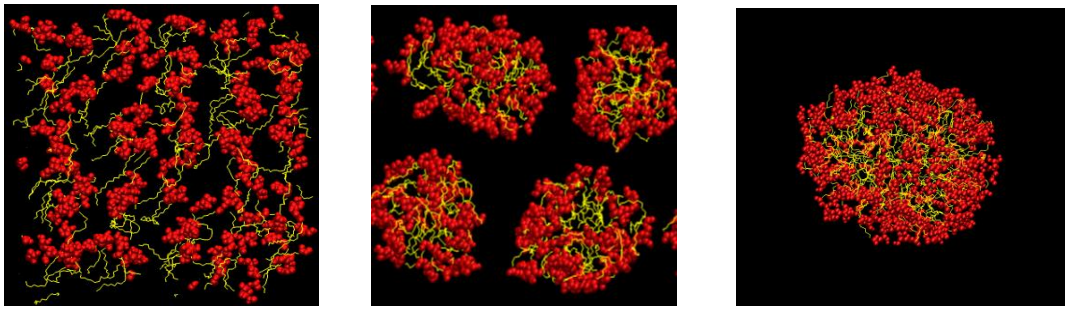

(a) 20ps (b) 6ns (c) 10ns

Figure1 Three snapshots of the125 Span 80 system at the simulation time 20ps, 6 and 10ns respectively.

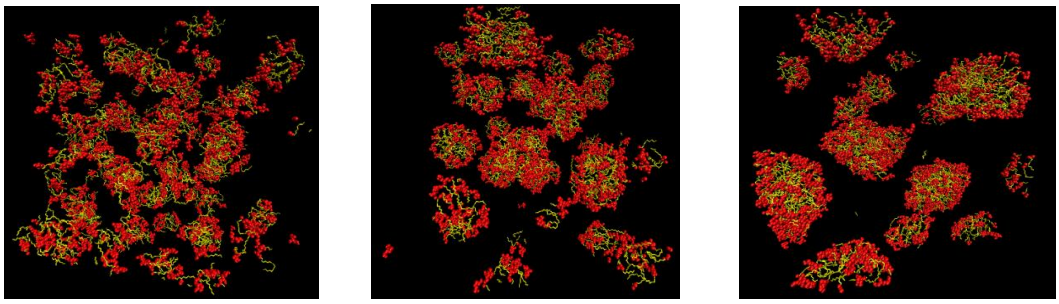

(a) 200ps (b) 5ns (c) 9ns

Figure 2 Three snapshots of the 512 span80 system at the simulation time 200ps, 5ns and 9ns respectively.

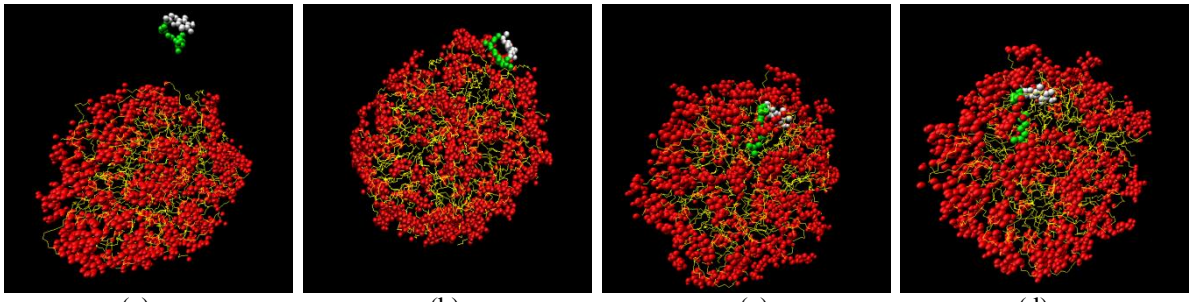

(a) (b) (c) (d)

Figure 3 Four snapshots delineating the passive absorption and entrapping of an alpha-tocopherol (vitamin E) molecule into a pre-assembled Span80 spherical micelle consisting of 125 surfactant molecules. Initially the vitamin E molecule was placed at a distance of about 0.8 nm away from the surface of the micelle. In the representation of the vitamin E the silver spheres are used to represent the hydrophilic head groups and green spheres represent the hydrophobic tail groups

4. Conclusion

Using all-atom large-scale MD simulations we have shown that the spontaneous aggregation of Span80 surfactants into spherical micelles is a very fast process and occurs within a few tens of nanoseconds. The MD simulations indicate that, when starting from an initial random distribution of the surfactant molecules, the aggregation process occurs in three stages: first the surfactant molecules aggregate in small clusters followed by a cluster ripening stage and ending with a slow stage involving diffusion and coalescence of small micelles.
Our study also shows that the incorporation of vitamin E into a pre-assembled Span80 spherical micelle can occur in a spontaneous fashion. The mechanism involves a two-step process where first the hydrophobic tail of the molecule is incorporated into the surface of the micelle followed by reorientation and penetration of the tail into the tails region of the micelle.

5. Acknowledgments

The current work is supported by the NSF-EPSCoR, Grant # EPS-1003897 (LA-SiGMA). Computational resources were provided by LONI and HPC @ LSU.

6. References

[1] A. W. Schuettelkopf and D. M. F van Aalten, *Acta Crystallograpgica*, D60, 1355 (2004).
[2] H.J.C. Berendsen, J.P.M. Postma, W.F. Gunsteren, J. Hermans, *Intermolecular Forces*, Pulman, The Netherlands, pp. 331-342 (1981).
[3] Hess, B., et al., LINCS: A linear constraint solver for molecular simulations. Journal of Computational Chemistry, 18(12): p. 1463-1472 (1997).
[4] Miyamoto, S. and P.A. Kollman, SETTLE - An Analytical Version of the SHAKE and RATTLE Algorithm for Rigid Water Models. Journal of Computational Chemistry, 13(8): p. 952-962 (1992).
[5] Darden, T., D. York, and L. Pedersen, Particle Mesh Ewald - An N-Log(N) Method for Ewald Sums in Large Systems. Journal of Chemical Physics, 98(12): p. 10089-10092 (1993).
[6] Essmann, U., et al., A Smooth Particle Mesh Ewald Method. Journal of Chemical Physics, 103(19): p. 8577-8593 (1995).

Molecular Magnets: High Spin Investigation of Iron Oxide Clusters

J.M. Leveritt III[1], A. Kurnosov[1], J.P. Perdew[2], V. Kolesnichenko[3], G. Goloverda[3], A.L. Burin[1]

[1]Department of Chemistry, Tulane University
[2]Department of Physics, Tulane University
[2]Department of Chemistry, Xavier University of Louisiana

Abstract: Elementary iron oxide clusters derived from spinel-type structures (magnetites, ferrites, etc.) are promising candidates to show small molecular magnet behavior similarly to their crystalline counterparts. In this preliminary work we investigate the ground state of two simple clusters $Fe_8H_{24}O_{24}$ and $Fe_8H_{26}O_{24}$ with two different Fe oxidation states ($8Fe^{3+}$ and $6Fe^{3+}2Fe^{2+}$, respectively) reproducing the elementary cell of magnetite with dangling bonds terminated by hydrogen atoms and water molecules. A QM/MM approach is taken using the quantum mechanical theory mPWPW91 to treat the iron atoms and the traditional UFF force field to treat the remainder of the atoms. The total spin, S, of a ground state is predicted to be S=4 in $Fe_8H_{24}O_{24}$ and S=10 in $Fe_8H_{26}O_{24}$. We also tested our method on a traditional molecular magnet Fe8 and show that it predicts the total ground state spin with reasonable accuracy.

Keywords: small molecular magnets, iron clusters, spinel-type, Fe-8, QM/MM.

1. Introduction

Small molecular magnets have many interesting applications in all fields of science, and a few examples include its potential use in quantum computation[1, 2], information storage[3], and potential permanent room temperature magnets[3]. Many small molecular magnets have been synthesized including Fe-8[4], Manganese-12[5], cobalt (II) structures[6], and V-15 structures[7]. Two key features of all of these small molecular magnets is the occurrence of a high spin ground state[8-11], and a large magnetic anisotropy barrier.[12, 13]

In this paper we investigate the simplest iron oxide clusters having spinel structure as alternative promising molecules[14] which can form a new family of molecular magnets. The magnetism is expected there similarly to magnetite having an identical structure.[15] We investigate the simplest cluster containing eight Fe atoms and reproducing the elementary cell of magnetite (see Fig. 1). The dangling bonds to other cells are terminated by hydrogen atoms. The cluster structure is similar to the other popular molecular magnet Fe-8. An important distinction between our proposed spinel-type iron cluster and Fe-8 is the relative size of the two molecules. Oxide iron clusters are almost two times smaller and therefore can be more suitable in various nano-applications as explored by Ref. [16].

In our calculations we used QM/MM approaches[16-18] to perform geometry optimizations and energies of various spin states[18] are calculated with the pure DFT functional mPWPW91 all available within the Gaussian 09

package.[19] QM/MM approaches have been used throughout inorganic chemistry for thermodynamic calculations in catalysis processes, electronic structure calculations, and they reproduce crystal structures of various complexes with a reasonable accuracy[16-18]. Du et al recently did some structural computations involving dimers containing various transition metal centers, and through this "finger printing" approach is shown that using the mPWPW91 theory for iron containing clusters can accurately calculate bond lengths determined via X-Ray crystallography[18]. These calculations justify our approach from a structural point of view, and it is the aim of this work to predict the molecular spin in the ground state corresponding to the global energy minimum. To test the relevance of used methods we also applied the theory to Fe-8 molecular magnets where the spin in the ground state, S=10, is known experimentally.

2. Theory

All structures were created using elementary cell of magnetite and then optimized with the Gaussian 09 package[19]. The structure of the optimized spinel-type iron cluster $Fe_8H_{24}O_{24}$ is shown in Figure 1. The equatorial irons are terminated with the addition of water molecules. Similar geometries have been calculated for various high spin states, and another set of optimizations have been performed after changing the oxidation states of two iron atoms ($Fe^{3+} \rightarrow Fe^{2+}$) via the addition of two hydrogen atoms ($Fe_8H_{26}O_{24}$). Singlet states were not calculated due to difficulty with their convergence (restricted vs. unrestricted wavefunctions).

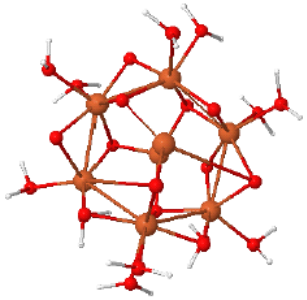

Figure 1 *Optimized structure of an iron cluster of the spinel-type moiety*

QM/MM methods have been used to perform basic geometry optimizations for various spin states ranging from S=1 to S=12. The inspiration using these methods comes from a recent review of Bo and Maseras[16] (see also references therein) where these methods have been successfully applied to various inorganic systems. The quantum mechanical method used is the pure DFT functional mPWPW91 capable to accurately calculate geometries of systems with multiple metal centers[17]. The molecular mechanics calculations were performed using the UFF force field, which is standard in QM/MM computations of inorganic systems.[16]

3. Results and Discussion

The dependence of ground state molecular energy on the total spin is shown in Fig. 2. For the cluster $Fe_8H_{24}O_{24}$

where all Fe atoms have oxidation state 3+ the energy minimum takes place at large spin, S=4. For the cluster $Fe_8H_{26}O_{24}$ ($6Fe^{3+}$, $2Fe^{2+}$) the energy minimum has been found at S=10 which is, indeed, high spin state. Computations for Fe-8 were achieved in the same manner indicating a high spin ground state (S=9), while the actual value is S=10, which validates qualitatively our approach.

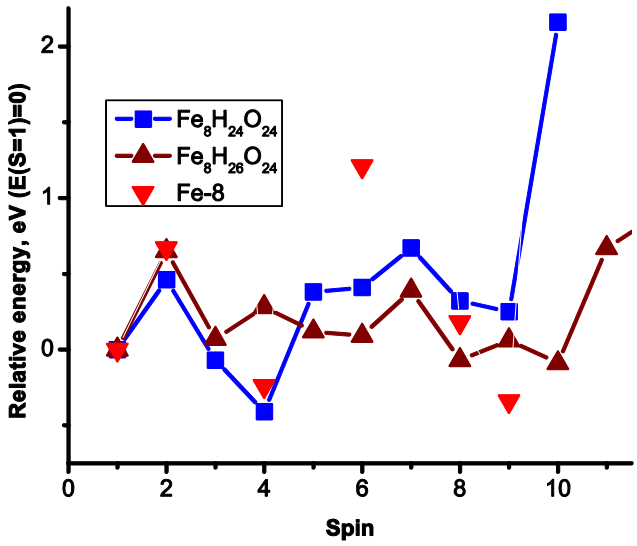

Figure 2 *The ground state of different clusters vs. the total spin. Ground states are realized at S=4 and S=10 for $Fe_8H_{24}O_{24}$ and $Fe_8H_{26}O_{24}$, respectively. The large energy for some spin states is possibly due to poor convergency*

4. Conclusion and Future Work

Iron oxide clusters, $Fe_8H_{24}O_{24}$ and $Fe_8H_{26}O_{24}$, of the spinel-type structure were studied using a QM/MM approach combined with mPWPW91 theory. It is shown that depending on the oxidation state of the iron atoms the ground state has the total spin S=4 ($8Fe^{3+}$), and S=10 ($6Fe^{3+}$, $2Fe^{2+}$). More oxidation states will be explored with the further addition of hydrogen atoms to understand this effect. Thus we predicted that $Fe_8H_{26}O_{24}$ can serve as a high spin molecular magnet. The ground state of Fe-8 was explored, and it is shown that our method predicts a ground state of S=9 slightly different from the experimental value S=10 possibly because relativistic effects were not taken into effect. Future work includes exploring anisotropy effects through the use of the ORCA package.[12] Experimental verification of our predictions by our collaborators in Xavier University is in progress. .

5. Acknowledgments

The work is supported by the NSF EPSCoR LA-SiGMA project under award #EPS-1003897. We thank Igor Tupitzyn for giving us data for Fe-8 Geometry and Rajesh Shrestha for useful discussions.

6. References

[1] D Gatteschi, R Sessoli. Quantum Tunneling of Magnetization and Related Phenomena in Molecular Materials.AngewandteChemie-International Ed. 43, 3, 2003.

[2] JA Jones. Fast searches with nuclear magnetic resonance computers. Science, 208, 5361, 229, 1998.

[3] AV Postnikov, J Kortus, MR Pederson. Density functional studies of molecular magnets.Physica Status Solidi (b) – Basic Solid State Physics, 243, 11, 2006

[4] K Wieghardt, K Phol, I Jibril, G Huttner. Hydrolysis products of the monomeric amine complex (C6H15N3)FeCl3 – the structure of the octameric iron (III) cation of [[(C6H15N3)6Fe8(u3-O)12]Br7(H2O)]Br8H2O. AngewandteChemie-International Ed. Engl, 23, 77

[5] T Lis. Preparation, structure, and magnetic properties of a dodecanuclear mixed-valence manganese carboxylate.ActaCrystallogr. Soc. B 36, 2042, 1980

[6] M Murrie. Cobalt(II) single-molecule magnets. Chemical Society Reviews, 39, 6, 1986-1995, 2010

[7] A Muller, J Doring. A novel heterocluster with d3-symmetry containing 21 core atoms – [As6(III)V15(IV)O42(H2O)]6-. Angewandte.Chemie-International. Ed. Engl. 27, 1721, 1988

[8] AM Ayuk, IJ Hewitt, V. Mereacre, R. Clerac, W. Wernsdorfer, CE Anson, AK Powell. A ferromagnetically coupled Mn-19 aggregate with a record S=83/2 ground spin state. AngewandteChemie-International Edition, 45, 30, 4926-4929, 2006

[9] A Caneschi, D Gatteschi, R Sessoli, AL Barra, LC Brunel, M Guillot. Alternating-current susceptibility, high-field magnetization, and milllimeter band EPR evidence for a ground S = 10 state in [MN12O12(CH3COO)16(H2O)4].2CH3COOH.4H2O. Journal of the American Chemical Society, 113, 15, 5873-5874, 1991.

[10] E Ruiz, J Cirera, J cano, S Alvarez, C Loose, J Kortus. Can large magnetic anisotropy and high spin really coexist?. Chemical Communications, 1, 52-54, 2008

[11] SMJ Aubin, ZM Sun, L Pardi, J Krzystek, K Folting, LC Brunel, AL Rheingold, G Christou, DN Hendrickson. Reduced anionic Mn-12 molecules with half-integer ground states as single-molecule magnets. Inorganic Chemistry, 38, 23, 5329-5340, 1999

[12] F. Neese, DA Pantazis. What is not required to make a single molecule magnet. Faraday Discussions, 148, 229-238, 2011

[13] CJ Milios, A Vinslava, W Wernsdorfer, S Moggach, S Parsons, SP Perlepes, G Christou, EK Brechin. A record anisotropy barrier for a single-molecule magnet. Journal of the American Chemical Society, 129, 10, 2754+, 2007

[14] G Aromi, EK Brechin. Synthesis of 3d metallic single-molecule magnets.Single-Molecule Magnets and Related Phenomena. Structure and Bonding, 112, 1-67, 2006

[15] Z Zhang, S Satpahty. Electron states, magnetism, and the Verwey transition in magnetite, Phys. Rev. B 44, 13319-13331 (1991).

[16] D Gatteschi, ACaneschi, L Pardi, R Sessoli. Large Clusters of Metal-Ions – The Transition From Molecular to Bulk Magnets. Science, 265, 5175, 1054-1058

[17] C Bo, F Maseras. QM/MM methods in inorganic chemistry. Dalton Transactions, 2911-2919, 2008

[18] JG Du, XY Sun, HY Wang. The confirmation of accurate combination of functional and basis set for transition-metal dimers: Fe-2, Co-2, Ni-2, Ru-2, Rh-2, Pd-2, Os-2, Ir-2, and Pt-2 International Journal of Quantum Chemistry, 108, 9, 1505-1517

[19] Frisch, M. J. et al. GAUSSIAN 09 Revision A.1, Gaussian, Inc. Wallingford CT 2009.

Optimization of Linear and Branched Alkane Interactions with Water to Simulate Hydrophobic Hydration

Henry S. Ashbaugh and Lixin Liu

Department of Chemical and Biomolecular Engineering, Tulane University, New Orelans, LA 70118

Abstract: Previous studies of simple gas hydration have demonstrated that the accuracy of molecular simulations at capturing the thermodynamic signatures of hydrophobic hydration is linked both to the fidelity of the water model at replicating the experimental liquid density at ambient pressure and an accounting of polarization interactions between the solute and water. We extend those studies to examine alkane hydration using the Transferable Potentials for Phase Equilibria-United Atom model for linear and branched alkanes, developed to reproduce alkane phase behavior, and the TIP4P/2005 model for water, which provides one of the best descriptions of liquid water of the available fixed-point charge models. Alkane site/water oxygen Lennard-Jones cross interactions were optimized to reproduce experimental alkane hydration free energies over a range of temperatures. The optimized model reproduces the hydration free energies of the fitted alkanes with a root mean square difference between simulation and experiment of 0.06 kcal/mol over a wide temperature range, compared to 0.44 kcal/mol for the parent model. The optimized model accurately reproduces the temperature dependence of hydrophobic hydration, as characterized by the hydration enthalpies, entropies, and heat capacities.

Keywords: hydrophobic hydration, molecular simulation, interaction potential

1. Introduction

The poor solubility of non-polar oils in water is characterized not only by unfavorable hydration free energies but significant temperature dependencies to the underlying thermodynamic contributions to the free energy.[1,2] More specifically, at ambient temperature the dissolution of hydrophobic species from the gas phase is favored by negative enthalpic contributions to the free energy, but these are overwhelmed by unfavorable negative entropic contributions. At higher temperatures hydration is entropically favored but disfavored by a dominant positive enthalpy. The changing roles of enthalpy and entropy in opposing non-polar solute hydration are indicative of a large, positive heat capacity increment. Collectively these thermodynamic properties have been identified as signatures of hydrophobic hydration. The importance of water-mediated interactions between non-polar moieties in driving self-assembly processes, like surfactant micellization[2] and protein folding,[3,4] has motivated simulation studies to probe the molecular rationale underlying the meager solubility of hydrophobic species and manifestations of its characteristic temperature dependence, like solubility minima.

Simulation calculations of the dissolution of the normal alkanes at ambient conditions tend to under predict their aqueous solubility.[5,6] It may be anticipated that, similar to simple non-polar gases, polarization effects between water and the hydrocarbon are unaccounted for in these simulations. To address this shortcoming, we reparameterize a standard simulation potential that permits modeling of the linear and branched alkanes, the

Transferable Potentials for Phase Equilibria United-Atom model (TraPPE-UA),[7,8] to reproduce their experimental aqueous solubility at atmospheric pressure in TIP4P/2005 water.[9] These alkane and water models were chosen due to their accuracy in reproducing the experimental pure component liquid/vapor phase diagrams. Solubilities were calculated over a broad temperature range permitting a simultaneous analysis of the enthalpic, entropic, and heat capacity contributions to the hydration free energies that are characteristic of hydrophobic hydration.

2. Simulation Techniques

Alkane hydration simulations were performed using the GROMACS 4 molecular dynamics simulation package.[10] Simulations were conducted in the isothermal isobaric ensemble for a single alkane in a bath of 400 water molecules. Simulations were conducted over a series of temperatures from 270 K to 370 K in 10 K increments at atmospheric pressure. The temperature and pressure were maintained using the Nose-Hoover thermostat[11,12] and Parrinello-Rahman barostat,[13] respectively. A 2 fs time step was used to integrate the equations of motion. Lennard-Jones interactions were evaluated out to 9 Å, and standard long-range corrections were applied to the energy and pressure. Particle Mesh Ewald summation[14,15] was used to evaluate electrostatic interactions. Water was modeled using the TIP4P/2005 potential,[9] which provides one of the most accurate description water's equation-of-state over the liquid regime at atmospheric pressure of the available classical fixed charge models. The TraPPE-UA potential,[7,8] which is optimized to reproduce pure alkane phase diagrams, was used as the basis to simulate the linear and branched alkanes. The alkanes simulated were methane, ethane, propane, butane, isobutane, and neopentane.

Table 1. Cross alkane site/water oxygen Lennard-Jones interaction parameters for the TraPPE-UA and HH-Alkane models.

	σ_{iw} (Å)	ε_{iw}/R (K)
TraPPE-UA		
CH_4	3.444	117.4
CH_3	3.452	95.57
CH_2	3.552	65.48
CH	3.919	30.53
C	4.779	6.826
HH-Alkane		
CH_4	3.436	123.0
CH_3	3.448	98.92
CH_2	3.547	67.99
CH	3.895	33.71
C	4.614	11.18

To begin, simulations were conducted using the TraPPE-UA interaction model to calculate alkane hydration free energies in water over a wide temperature range using the thermodynamic integration method.[16,17] The free energies were subsequently compared with experimental hydration free energies. The alkane site (i) – water oxygen (w) cross interaction Lennard-Jones diameters (σ_{iw}) and well depths (ε_{iw}) were optimized to minimize the root mean square difference between simulation and experiment. The alkane intramolecular interactions for the optimized model were assumed to be equal to that of the parent TraPPE-UA model. The cross alkane site – water oxygen Lennard-Jones parameters for the TraPPE-UA model listed in Table 1 were obtained using standard Lorenz Berthelot combining rules.

3. Results

Alkane hydration free energies at 300 K for methane, ethane, propane, butane, isobutane, and neopentane calculated from simulations using the TraPPE-UA model are listed in Table 2. These free energies were further decomposed into enthalpic, entropic, and heat capacity contributions by fitting the simulation free energies the function $\mu_s^{ex} = a + bT + cT\ln T$, which assumes a temperature independent hydration heat capacity, and taking the

appropriate temperature (T) derivatives. While alkane hydration thermodynamic properties are in reasonable agreement with experiment[18,19] (Table 2), the TraPPE-UA model generally over predicts the hydration free energies of all the alkanes. This over prediction is observed over the entire simulated temperature range for the all the alkanes examined (results not shown). The root mean square free energy difference between the TraPPE-UA model simulations and experiment averaged over all alkanes and temperatures is 0.44 kcal/mol, comparable to the ambient thermal energy, kT.

Table 2. Alkane hydration thermodynamic properties at 300 K and atmospheric pressure from experiment and simulation for the TraPPE-UA and HH-Alkane cross interaction models in TIP4P/2005 water.

	μ_s^{ex} kcal/mol	h_s^{ex} kcal/mol	s_s^{ex} cal/(mol K)	c_s^{ex} cal/(mol K)
experiment[18,19]				
methane	2.03	-2.66	-15.6	49.5
ethane	1.87	-4.04	-19.7	71.7
propane	2.00	-4.66	-22.2	88.1
butane	2.13	-5.49	-25.4	89.1
isobutane	2.29	-5.08	-24.5	88.4
neopentane	2.56	-5.88	-28.1	123
TraPPE-UA				
methane	2.23	-2.19	-14.7	44.5
ethane	2.07	-3.67	-19.1	56.8
propane	2.31	-4.71	-23.4	75.5
butane	2.47	-5.72	-27.3	79.3
isobutane	2.73	-5.20	-26.5	88.6
neopentane	3.32	-4.75	-26.9	85.4
HH-Alkane				
methane	2.03	-2.28	-14.4	43.0
ethane	1.86	-4.07	-19.8	61.7
propane	2.01	-5.23	-24.1	77.2
butane	2.14	-6.29	-28.1	95.8
isobutane	2.28	-5.91	-27.3	88.3
neopentane	2.53	-6.38	-29.7	108

Starting from the TraPPE-UA model, we optimized the alkane-water interaction parameters to reproduce the experimental hydration free energies to create the Hydrophobic Hydration Alkane model (HH-Alkane). The alkane site-water oxygen cross interaction parameters for the HH-Alkane model are reported in Table 1. The hydration thermodynamic properties of the HH-Alkane model at 300 K evaluated from simulation are reported in Table 2. Generally the agreement with experiment[18,19] is excellent, particularly for the hydration free energies, which quantitative reproduces experiment. Compared the to the TraPPE-UA model, the HH-Alkane model provides a significantly improved description of alkane hydration over the entire temperature range (results not shown). The root mean square free energy difference between HH-Alkane model simulations and experiment averaged over all alkanes and temperatures is 0.06 kcal/mol, nearly ten times better than the parent model.

Generally the improved agreement between simulation and experiment achieved for the HH-Alkane model was obtained by increasing the Lennard-Jones well depth of all the alkane sites by $D\varepsilon_{iw}/k \approx 3$ to 6 K. This suggests the discrepancy between the free energies obtained using the TraPPE-UA model and experiment arises largely from polarization interactions typically not included in classical molecular simulation models.

4. Conclusion

Beginning with the TraPPE-UA model for linear and branched alkanes as a foundation, we developed the HH-Alkane model by optimizing solute site/water oxygen cross interactions to reproduce the hydration free

energies of methane, ethane, propane, butane, isobutane and neopentane over a range of temperatures. Optimizing Lennard-Jones interactions results in a lowering of the Lennard-Jones well-depth by $D\varepsilon_{iw}/k \approx 3$ to 6 K. Concurring with previous studies of noble gases and methane in water, we ascribe the increase in the cross interaction well-depth to polarization of the alkane by water. This effective polarization is largely absent in the TraPPE-UA model since it was originally developed to reproduce the phase behavior of the non-polar alkanes. We have optimized HH-Alkane interactions for the all the CH_n sites ($n = 0$ to 4) permitting extension of the model to any linear or branched alkane in water.

5. Acknowledgments

The current work is funded by the NSF EPSCoR LA-SiGMA project under award #EPS-1003897.

6. References

[1] H. S. Frank and M. E. Evans, J. Chem. Phys. 13, 507 (1945).
[2] C. Tanford, *The Hydrophobic Effect: Formation of Micelles and Biological Membranes*. (John Wiley and Sons, New York, NY, 1973).
[3] W. Kauzmann, Adv. Protein Chem. 14, 1 (1959).
[4] K. A. Dill, Biochemistry 29, 7133 (1990).
[5] N. M. Garrido, A. J. Queimada, M. Jorge, E. A. Macedo, and I. J. Economou, J. Chem. Theory Comp. 5, 2436 (2009).
[6] E. Gallachio, M. M. Kubo, and R. M. Levy, J. Phys. Chem. B 104, 6271 (2000).
[7] M. G. Martin and J. I. Siepmann, J. Phys. Chem. B 102, 2569 (1998).
[8] M. G. Martin and J. I. Siepmann, J. Phys. Chem. B 103, 4508 (1999).
[9] J. L. F. Abascal and C. Vega, J. Chem. Phys. 123, 234505 (20 05).
[10] B. Hess, C. Kutzner, D. van der Spoel, and E. Lindahl, J. Chem. Theory Comp. 4, 435 (2008).
[11] S. Nos´e, Mol. Phys. 52, 255 (1984).
[12] W. G. Hoover, Phys. Rev. A 31, 1695 (1985).
[13] M. Parrinello and A. Rahman, J. Appl. Phys. 52, 7182 (1981).
[14] T. Darden, D. York, and L. Pedersen, J. Chem. Phys. 98, 10089 (1993).
[15] U. Essmann, P. N. Perera, M. L. Berkowitz, T. Darden, H. Lee, and L. G. Pedersen, J. Chem. Phys. 103, 8577 (1995).
[16] D. Chandler, *Introduction to Modern Statistical Mechanics*. (Oxford University Press, New York, NY, 1987).
[17] D. van der Spoel, E. Lindahl, B. Hess, A. R. van Buuren, E. Apol, P. J. Meulenhoff, D. P. Tielmann, A. L. T. M. Sijber, K. A. Dennstra, R. van Drunen, and H. J. C. Berendsen, *Gromacs User Manual version 4.5*. (www.gromacs.org, 2010)
[18] E. Wilhelm, R. Battino, and R. J. Wilcock, Chem. Rev. 77, 219 (1977).
[19] N. V. Plyasunova, A. V. Plyasunov, and E. L. Shock, Int. J. Thermophys. 25, 351 (2004). webdocs.asu.edu.

Preparation and Characterization of Amphiphilic Homopolymers

Yi Wang, Scott M. Grayson

Department of Chemistry, Tulane University, New Orleans, LA 70118

Abstract: A neutral amphiphilic monomer bearing both hydrophilic and hydrophobic side chain was designed and synthesized, and the monomer was polymerized via atom transfer radical polymerization (ATRP). The resultant amphiphilic homopolymers were characterized by NMR, GPC and MALDI and the molecular weight and polydispersity of the polymers were determined. UV, fluorescence and dynamic light scattering (DLS) studies showed that the amphiphilic polymers could form micelles in non-polar organic solvent that can encapsulate small polar molecules. The critical micelle concentration (~0.05mg/mL) determined by fluorescence was much lower than normal amphiphilic block copolymer. The unique aggregation behavior of these of amphiphilic homopolymers makes them promising candidates for further usage in drug delivery and other applications.

Keywords: Amphiphilic, homopolymer, dye encapsulation, drug delivery

1. Introduction

Amphiphilic polymers exhibit a unique ability to self-assemble, owing the contrasting physical properties of their polar and non-polar regions. This propensity to self-assemble makes them appealing materials for a variety of applications, including like drug delivery, sensing and catalyst as well as a variety of other "smart" materials applications [1]. A amphiphilic homopolymer which has both hydrophobic and hydrophilic region on each monomer unit can exhibit better self-assemble properties and a lower critical micelle concentration (CMC) [2], making them promising candidates for drug delivery. Because of the limited amount of research that has been devoted to this interesting class of materials, this research project is devoted to investigating the effects of polymer architecture on the properties of amphiphilic homopolymers.

Atom transfer radical polymerization (ATRP) is a controlled radical polymerization technique that enables exception control over molecular weight of the resulting polymer, and yields well-defined polymers with narrow polydispersity [3]. In addition, the "livingness" of the ATRP offers near quantitative end-group functionality that offers the possibility of further modification and assembly of the amphiphilic homopolymers.

2 Experiment section

2.1 Synthesis and characterization of the monomer

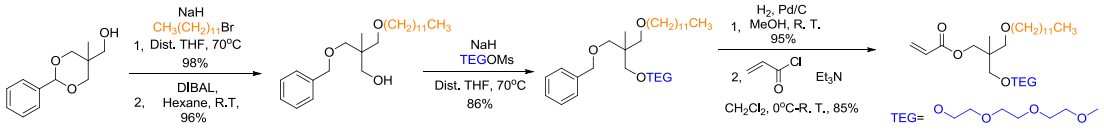

Scheme 1. Synthesis of amphiphilic monomer

The monomer was synthesized for 7 steps [4] with a total yield of 59% and characterized by ^{1}H and ^{13}C NMR

2.2 Synthesis and characterization of the polymers

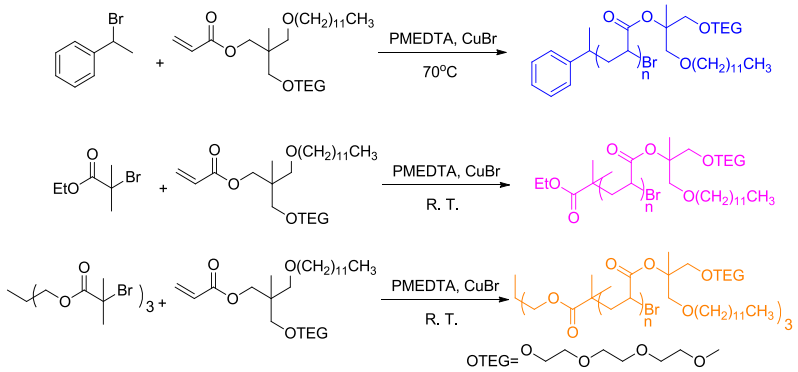

Scheme 2. Synthesis of the one-arm and multiple-arm polymer

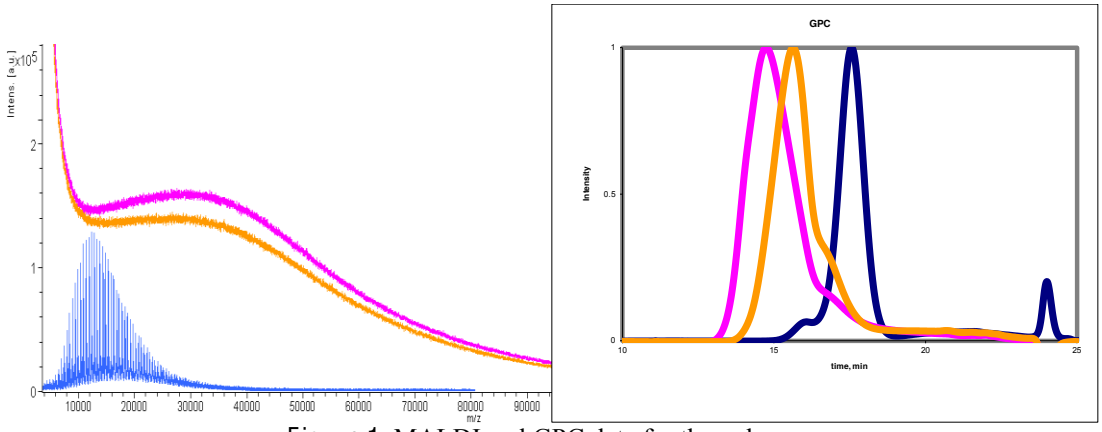

Figure 1. MALDI and GPC data for the polymers

Table 1. Molecular weight and PDI calculated by MALDI and GPC

	MALDI		GPC	
	Molecular weight	PDI	Molecular weight	PDI
Polymer 1	15.4k	1.09	12.0k	1.23
Polymer 2	35.7k	1.20	51.7k	1.64
Polymer 3 (3-arms)	34.1k	1.19	45.6k	1.55

The polymers could be prepared using standard ATRP conditions, enabling control of their molecular weights, as confirmed by both MALDI-TOF MS and GPC. The somewhat broad polydispersities were expected given the sterically bulky monomer.

3 Result and discussion

3.1 UV, fluorescence studies of the polymers

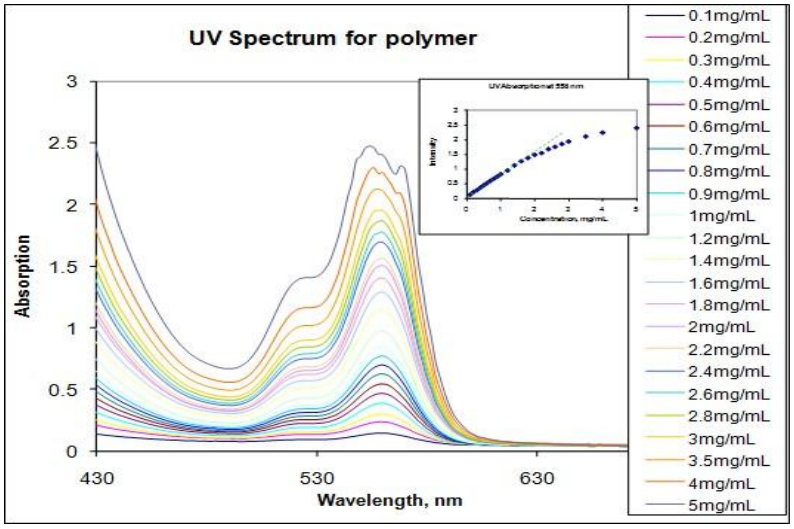

Figure 2. UV absorbance of linear 12k polymer with different concentration in hexane, the dye used for the encapsulation was rose Bengal. *Insert:* UV intensity at 572nm as a function of concentration, the CMC was determined to be <0.1mg/mL, and shifting slope suggests changes in aggregation at higher concentration

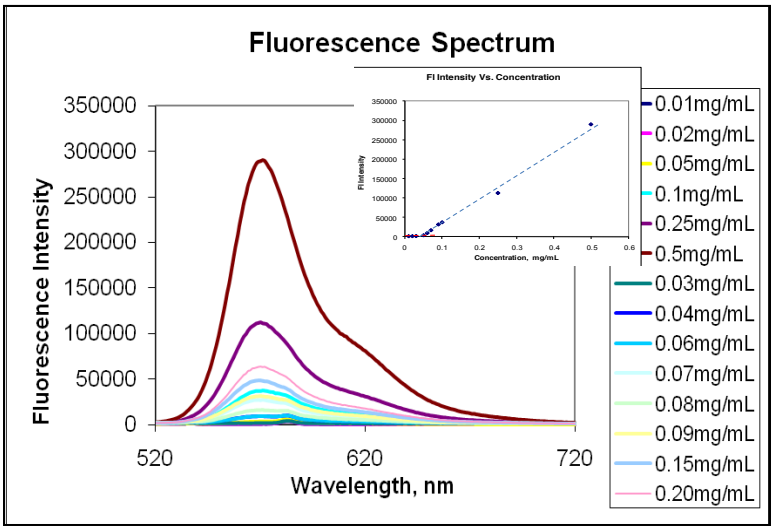

Figure 3. Fluorescence spectrum of linear 36k polymer with different concentration in hexane, the dye used was rose bengal. *Insert*: Fluorescence Intensity at 572nm as a function of concentration, the critical micelle concentration was determined to be 0.04mg/mL.

The linear 12k and 3-arms 34k amphiphilic homopolymer gave similar UV and fluorescence spectrums as showed here, the CMC were determined to be 0.1mg/mL and 0.06mg/mL, respectively.

The UV and fluorescence studies showed that the amphiphilic homopolymer could form micelles in non-polar organic solvents, such as hexanes. Rose bengal, a polar dye which exhibits negligible solubility in non-polar solvents, could dissolve in a hexane solution of the amphiphilic homopolymer, as judged by its UV absorption and fluorescence emissions. The fluorescence signal relative to polymer concentration exhibited a linear trend for concentrations above 0.1mg/mL but below this CMC, the polymer disaggregated, and exhibited no ability to encapsulate dye.

4. Conclusion

Amphiphilic homopolymers with differing molecular weight and architecture were synthesized using ATRP and characterized by NMR, GPC and MALDI. Further studies using DLS, and UV/visible spectrophotometry confirmed the formation of micelle in solution. The critical micelle concentrations of these polymers were determined, and were particularly low, making amphiphilic homopolymers promising candidates for drug delivery.

5. Acknowledgments

The current work is funded by the NSF EPSCoR LA-SiGMA project under award #EPS-1003897.

6. References

[1] Torchilin, V. P. J. *Controlled Release* 2001, *73*, 137-172.
[2] Basu, S.; Vutukuri, D.; Shyamroy, S.; Sandanaraj, B. S.; Thayumanavan, S. *J. Am. Chem. Soc.* 2004, *126,* 9890–9891.
[3] Matyjaszewski, K; Xia, J. *Chem. Rev.* 2001, *101,* 2921-2990.
[4] Willham, K. A.; Laurent, B. A. Grayson, S. M. *Tetrahedron Lett.* 2008, *49,* 2091-2094.

Searching for Novel Spin-Coupled Coordination Complexes: Mn, Fe and Co Polynuclear Galactarates

Pavel Kucheryavy[1], Naijue Zhu[1], Cheryl Stevens[1], Galina Goloverda[1], Alexander Burin[2], Chisom Ezenwoye[1], Uchenna Onwuegbusi[1] and Vladimir Kolesnichenko[1]

[1]Chemistry Department, Xavier University; and [2]Chemistry Department, Tulane University

Abstract: Aiming the preparation of novel polynuclear transition metal complexes with spin-coupled metal ions, base-promoted metal ion condensation reactions were studied in aqueous solutions at a presence of galactaric acid. Depending on pH and oxidation number of the metal, it was found that three types of complexes form with Mn, Fe and Co. Chain-structured metal (II) coordination polymers form with metal to ligand ratio of 1:1 under acidic or neutral conditions. Under basic conditions, soluble complexes with metal to ligand ratio of 2:1 are produced. These compounds undergo spontaneous oxidation under open air yielding metal (III) complexes with metal to ligand ratio of 3:1. Depending on pH, these compounds exist in aqueous solutions in different protonated forms, for example neutral and anionic salts with a variety of cations were obtained from acidic and basic solutions respectively.

Keywords: manganese, iron, cobalt mucate complexes; galactarate complexes

1. Introduction

Single-molecule magnets are described as inorganic coordination compounds with well-defined composition and low-dimension structure, and which contain several magnetically-coupled paramagnetic metal ions. Study of these compounds can lead to understanding of the structure and magnetism relationship, and ultimately to obtaining small-dimension magnets useful for biomedical application, computer and microelectronic technologies. This paper describes a portion of the research project entitled: "Iron Oxide Molecular Clusters as Building Blocks of Non-volatile Memory". This is a multidisciplinary project being accomplished in collaboration with computational chemists A. Burin and J. Perdew (Tulane University) and magnetism-physicist L. Spinu (University of New Orleans). Present introductory paper describes only experimental results on the synthesis and structural characterization of novel polynuclear coordination complexes. Computational studies and magnetic characterization components of the project will be reported in forthcoming papers.

Aiming the preparation of novel polynuclear coordination complexes with spin-coupled metal ions (single-molecule magnets), we studied condensation of transition metal (Mn, Fe and Co) aqua ions at a presence of galactaric (mucic) acid. This acid is one of the sugar acids, which is a six-carbon dicarboxylic acid containing two α- and two β-OH groups. It is a polydentate bridging ligand which can direct the assembly differently, depending on conditions. Such a property of the acid originates from its molecular structure, which can adopt different conformations promoting the formation of two or more chelates with different metal ions. As a ligand of weak field, it does not significantly affect the spin state of a metal center, so we could expect formation of a ferromagnetic coupling. There are only few reports in the literature describing metal complex formation with

galactaric acid. Most commonly, it uses its carboxyl groups simultaneously with adjacent (α) OH-groups to chelate metal ions, so that galactarate ion appears as di- or tetra-anion [1-5]. Rather rare example of hexa-deprotonated ligand is realized in copper (II) galactarate structure [3]. Long-range structures vary from zero-dimensional [3,4] to 1D [1,2] or 3D [5] coordination polymers.

2. Experimental

All chemicals were purchased from Aldrich and used as received. Manipulations with air-sensitive samples were performed using Schlenk technique. FT-IR spectra were obtained using Thermo Nicolet 380 spectrometer; UV-VIS spectra were obtained using Beckman DU800 UV-Vis spectrophotometer; single-crystal X-ray diffractometry experiments and crystal structure analysis were done on Bruker Smart X2S diffractometer; powder X-ray diffraction experiments were done on Rigaku MiniFlex II diffractometer; thermogravimetric analysis experiments were done on Perkin Elmer STA6000 thermal analyzer.

3. Results and Discussion

a. Complexation reactions

In order to determine the preferential metal to ligand ratio in metal galactarate coordination complexes, we carried out series of pH-metric and spectrophotometric titrations. In some experiments, solutions containing metal ions (Mn, Fe, Co) and galactaric (mucic) acid, $H_2H^{\alpha}{}_2H^{\beta}{}_2Mu$, in a fixed proportion were titrated with base (NaOH). In other experiments, galactaric acid and base (NaOH) in a fixed proportion were titrated with metal salt. The equivalence point determined by pH-metering and spectrophotometry, helped to determine the stoichiometry of the reactions and therefore possible composition of the coordination complexes in solutions. The stoichiometry determined from these titrations was then used in synthesis experiments. Obtained products were characterized by thermogravimetric analysis (TGA), infrared spectrometry (FT-IR), powder and single-crystal X-ray diffractometry.

In most of titration experiments, the first equivalence point corresponded to the ratio of M^{2+} : $H_2H_2H_2Mu$:OH^- as 1 : 1 : 2 (M = Mn, Fe, Co). At this point we observed formation of a precipitate with composition of $MH^{\alpha}{}_2H^{\beta}{}_2Mu$, which included hydration water, depending on metal.

$$M^{2+} + H_2H^{\alpha}{}_2H^{\beta}{}_2Mu + 2OH^- \rightarrow MH^{\alpha}{}_2H^{\beta}{}_2Mu + 2H_2O$$

Further addition of base leads to dissolution of the precipitate at the second equivalence point, and resulting solutions are highly oxygen-sensitive. Similar solutions can be obtained when metal to ligand ratio is 2:1, and titration experiments show evidence to the following reaction stoichiometries:

$$2M^{2+} + H_2H^{\alpha}{}_2H^{\beta}{}_2Mu + 4OH^- \rightarrow M_2H^{\beta}{}_2Mu + 4H_2O$$

$$2M^{2+} + H_2H^{\alpha}{}_2H^{\beta}{}_2Mu + 6OH^- \rightarrow M_2(OH)_2H^{\beta}{}_2Mu^{2-} + 4H_2O$$

Products of these reactions were isolated from solutions as glossy solids with variable content of hydration water, causing difficulty for elemental analysis interpretation.

Behavior of M^{3+} - $H_2H_2H_2Mu$ - OH^- system appears to be more complicated. Iron (III) containing system was studied in more details than Mn (III) and Co (III) systems because simple Fe(III) salts are readily available, and the product of reactions is redox stable over a wide range of pHs. Series of spectrophotometric and potentiometric titrations for Fe^{3+} - $H_2H_2H_2Mu$ mixtures showed formation of several species at different pH values. Based on the titration equivalence points, we obtained the following metal to ligand ratios: Fe^{3+}: $H_2H_2H_2Mu$ in acidic solution is 4:3, and Fe^{3+} : $H_2H_2H_2Mu$: OH^- under basic conditions is 3:1:9.5. Attempts to isolate these compound lead to formation of insoluble amorphous precipitates with compositions of $Fe_4(H_2Mu)_3$ and $Fe_3Mu(OH)_3$, based on results of TGA. If aqueous base is added to these solids, they readily dissolve to form a reddish-brown solution; complete dissolving was observed at a ratio of Fe^{3+} : $H_2H_2H_2Mu$: OH^- equal to 3:1:10.

$$3Fe^{3+} + H_2H^{\alpha}{}_2H^{\beta}{}_2Mu + 9OH^- \rightarrow Fe_3Mu(OH)_3 + 6H_2O$$

$$3Fe^{3+} + H_2H^{\alpha}{}_2H^{\beta}{}_2Mu + 10OH^- \rightarrow Fe_3Mu(OH)_4^- + 6H_2O$$

In our initial experiment we used NaOH as a base, which afforded us a very soluble in water, but completely insoluble in organic solvents compound. Starting from $Fe_3Mu(OH)_3$, we prepared a series of water-soluble compounds with Na^+, K^+, Cs^+, NH_4^+, and water- and organic solvents-soluble compounds with NMe_4^+, NBu_4^+, $NBzMe_3^+$, DMAP, DABCO, and PPh_4^+. These compounds were isolated from aqueous and non-aqueous solutions as solids and analyzed by IR, XRD, and TGA, however all of them were amorphous. Supposedly, they contain hexa-deprotonated galactarate ligand.

Spontaneous oxidation under open air of the alkaline solutions containing Mn and Co galactarates, leads to formation of species which are presumably analogous to aforementioned iron (III) galacrarate.

$$12M^{2+} + 4H_2H^{\alpha}{}_2H^{\beta}{}_2Mu + 3O_2 + 28OH^- \rightarrow 4M_3Mu(OH)_4^- + 18H_2O$$

Under strongly acidic conditions, iron(III) complex transforms into another complex with metal to ligand stoichiometry of 4:3, whereas cobalt (III) complex undergoes reduction into aforementioned Co(II) 1:1 salt. Manganese (III) complex undergoes spontaneous oxidation under open air producing manganese (IV) oxide. Attempts to crystallize these complexes with different cations and/or organic ligands are ongoing.

Controlled oxidation of alkaline cobalt galactarate leads to formation of a green crystalline product with composition of $Co_2H_2H_2Mu{\cdot}4H_2O$, which is insoluble in most of solvents. We are currently trying to obtain a single crystal of this compound, suitable for X-Ray analysis.

b. Crystal and molecular structure analysis

We isolated insoluble polycrystalline solids for Mn^{2+}, Fe^{2+}, Co^{2+}, and Ni^{2+} galactarates with 1:1 stoichiometry, but only manganese salt $MnH_2H_2Mu{\cdot}4H_2O$ formed single crystals suitable for X-ray analysis. It has a polymeric chain

structure where each manganese cation is bound to two galactarate anion via chelates formed by carboxylate and α-hydroxy groups (Fig. 1). The key feature of this complex is in manganese coordination number 7 and pentagonal bipyramidal coordination polyhedron. Since metal atoms are separated by a large ligand, we would not expect any significant magnetic interaction between them.

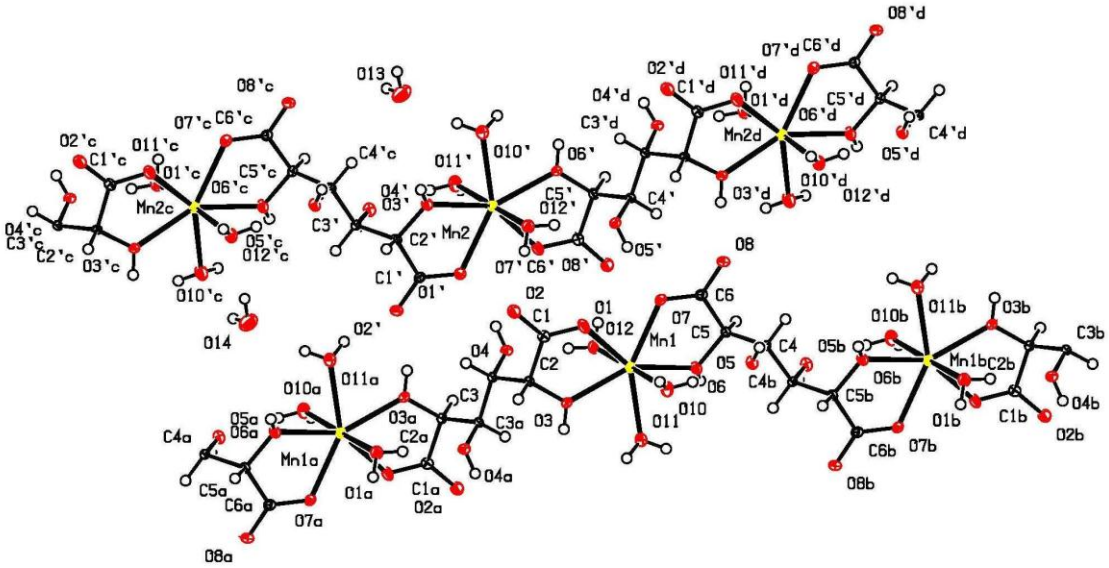

Figure 1. Crystal packing of $MnH^{\alpha}_{2}H^{\beta}_{2}Mu{\cdot}4H_2O$ (hydrogen atoms are omitted for clarity)

4. Conclusion

Galactaric (mucic) acid is a versatile complexing agent capable of forming metal complexes with large variety of compositions and structures, depending on the charge of a metal ion and on the pH. The trivalent Mn, Fe and Co complexes are likely to be polynuclear and have potential for showing magnetic spin coupling.

5. Acknowledgments

The current work is funded by the NSF EPSCoR LA-SiGMA project under awards #EPS-1003897 and PREM DMR-0934111. Research was also supported by the NIH SCORE SC3GM088042 and NIH-RCMI Grant # 1G12RR026260-01.

6. References

[1] B. Sheldrick, W. Mackie and D. Akrigg, *Acta Cryst.*, 1989, C45, 191
[2] B. Sheldrick and W. Mackie, *Acta Cryst.*, 1989, C45, 1072.
[3] P. Klufers, G. Kramer, H. Piotrowski and J. Senker, Z. Naturforschung, 2002, 57b, 12, 1446.
[4] A. Lakatos, R. Bertani, T. Kiss, A. Venzo, M. Casarin, F. Benetollo, P. Ganis, and D. Favretto, *Chem. Eur. J.* 2004, 10, 1281.
[5] B. F. Abrahams, M. Moylan, S. D. Orchard and R. Robson, *Cryst. Eng. Comm*, 2003, 5(55), 313.

Sharp Contrast of Strain Relaxation between Sr_2RuO_4 and Ca_2RuO_4 Epitaxial Thin Films

Ludi Miao, Xiaolan Zhou, Wenyong Zhang, Tijiang Liu, Jin Peng, Jin Hu, Punam Silwal, Ilan Stern, Z.Q. Mao* and Dae Ho Kim

Department of Physics and Engineering Physics, Tulane University, New Orleans, Louisiana 70118, USA

Abstract: We have grown and characterized Sr_2RuO_4 (SRO) and Ca_2RuO_4 (CRO) epitaxial thin films on various perovskite substrates. In SRO films, both disorders and electronic transport properties are found to strongly depend on the lattice mismatch between the films and substrates. Lattice parameters of these films remain nearly constant regardless of variations in thickness or substrate, indicating that the strain in SRO films is readily relaxed. On the contrary, CRO films are fully strained and their lattice constants vary with substrates. Such contrast between SRO and CRO films can be understood in terms of their distinct crystal lattices.

Keywords: Thin films, epitaxial strain, transport, ruthenates

1. Introduction

Strongly correlated layered ruthenates, $R_{n+1}Ru_nO_{3n+1}$ (R=Ca, Sr) with n=1,2,…,∞ , in the Ruddlesdon-Popper (RP) series have attracted great attention since they display a remarkable range of unique electronic and magnetic properties such as an antiferromagnetic Mott-insulating state, itinerant ferromagnetism, and metamagnetic quantum criticality [1-2]. In particular, the discovery of spin-triplet superconductivity (T_c = 1.5 K) in Sr_2RuO_4 (SRO), the n = 1 member of the RP series, has generated a great deal of interest [3]. A key signature of SRO is that its superconductivity is extremely sensitive to disorders/impurities owing to its long superconducting coherence length.

Successful growth of SRO epitaxial films on perovskite substrates $LaAlO_3$(LAO), $NdGaO_3$(NGO), $SrTiO_3$(STO), and $LaSrGaO_4$(LSGO) using pulsed laser deposition (PLD) was first reported by Madhavan *et al.* However, those SRO films did not show superconductivity due to disorder-scattering-induced pair-breaking [4]. Recently, Krockenberger *et al.* reported the observation of superconductivity with a transition temperature around 1 K in a SRO epitaxial film grown on a $(LaAlO_3)_{0.3}(SrAl_{0.5}Ta_{0.5}O_3)_{0.7}$ (LSAT) substrate [5]. Since LSAT is the closest to SRO in lattice constants compared to other substrates, disorders caused by lattice mismatch is likely minimized such that superconductivity could survive. This implies that lattice mismatch between the film and substrate can be a key parameter in governing the electrical properties of SRO thin films. In this article, we address this issue systematically using SRO epitaxial films grown on various substrates including LAO, STO, LSAT, LSGO and NGO. We find that both the residual resistivities ρ_{res} and density of disorders of these films systematically

increase with lattice mismatch. The lattice parameters of these films, however, remain invariant, indicating that in SRO thin film strain is readily relaxed regardless of the substrate, in stark contrast with fully strained Ca_2RuO_4 (CRO) epitaxial films involving lattice mismatch.

2. Experimental Procedures

We have grown SRO and CRO epitaxial thin films using the PLD. Single crystalline LAO, LSGO, NGO, LSAT and STO all with (001) pseudo-cubic orientations were used as substrates. High-resolution four circle X-ray diffraction (HR-XRD) was used to characterize the structure and crystalline quality of films. The resistivity of thin film samples was measured using a standard 4-probe method in a Physical Property Measurement System (PPMS, Quantum Design).

3. Results and Discussion

We present the XRD data of the 150 nm-thick SRO/LSAT film in Fig. 1 as an example. High quality of crystallization of the film with c-orientation can be seen clearly from the strong (00l) diffraction peaks shown in Fig. 1(a) and sharp rocking curve in the inset with a full width at half maximum $\Delta\theta_{FWHM} \sim 0.02°$. As shown in Fig. 1(b) and 1(c), the same four-fold symmetry is observed for both SRO (103) and LSAT (101), confirming an epitaxial relation with SRO [100] || LSAT [100].

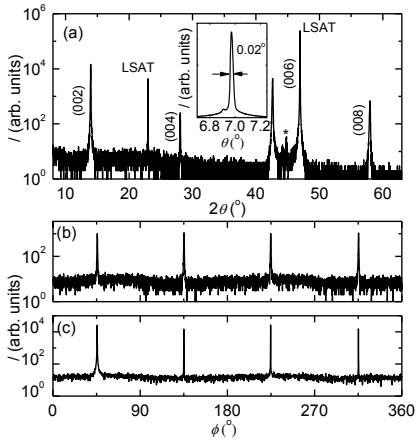

Fig. 1. (a) X-ray diffraction pattern (2θ-θ scan) of a 150 nm SRO film on a LSAT (001) substrate. The inset shows the rocking curve of the SRO (002) reflection. [(b) and (c)] ϕ-scans of SRO (103) and LSAT (101) reflections, respectively.

Most of these SRO films exhibit metallic behavior in in-plane resistivity $\rho(T)$. The superconducting transition was not observed in any of these films. The residual resistivity ρ_{res} (approximately defined as the resistivity at 2 K) and the ratio of room temperature to residual resistivity (ρ_{300K}/ρ_{res}) of these films shows remarkable variation with

substrate. The SRO/LSAT films have the smallest ρ_{res} (~6.6-81 $\mu\Omega$cm) and the largest ρ_{300K}/ρ_{res} (~ 24.0-5.5). The SRO/STO films have the greatest ρ_{res} ranging from 118 to 5700 $\mu\Omega$cm and the smallest ρ_{300K}/ρ_{res} of 1.4-5.2.

Such significant variation in the electronic properties of SRO films on different substrates is likely to originate from their different levels of structural disorders. In order to characterize the disorders of these films, we have measured the rocking curve $\Delta\theta_{FWHM}$ of the (002) reflection for each film. As shown in Fig. 2(a), ρ_{res} increases systematically with increasing $\Delta\theta_{FWHM}$, indicating that structural disorder is truly a key parameter dominating electronic properties of SRO films.

The substrate dependence of the films' ρ_{res} and $\Delta\theta_{FWHM}$ described above implies that the degree of disorders may depend on the lattice mismatch. Among our films, the SRO/LSAT has the least lattice mismatch, with the relative magnitude of mismatch $(a_{sub}-a_{SRO})/a_{SRO} = -0.05\%$, where a_{sub} and a_{SRO} represent lattice constants of substrate and SRO bulk single crystal, respectively. In order to examine how disorders depend on the lattice mismatch in SRO films, we plot $\Delta\theta_{FWHM}$ vs. $(a_{sub}-a_{SRO})/a_{SRO}$ for all the films in Fig. 2(b). $\Delta\theta_{FWHM}$ for films grown on the same substrate increases as the magnitude of mismatch increases (the dashed-line). In other words, a larger lattice mismatch causes a higher density of disorders.

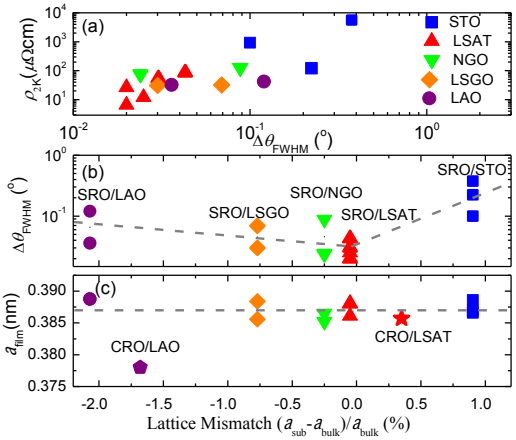

Fig. 2. (a) Residual resistivity as a function of $\Delta\theta_{FWHM}$, the full width at half maximum of the SRO (002) rocking curve. (b) The full width at half maximum of the SRO (002) rocking curve $\Delta\theta_{FWHM}$ as a function of the lattice mismatch defined as $(a_{sub}-a_{SRO})/a_{SRO}$ for various SRO thin films. (c) The in-plane lattice constants of SRO and CRO thin films (a_{SRO} and a_{CRO}) vs. the lattice mismatch.

We have also measured the lattice constants for all of SRO thin film samples by XRD reciprocal space map. We found that SRO films on various substrates all have similar lattice constants, as shown in Fig. 2(c). The strain relaxation of SRO film will result in structural disorders, whose density increases with increasing lattice mismatch.

To understand the strain relaxation of SRO, we have also grown CRO epitaxial thin films on LAO and LSAT substrates for comparison. In sharp contrast to SRO films, CRO film is fully strained on LAO (LSAT) substrates even with -1.7% (0.3%) lattice mismatch,, as seen in Fig. 2(c). Our magnetic and transport measurements reveal that the CRO/LAO film has an itinerant ferromagnetic ground state, rather than the Mott-insulating state seen in bulk CRO.

The sharp contrast between the strain states of SRO and CRO films can be understood in terms of their distinct crystal lattices. As noted above, SRO possesses a tetragonal structure without involving any structural distortion, whereas the structure of CRO is strongly distorted owing to smaller ionic radius of Ca^{2+}, manifested in the rotation, tilting, and flattening of RuO_6 octahedra. Strong structural distortion apparently gives rise to a more active lattice degree of freedom in CRO than SRO, which leads CRO's structure to be more susceptible to pressure.

4. Conclusion

We have grown *c*-oriented epitaxial $Sr_2RuO_4$and Ca_2RuO_4 thin films on various perovskite substrates using pulsed laser deposition. Strain is relaxed in all Sr_2RuO_4 films, regardless of substrate, generating structural disorders. The degree of disorders increases as the lattice mismatch between Sr_2RuO_4 and substrate increases. The electronic properties of Sr_2RuO_4 films are governed by these disorders. Ca_2RuO_4, however, has a more active lattice degree of freedom and thus allows for epitaxial growth of fully strained films. These results provide a useful reference for us to understand the general relationship between strain effect and lattice distortion in epitaxial thin films of perovskite oxides.

5. Acknowledgments

This research is supported by the LA-SiGMA program under award #EPS-1003897 and DOD ARO under Grant No. W911NF0910530.

6. References

[1] S. Nakatsuji, S. Ikeda, and Y. Maeno, J. Phys. Soc. Jpn. 66, 1868 (1997).

[2] F. Nakamura, T. Goko, M. Ito, T. Fujita, S. Nakatsuji, H. Fukazawa, Y. Maeno, P. Alireza, D. Forsythe, and S. R. Julian, Phys. Rev. B 65, 220402 (2002).

[3] Y. Maeno, H. Hashimoto, K. Yoshida, S. Nishizaki, T. Fujita, J. G. Bednorz, and F. Lichtenberg, Nature 372, 532 (1994).

[4] S. Madhavan, D. G. Schlom, A. Dabkowski, H. A. Dabkowska, and Y. Liu, Appl. Phys. Lett. 68, 559 (1996).

[5] Y. Krockenberger, M. Uchida, K. S. Takahashi, M. Nakamura, M. Kawasaki, and Y. Tokura, Appl. Phys. Lett. 97, 082502 (2010).

Simulating Nanoparticle Movement in Tumor Tissue Blood Vessels

Podduturi Vishwa Priya[1], Pedro Derosa[1,2]

[1]Institute for Micromanufacturing, Louisiana Tech University, Ruston.
[2]Department of Mathematics and Physics, Grambling State University, Grambling.

Abstract: Chemotherapy, one of the most common treatments for cancer, can affect the patient's living condition by damaging the healthy tissue due to the non-specific delivery of the drug. In an attempt to minimize the collateral damage, nanoparticles are being used for a targeted delivery of drugs thereby reducing the dose to healthy tissue. In this paper a model that combines random walk with diffusion principles is presented. Nanoparticles movement in a cylindrical tube with dimensions similar to the tumor blood capillary is simulated. The particle drift velocity is calculated from the Hagen-Poiseuille equation that is modified here to adjust the profile to that described elsewhere. The velocity profile at the pore is obtained by vector addition of velocities along and across the blood vessel. The delivery of nanoparticles to the tumor is obtained as a function of blood pressure, pore size, pressure gradient across the pore, and nanoparticle size and concentration. The results indicate that the number of nanoparticles entering the tumor tissue increases with pore size, blood pressure, and nanoparticle concentration, however in this last case, the ratio of nanoparticles going into the tumor to the total number of nanoparticles in blood decreases.

Keywords: Nanoparticle delivery, Tumor Tissues, Monte Carlo, fluid dynamics.

1. Introduction

Cancer is a deadly disease affecting many people all over the world. It can be treated by surgery, radiation therapy, chemotherapy etc. or a combination of them. Surgery may be very complicated or not even possible when it is spread to multiple areas of the body. In radiation therapy, radiation can be targeted to the desired area but the damage to surrounding healthy tissue is almost unavoidable. In chemotherapy, the drug may unfortunately confuse rapidly dividing healthy cells of the body, such as bone marrow or hair cells, with cancer cells leading to hair loss or more serious anemia, bleeding, and clotting problem[1]. To minimize those side effects, a more efficient and effective mechanism for specific and targeted drug delivery is a necessity. Polymeric nanoparticles, polymeric micelles, dendrimes, liposomes, viral nanoparticles are some of the nanoparticles being studied as potential drug delivery vehicles[2]. The study of the characteristics of the nanoparticle diffusion in blood vessels and out of them into tumors is important in order to guide the delivery process.

2 Model Description:

In the model presented here, the flow of nanoparticles in a segment of the blood vessel with a single pore is simulated. The model was developed using matlab [3].

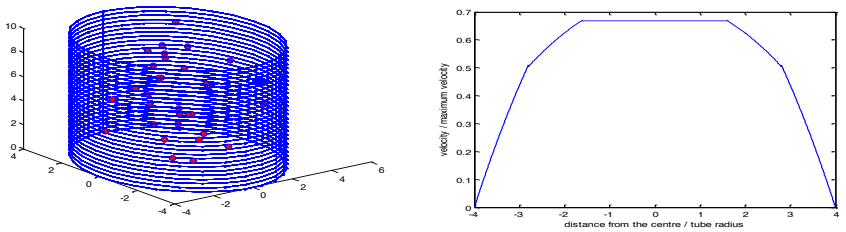

(a) (b)

Figure 1: (a) Nanoparticles uniformly distributed in a segment of a blood vessel with a single pore simulated in matlab (b) Velocity profile obtained by flattening the center of the parabolic profile given by the Hagen-Poiseuille equation (1), according to the profile reported in reference [4].

Nanoparticles are considered spherical in shape and are initially distributed uniformly throughout the cylinder. Nanoparticle motion is simulated as a superposition of two different motions, one produced by the fluid dragging nanoparticles along the blood vessel and a second motion due to random collisions. The displacement due to the fluid drag is considered to have a Hagen-Poiseuille profile, shown in equation 1, [5]. This profile, however needs to be modified to account for the effect of red blood cells. The effect of red blood cells on the velocity profile of Plasma, was predicted by Wong and his group [4] to be parabolic but with a blunt center. Figure 1 (b) shows the profile used in this work that closely resembles that in ref [4] .

$$V = \frac{P(R^2 - r^2)}{4\eta l} \tag{1}$$

Where V= velocity of the nanoparticle; P= Pressure drop across the blood vessel
R= Radius of the blood vessel; r= radial coordinate of the nanoparticle
η = dynamic viscosity of the blood plasma, 1.1×10^{-3} Pa − Sec; l = length of the blood vessel.

The displacement due to the over imposed Brownian motion is calculated by randomly selecting a hoping distance from 0 to a maximum, and randomly selecting the inclination and azimuth angles between 0 and π and 0 and 2π respectively. The maximum displacement due to the random movement is fixed and it is smaller than the particle radius and smaller than the displacement due to the velocity of the flow. The direction of the flow is along the axis of the blood vessel except in the vicinity of the pore. Near the pore, there is a velocity component in the radial direction which is a result of the pressure gradient along the pore. Hence the velocity at the pore is the resultant of the velocities along the blood vessel and along the pore. The component of the velocity in the direction of the pore is considered to follow the unmodified Hagen-Poiseuille profile. The direction of the flow is supported by a simulation of fluid dynamic done with COMSOL[6].

3. Results

The nanoparticle delivery to the tumor tissue is simulated for various size of nanoparticles and different pore size. The uptake of nanoparticles by the tumor increased with the increase in pore size. This simulation si done in

two ways, in one case, a single pore size is considered (Figure 2a), in the second case, a Gaussian distribution centered on a particular pore size is considered (Figure 2b). The percent of nanoparticles entering tumor tissue is greater for a Gaussian distribution for every pore size than for a single pore size since the presence of larger pores in the former case increases the nanoparticle delivery. Also, the particle absorption profile when pore size has a Gaussian distribution, is closer to the experimental results conducted by G. Kong and his group[7] than that of the single size pores indicating that tumor blood vessel have a distribution of pore size rather than pores of single size as expected.

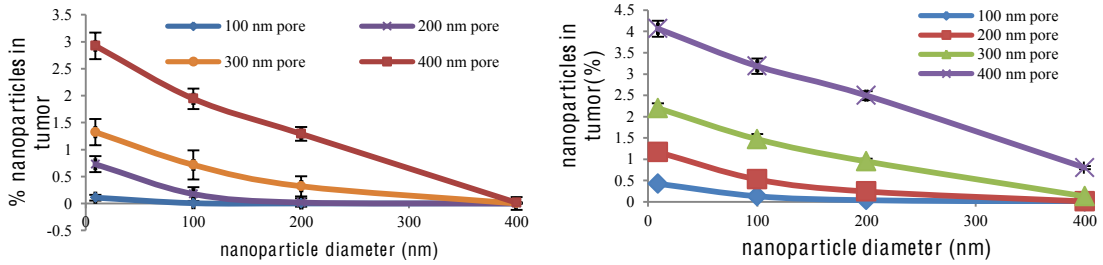

(a) (b)

Figure 2: (a) simulations with a single size of pores (b) simulations with a Gaussian distribution of pore sizes with a mean of 100- 500 um and variance of 100 um.

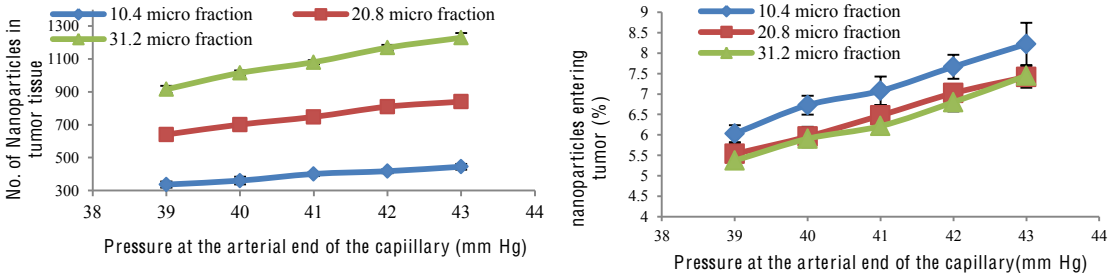

(a) (b)

Figure 3: (a) number of nanoparticles (b) percent of total nanoparticles in the tumor tissue as a function of blood pressure.

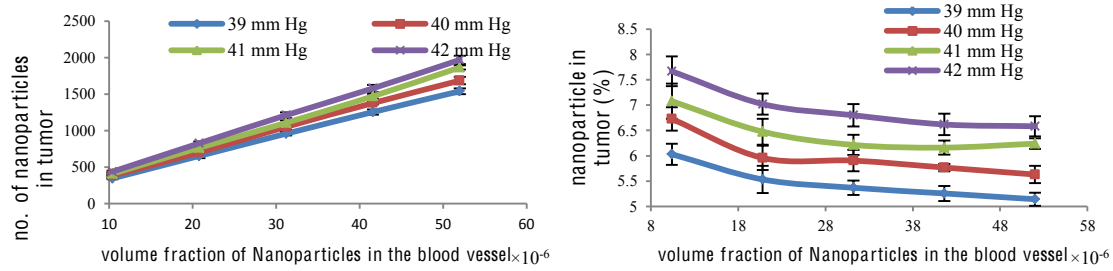

(a) (b)

Figure 4: (a) number of nanoparticles (b) percent of total nanoparticles in the tumor as a function of volume fraction of nanoparticles in the blood capillary.

Simulations are also performed as a function of blood pressure and the nanoparticle concentration. The number of nanoparticles delivered to a tumor is observed to increase with increasing blood pressure as well as with increasing concentration, however, while the percentage of nanoparticles delivered increases with blood pressure it decreases with concentration, this indicates that as the total concentration of particles in blood increases, a larger percentage of them are left undelivered to the tumor.

4. Conclusion

The study of the effect of pore size and nanoparticle size on the drug delivery to tumor tissue indicates that nanoparticle delivery increases with pore size and decrease with nanoparticle size. Any mechanisms which can increase the pore size of tumor blood vessels leads to an increased drug delivery. Smaller nanoparticles have more chance of passing through the leaky walls of tumor blood vessel, which however will also increase the delivery to healthy tissue and some care should be taken, nanoparticles should be large enough to escape the pores of normal blood vessels. Increased blood pressure can reduce the nanoparticles remaining in the blood stream by increasing their delivery to the tumor. Increased concentration of the nanoparticles in blood, leads to larger amount of nanoparticles in the tumor but also increases the number of nanoparticles remaining in the blood stream, not only in number but also in percentage.

5. Acknowledgments

The current work is funded by NSF through the "Louisiana Alliance for Simulation-Guided Materials Applications- LA-SIGMA", Federal Award Number: EPS-1003897

6. References

[1] A. Coates, *et al.*, "On the receiving end--patient perception of the side-effects of cancer chemotherapy," *Eur J Cancer Clin Oncol*, vol. 19, pp. 203-8, Feb 1983.

[2] K. Cho, *et al.*, "Therapeutic Nanoparticles for Drug Delivery in Cancer," *Clinical Cancer Research*, vol. 14, pp. 1310-1316, March 1, 2008 2008.

[3] MATLAB version 7.8. Natick, Massachusetts: The MathWorks Inc., 2009.

[4] T. Wang and Z. Xing, "Characterization of Blood Flow in Capillaries by Numerical Simulation " *Journal of Modern Physics* vol. 1, pp. 349-356 2010.

[5] G. A. Truskey, *et al.*, *Transport phenomena in biological systems*, 2nd ed. Upper Saddle River, N.J.: Pearson Prentice Hall, 2009.

[6] www.comsol.com.

[7] G. Kong, *et al.*, "Hyperthermia Enables Tumor-specific Nanoparticle Delivery: Effect of Particle Size," *Cancer Research*, vol. 60, pp. 4440-4445, August 8, 2000 2000.

Simulation of Propylene Carbonate as a Solvent for Electrochemical Double-layer Capacitors

G. G. Hoffman,[1] R. Mariano,[2] N. Pesika,[1] L. R. Pratt,[1] S. W. Rick,[2] X. You[1]

[1]Department of Chemical & Biomolecular Engineering, Tulane University
[2]Department of Chemistry, University of New Orleans

Abstract: Molecular dynamics simulations are in progress on (a) bulk liquid propylene carbonate (PC), force-field model and electron-density-functional based *ab initio* molecular dynamics (AIMD), with/without dispersion corrections; (b) PC fluid droplet; and (c) PC droplet on graphite. The measured contact angle of a PC droplet on graphite, reported here, shows that PC wets graphite effectively, though not completely. Simulations with a GAFF force-field leads to complete wetting of a model graphite surface by a PC droplet. Ongoing AIMD work with *dispersion-correction* electron-density-functional models, and further exploitation of contact angle measurements are expected to lead to a refined force-field model for large-scale molecular dynamics studies of electrochemical double-layer capacitors based on nanotube forests.

Keywords: propylene carbonate, molecular dynamics simulation, graphite, contact angles

1. Introduction

The performance of electrochemical double-layer capacitors (EDLCs) is expected to be sensitive to molecular-scale interactions involving the solvent and solution, yet compelling simulation testing of realistic possibilities has been almost non-existent [1]. Propylene carbonate (PC) is the most common choice of solvent for electrolyte solutions filling EDLCs; acetonitrile is the second most common choice of solvent. *Ab initio* molecular dynamics (AIMD) simulations of PC filling a nanotube forest with currently standard methods strongly suggest that, as described by currently standard electron-density-functional models, the PC would evacuate the forest [2]. This behavior reflects the balance of attractive interactions between PC molecules and the nanotubes. Observation (Figure 1) of the contact angle of a PC droplet on graphite indicates *favorable* wetting, and thus the AIMD result with currently standard methods is undoubtedly not correct in this respect. This suggests that the description of dispersion interactions in currently standard AIMD methods, built upon electron-density-functional models, is not sufficiently accurate for this application.

Calculations in progress (TeraGrid on Kraken, http://www.nics.tennessee.edu/computing-resources/kraken) utilize *dispersion corrected* electron-density-functional models, specifically PBE-D for propylene-carbonate-filled nanotube forests. But to exploit the experimental contact angle information, we must do simulations at a larger spatial scale that permits direct observation of a contact angle. Those larger calculations are not presently possible with AIMD methods. Instead, refined force-field models will be required for those larger scale calculations. Suitable AIMD results provide one source of information for the refinement; experimental results assist in further refinement.

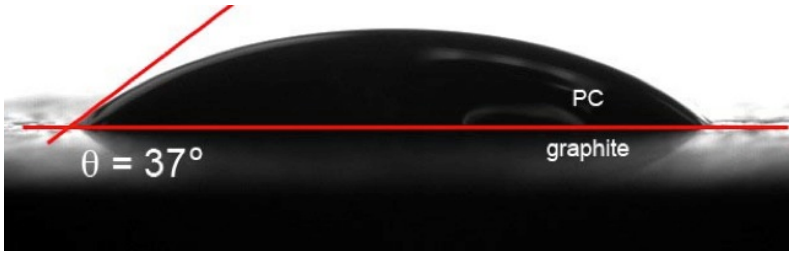

Figure 1: Propylene carbonate (PC) droplet on graphite. The low observed contact angle of 37° indicates good wetting behavior, and suggests that PC should effectively fill nanotube forests that are a basis of EDCLs.

Several types of calculations are in progress: (a) bulk liquid PC [3], force-field model and AIMD, and both PBE and PBE-D model electron-density-functional based interactions; (b) PC fluid droplet; and (c) PC droplet on graphite. Here we discuss principally the larger scale, force-field based calculations on PC. These calculations use widely available simulation codes: AMBER [4], GROMACS [5], and NAMD [6].

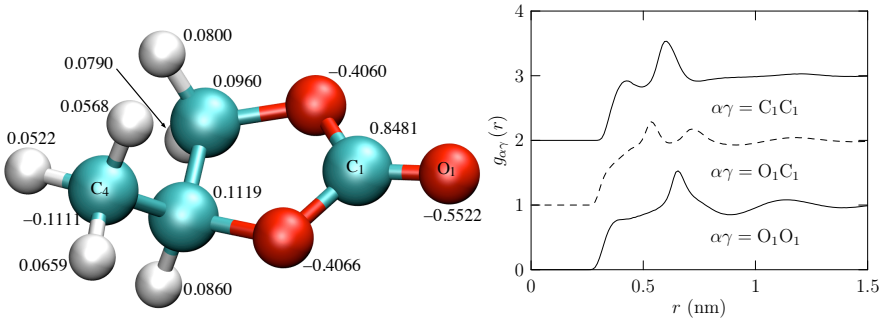

Figure 2: (left) PC molecular model for the generalized AMBER force-field (GAFF); the numbers indicate assigned atomic partial charges. (right) Radial distribution functions for the bulk liquid at p=1 atm, and T=300K. These results are in qualitative agreement with X-ray scattering data [7], but a quantitative comparison is in progress.

2. Bulk liquid PC

We summarize our previous results with a generalized AMBER force-field (GAFF) [3] (Figure 2): The dielectric constant of the liquid and its temperature derivative, the density and the compressibility of the bulk liquid are conventionally satisfactory. The bulk liquid force-field simulations will permit a close comparison with bulk liquid AIMD calculations (with/without dispersion correction for the electron-density-functional models). An interesting comparison will be with the binding energies of PC molecules to the liquid. Those results should clearly indicate the role of dispersion interactions in stabilizing the liquid. For the nanotube forest AIMD calculations, it is likely that the dispersion interactions associated with the *nanotubes* are the foremost problem of

conventional AIMD simulations, *i.e.,* neglect of dispersion interactions by electron-density-functional models is less serious for the highly polar bulk liquid PC than for the nanotube forest.

The dipole moments of the PC molecules analyzed on the basis of the maximally-localized Wannier orbitals of individual molecules constitute second interesting point of comparison for force-field simulations. The force-field model that has been used so far intentionally makes a standard error: the dipole moment of the PC molecule is significantly larger than experimental determinations for the isolated molecule. The dielectric properties then agree with experiment. Because PC functions as a solvent for electrolytes in these devices, it is important that these electrostatic characteristics be understood clearly. The calculations necessary for the desired comparison are also in progress now.

The bulk liquid simulations also provide basic data for construction of an accurate thermophysical model that should assist us in device-level modeling of EDCLs; they will evaluate conventional transport properties and dielectric relaxation processes.

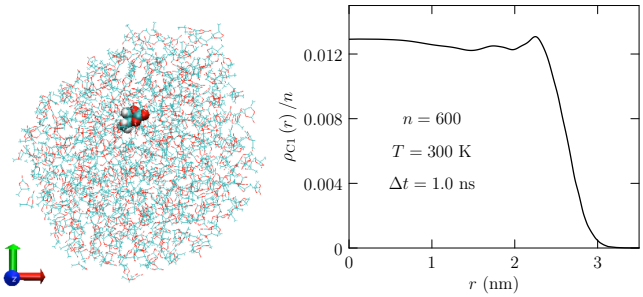

Figure 3: (left) Configuration from molecular dynamics simulation of a PC droplet. This droplet contains n=600 molecules. One PC molecule is shown as its van der Waals surface, the others are stick-figures. (right) Density profile of the mid-carbon (C1 of Figure 1) from the center-of-mass obtained from these simulations.

3. PC droplet

Calculations on PC liquid droplets will serve as a control when we proceed to the more complicated solution-electrode-interface (SEI). Molecular dynamics calculations on PC droplets are in progress, but Figure 3 shows preliminary results.

4. PC droplet on graphite

As a test of the PC-graphite interactions, we have carried out simulations of PC droplets on graphite surfaces, using the Amber GAFF force fields. These simulations contain 600 PC molecules and three layers of graphite, each containing 8856 carbon atoms. Starting with the PC molecules above the surface, the droplet moves to the surface after 300 ps of simulation time. As shown in the Figure 4, PC completely wets the graphite surface, rather

than forming a drop with a small contact angle of 37° (Figure 1). This suggests that the PC-graphite interactions of the GAFF force-field are too attractive. We are currently carrying out simulations with reduced PC-graphite interactions to reproduce the experimental contact angle.

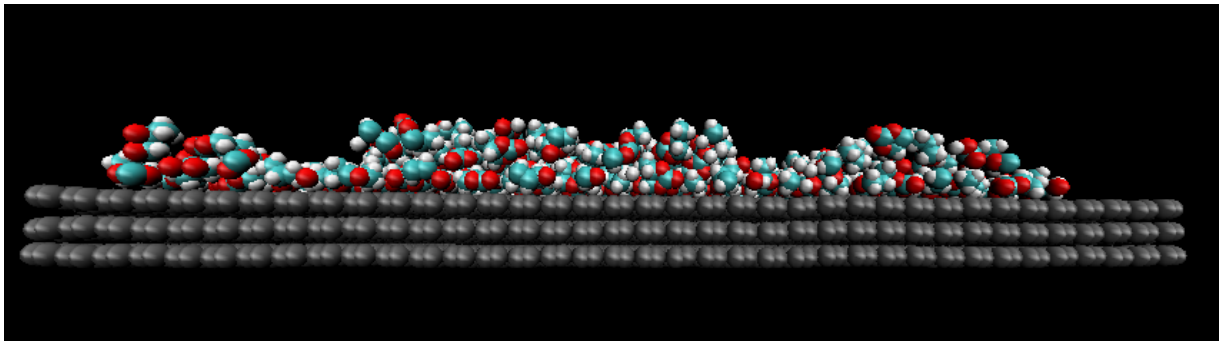

Figure 4: PC molecules (colored van der Waals spheres) on the graphite surface (gray spheres), demonstrating complete wetting of the surface with the classical Amber GAFF force fields.

5. Conclusions

AIMD with standard methods underestimates the strength of attractive PC-nanotube interactions [2]. Observation of the contact angle of a PC droplet on graphite indicates that PC should wet graphite effectively. Larger-scale simulations with a GAFF force-field [3] leads to complete wetting of the graphite surface by a PC droplet. Ongoing AIMD work with *dispersion-correction* electron-density-functional models, and further exploitation of contact angle measurements are expected to lead to a refined force-field model suitable of large-scale molecular dynamics studies of electrochemical double-layer capacitors based on nanotube forests [1].

6. Acknowledgments

The current work is funded by the NSF EPSCoR LA-SiGMA project under award #EPS-1003897.

7. References

[1] L. Yang, B. H. Fishbine, A. Migliori, and L. R. Pratt, *J. Am. Chem. Soc.* **131**, 12373—12376 (2009)
[2] G. G. Hoffman and L. R. Pratt, elsewhere in this Proceedings. The AIMD calculations used the CPMD package (http://www.cpmd.org/) with the PBE electron-density-functional model, a norm-conserving pseudo-potential (NCPP), and a plane-wave basis set cut-off of 85 Ry.
[3] L. Yang, B. H. Fishbine, A. Migliori, and L. R. Pratt, *J. Chem. Phys.* **132**, 044701 (2010)
[4] http://ambermd.org/
[5] http://www.gromacs.org/
[6] http://www.ks.uiuc.edu/Research/namd/
[7] J. C. Soetens, C. Millot, B. Maigret, and I. Bako, *J. Mol. Liq.* **92**, 201—216 (2001)

Study of the Hydrogen Storage Capability of $LaNi_5H_6$ and $KMgH_3$

Brandon Borill[1], Randall Hall[1]
Fernando Soto[2], Daniella Mainardi[2]

[1]Department of Chemistry, Louisiana State University
[2]Department of Chemical Engineering, Louisiana Tech University

Abstract: The hydrogen storage capabilities of $LaNi_5H_6$ and $KMgH_3$ were studied using grand canonical Monte Carlo simulations. The average amount of hydrogen in the metal hydrides was studied as a function of pressure and temperature. Hydrogen remains in the hydride system at lower temperatures while increasing the temperature above 400 K causes hydrogen depletion in $KMgH_3$. The rate of hydrogen loss can be slowed by increasing the pressure.

Keywords: Hydrogen storage, Monte Carlo, metal hydride

1. Introduction

Hydrogen storage in solid materials is an ongoing avenue of research that includes the study of materials such as carbon nanotubes and metal hydrides. Examples of such metal hydrides targeted in hydrogen storage research are $LaNi_5H_6$, $NaMgH_3$, $KMgH_3$, $FeMg_2H_6$, and $MgNiH_4$ [1, 2, 3, 4]. Figure 1 depicts the crystal structures for $LaNi_5H_6$ (a) and $KMgH_3$ (b).

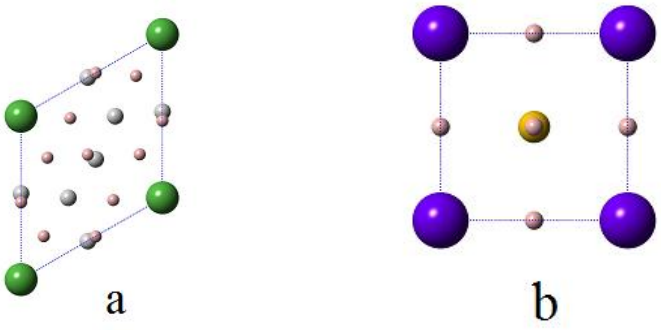

Fig. 1 (a) $LaNi_5H_6$ crystal structure and (b) $KMgH_3$ crystal structure. The pink spheres depict hydrogen atom locations: in $LaNi_5H_6$, some of the sites have 50% according to the crystal structure.

The study of these materials continues in both experimental and computational settings. The goal of this research is to discover a material that not only readily accepts hydrogen, but will also release it without a significant energy penalty. This material would also ideally be lightweight and inexpensive as well as comply with targets set by the United States Department of Energy. Metal hydrides meet the DOE requirements for volumetric capacity [5].

Unfortunately, metal hydrides suffer from a high mass density, leading some researchers to investigate carbon nanotubes as a potential hydrogen storage material [5]. Despite this, research into metal hydrides as hydrogen storage materials is still ongoing.

It is important to note that while the ideal hydrogen storage material still eludes researchers, metal hydrides are a promising avenue of research. Metals such as palladium are studied, but a material such as palladium is ultimately not desirable because of its expense [6]. Complex metal hydrides are promising because of their thermodynamic qualities. The enthalpy of hydrogen loss for $LaNi_5H_6$ is 30.1 kJ mol^{-1} and 74.2 kJ mol^{-1} for MgH_2 [7]. It is for $KMgH_3$ 99.1 kJ mol^{-1} [8].

2. Computational Procedure

The calculations used an embedded-atom method (EAM) similar to one developed in the study of hydrogen in iron [9]. Parameters for the force fields were determined using simulated annealing canonical Monte Carlo simulations to minimize a cost function that depended on energies and bulk moduli of the pure metals, alloys, and hydrides. Grand canonical Monte Carlo simulations were then used to determine the average fraction of available hydrogen binding sites in an alloy at different temperatures and pressures. All simulations were performed on machines provided by the LSU Center for Computation and Technology (CCT) and the Louisiana Optical Network Initiative (LONI).

3. Results and Discussion

The study of $LaNi_5H_6$ and $KMgH_3$ remains ongoing. Force field development is complete for $KMgH_3$ but still ongoing for $LaNi_5H_6$ due to the uncertainty in hydrogen atom location from the available crystal structure. Calculations using Materials Studio are being used to identify the lowest energy occupancy in $LaNi_5H_6$ and the energy differences between this structure and alternatives. This information will be used to fine tune the force field. A 1K canonical Monte Carlo simulation shows agreement with experimental crystal structure (Figure 2). Therefore, grand canonical Monte Carlo simulations have been performed for $KMgH_3$.

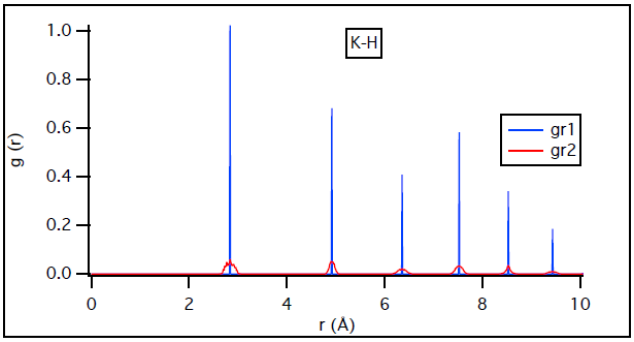

Figure 2 Sample radial distribution plot showing the interaction between K and H in $KMgH_3$. The crystal structure peaks are in blue.

The average fraction of populated hydrogen binding sites has been calculated using Grand grand canonical Monte Carlo simulations at several different temperatures and pressures (Figure 3). As expected, increasing pressure has the effect of retaining more hydrogen in the system at higher temperatures than at lower pressures. In general, the amount of hydrogen stored in the system still declines with rising temperature.

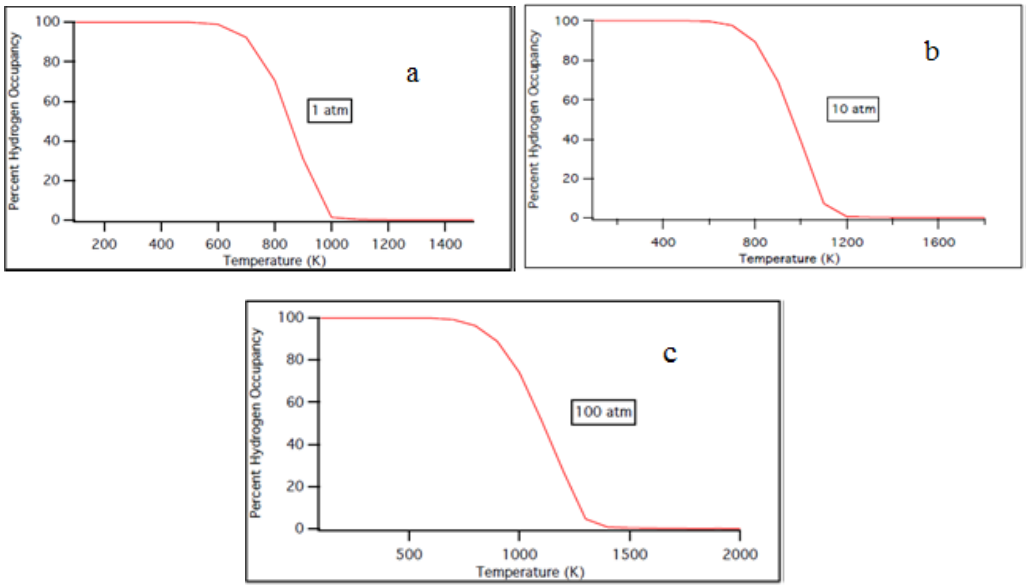

Fig. 3 Relationship between temperature and percent occupancy of hydrogen atoms at (a) 1 atm, (b) 10 atm, (c) and 100 atm.

4. Conclusions and Future Work

Initial grand canonical Monte Carlo simulations for $KMgH_3$ display a relationship between temperature and pressure with the average occupancy of hydrogen atoms in the system. Hydrogen occupancy in $KMgH_3$ begins to decrease at temperatures above 400 K. At high temperatures, less hydrogen remains in the solid (as low as below one percent hydrogen) because of a thermodynamic preference to remain in the gas phase. This effect can be slowed by increasing the pressure. We have observed that over 26% retention of hydrogen is possible at 100 atm and 1,200 K, whereas this amount of retention is not possible at lower pressures. Comparison of this work with experimental data on hydrogen uptake remains as well as calculating the free energy of the system as a function of fraction of hydrogen content.

Comparison with the results of the Butler group at LSU will be performed once the force field for $LaNi_5H_6$ is fully developed. Grand canonical Monte Carlo simulations for $LaNi_5H_6$ are ongoing. It is also planned to perform research on $NaMgH_3$ and $FeMg_2H_6$, with $FeMg_2H_6$ to be studied first.

5. Acknowledgments

The current work is funded by the NSF EPSCoR LA-SiGMA project under award #EPS-1003897.

Useful discussions with Dr. Les Butler are gratefully acknowledged. The work was accomplished using the computer resources of the Louisiana Optical Network Initiative (LONI) and the high performance computing resources at LSU.

6. References

[1] Zhang, J., Huang, Y. N., Long, C. G., Zhou, D. W., and Liu, J. S. Mat. Sci. Poland, 28, 357 (2010).
[2] Garcia, G. N., Abriata, J. P., and Sofo, J. O. Phys. Rev. B, 59, 11746 (1999).
[3] Klaveness, A., Swang, O., and Fjellvag, H. Europhys. Lett., 76, 285 (2006).
[4] Viegas, Jennifer. The Laws of Thermodynamics: An Anthology of Current Thought, 1st Ed. The Rosen Publishing Group: New York, 2006: p. 90.
[5] Gigras, Ankur, Bhatia, Suresh K., Kumar, A. V. Anil, Myers, and Alan L. Carbon, 45, 1043 (2007).
[6] Crespo, E. A., Ruda, M., and de Debiaggi, S. Ramos. Int. J. Hydrogen Energy, 33, 3561 (2008).
[7] Gupta, Ram B. Hydrogen Fuel: Production, Storage and Transport. CRC Press Group: Boca Raton, 2009, p. 383.
[8] Shinzato, Yoshifumi, Komiya, Kenji, Takahashi, Yoshitaka, Yukawa, Hiroshi, Morinaga, Masashiko, and Orimo, Shinici. Adv. Quantum Chem. 54, 245 (2008).
[9] Ramasubramaniam, Ashwin, Itakura, Mitsuhiro, and Carter, Emily. Phys. Rev. B, 79, 174101 (2009).

Surface Interactions and Transport of Single DNA Nucleotides in Nanoslits

Brian R. Novak[1], Kai Xia[1], Dimitris E. Nikitopoulos[1,2], Dorel Moldovan[1,2]

[1]Department of Mechanical Engineering, Louisiana State University
[2]Center for Bio-modular Multi-scale Systems, Louisiana State University

Abstract: Molecular dynamics simulations were used to study the interaction and transport of single DNA nucleotides in aqueous solution moving through nanometer scale slits with disordered carbon walls. The driving force was either a force proportional to the mass on each atom (body forces), or an electric field to drive the nucleotides electrophoretically. The nucleotides adsorbed and desorbed on time scales on the order of tens of nanoseconds or less. The base parts of the nucleotide tended to sit nearly flat on the surface, and the hydrophobicity of the bases determined the dynamics of the nucleotides.

Keywords: molecular dynamics, nanochannel, surface interaction, DNA, nucleotides

1. Introduction

Various technologies are being developed with their goal directed towards fast and low-cost sequencing of linear heteropolymers such as DNA. This work addresses a system for heteropolymer sequencing which would use a combination of sequential enzymatic disassembly and measurement of the flight time of each monomer as it passes through a nanochannel. The basic hypothesis is that different types of monomers in solution moving through a nanochannel will experience transit (flight) times that are dependent upon the molecular identity of the monomer, the chemical identity of the surface of the nanochannel, and its dimensions.

Using molecular dynamics simulations, we have studied the transport and dynamics of the four common DNA nucleotide 5'-monophosphates as they moved through 3.0 nanometer wide slits in an aqueous environment. This system is useful for the study of the interactions of any biological or other organic molecules such as drugs with various chemical groups in confined, non-equilibrium conditions.

2. Simulation Details

The DNA nucleotides have a single phosphate group attached to the 5' site of a deoxyribose sugar, while a nucleobase (adenine, cytidine, guanine, or thymidine) is attached at the 1' site of the sugar (Figure 1). The phosphate group of the nucleotides may be either completely un-protonated or be singly protonated near neutral pH. Above pH 7.0, the dominant form is the un-protonated one which has a net charge of -2 , and this is the form that was simulated.

The walls of the slits were composed of Lennard-Jones atoms with the same potential energy parameters as those for a carbon atom. The number density of the walls was chosen so that it matched the number density of the heavy atoms in amorphous poly(methyl methacrylate) (PMMA). The mass of the wall atoms was chosen to

reproduce the mass density of PMMA. A disordered wall structure was desired, so the walls were prepared by cutting configurations from a constant volume, bulk liquid simulation at 5000 K.

Four sets of simulations were performed: 1) equilibrium (no driving force) where the slit walls were atomically smooth, 2) the slit walls were smooth and the fluid was driven by body forces (acceleration of 264 nm/ns^2), 3) the slit walls were smooth and an electric field was applied (0.1 V/nm), and 4) the slit walls had an average rms roughness of 2.27 Å and an electric field was applied (0.1 V/nm). Each set consisted of several simulations for each nucleotide with different wall configurations. This was done to avoid any bias due to a specific wall configuration.

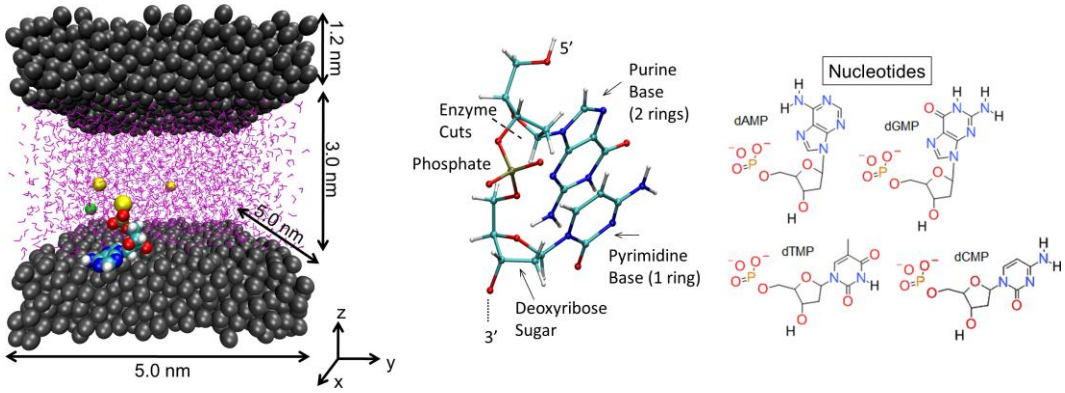

Fig. 1: Simulation system (left), DNA structure (center), and nucleotide structures (right). Colors: gray = tethered wall (300 K), tan/orange = phosphorus, red = oxygen, white = hydrogen, cyan = carbon, blue = nitrogen, yellow = sodium ion, green = chloride ion, purple = water molecule.

The simulation conditions were as follows. The slit wall atoms were harmonically tethered to their initial positions and were kept at a constant temperature of 300 K using a Berendsen thermostat [1]. For the atomically smooth cases, walls were placed such that the centers of the surface atoms were at least 3 nm apart. For the rough wall cases, they were placed so that the accessible volume to the nucleotides was approximately the same as in the smooth cases. This accessible volume was estimated by calculating the volume of the nucleotides and approximating them as spheres. In the directions parallel to the wall surfaces, periodic boundary conditions were used and the simulation box dimensions were 5.0 X 5.0 nm. The fluid was not thermostatted. The density of the bulk fluid (near the slit center) was 1.0149 g/cm^3 when there were no driving forces. In addition to water and a nucleotide, three Na^+ and one Cl^- ion were included which gave a concentration of Na^+ plus Cl^- of about 89 mM. The LAMMPS [2] program was used for the simulations and the CHARMM27 force field [3] was used to approximate the interactions between atoms. Figure 1 shows a snapshot of a typical simulation.

3. Results

Table 1 shows some statistics for the wall adsorption and desorption behavior of the nucleotides, their times of flight over a distance of 50 nm, and an estimate of the channel length required to separate the time of flight

distributions. For the equilibrium case, only the fraction of time adsorbed is relevant. Adsorption is determined based on the distance of a nucleotide from the wall or on the nucleotide-wall energy for the rough wall cases. The channel length estimate is derived by determining the overlap between the time of flight distributions, and using the fact that the width of distributions of the means is inversely proportional to the square root of the number of time of flight samples.

Table 1: Nucleotide adsorption/desorption statistics, times of flight, and estimated required channel length for 99.73% identification accuracy.

	Equil.	Body Forces: smooth walls				E: smooth walls				E: rough walls			
	f_{ads}	T	f_{ads}	n_{ads}	v_{ratio}	T	f_{ads}	n_{ads}	v_{ratio}	T	f_{ads}	n_{ads}	v_{ratio}
dAMP	0.60	77	0.63	0.179	0.29	17.5	0.48	0.061	0.51	23.8	0.24	0.066	0.38
dCMP	0.38	52	0.38	0.220	0.58	14.9	0.36	0.068	0.65	28.2	0.19	0.086	0.52
dGMP	0.68	66	0.68	0.083	0.22	18.1	0.34	0.053	0.81	26.7	0.19	0.064	0.42
dTMP	0.89	121	0.93	0.086	0.43	15.9	0.70	0.048	0.69	38.7	0.62	0.135	0.39
		Channel Length = 8.8 μm				Channel Length = 755 μm				Channel Length = 172 μm			

f_{ads} = fraction of time adsorbed to the wall, T = time of flight (ns) over 50 nm, n_{ads} = number of adsorptions per nm traveled in the driving force direction, v_{ratio} = ratio of average velocity when adsorbed to the average velocity when desorbed.

Since the times of flight for the electric field cases are different from the case with body forces, these cases cannot be compared without considering any effect that the nucleotide velocity differences may have. There is much better separation in the times of flight in the case of body forces than in the cases with an electric field, although dTMP shows better separation from the other three nucleotides when the surface is rough. The fractions of time adsorbed in the case when body forces were applied are almost the same as in the equilibrium case, but they are smaller in the case with an electric field and smooth walls. This difference may be due to the higher nucleotide velocities in the case with the electric field or due to the nature of the different driving forces. Further investigation will be required to answer this question. The rough wall further reduces the fraction of time adsorbed. The ratios of adsorbed to desorbed nucleotide velocities are larger with an electric field because the forces pushing the nucleotides are constant with an electric field which makes sliding along the wall easier. The rough surface reduces this sliding. The channel lengths required are only accurate to perhaps an order of magnitude, since they are dependent upon the tails of the time of flight distributions which may be inaccurate due to limited sampling. However, the case with the body forces clearly gives the shortest required length and the rough surface significantly reduces the length when an electric field is used.

We also considered the dynamics of the nucleotides as they adsorbed and desorbed from the walls. Since the nucleobase parts of the nucleotides consist of ring(s) and are nearly planar, axes were defined in the plane of the

nucleobases. The average angle of one of these axes with the surface plane was calculated as a function of the distance from the center of the slit for adsorption and desorption. For the purpose of these calculations, adsorption periods were defined from halfway between an adsorption point and the previous desorption point to halfway between the adsorption point and the next desorption point. Desorption was defined similarly. One of the defined axes points away from the sugar end of the nucleobases and the angle becomes negative during adsorption and desorption. This means that the sugar end adsorbs last and desorbs first. The depth of the minimum in the angle is related to the hydrophobicity of the nucleobases [4]. The hydrophobic methyl group in dTMP sticks to the wall, causing the depth of the minimum in angle to be larger.

4. Conclusions and Current Work

The following general conclusions may be drawn from this work. The nucleotides adsorbed and desorbed on nanosecond time scales even with no driving forces. This gives us confidence that a real surface can be found upon which the nucleotides do not adsorb for long periods which will reduce the potential problem of nucleotides passing each other in the nanochannel, leading to misidentification. The dynamics of the adsorption and desorption processes are related to the hydrophobicity of the base parts of nucleotides. More hydrophobic bases tilt more when coming on or off of the wall surface.

A summary of the results with driving forces follows. The estimated required channel length with smooth walls using body forces was two orders of magnitude lower than with an electric field, although the short flight times with the electric field may account for some of the difference. This is being investigated. Making the wall surface rough while using an electric field decreased the required channel length by more than four times.

Currently, the effect of electric field strength is being investigated. More realistic channel walls are also being constructed from PMMA. PMMA surface groups can be modified in experiments and in our simulations in order to study the effects of surface chemistry.

5. Acknowledgments

The current work is funded by the NSF-EPSCoR Grant # EPS-1003897 (LA-SiGMA). Computational resources were provided by LONI and HPC @ LSU. We also work with Steven A. Soper's group, which performs experimental work related to the sequencing system.

6. References

[1] H.J.C. Berendsen *et al.*, J. Chem. Phys. 81, 3684 (1984).
[2] S. Plimpton, Comput. Phys. 117, 1 (1995).
[3] N. Foloppe and A.D. MacKerell, J. Comput. Chem. 21, 86 (2000).
[4] P. Shih, L.G. Pedersen, P.R. Gibbs, and R. Wolfenden, J. Mol. Biol. 280, 421 (1998).

The intrinsic capacitance of two-dimensional electron gases

G. G. Hoffman[1], and L. R. Pratt[1]

[1]Department of Chemical & Biomolecular Engineering, Tulane University

Abstract: The quantum mechanical nature of nanoscale devices has led to the concept of quantum or intrinsic capacitance. This paper investigates the capacitance properties of a two-dimensional electron gas, paying close attention to the energetics of the system and including all interactions in the analysis. It is found that, in many ways, the two-dimensional quantum mechanical system behaves like a classical conductor. In particular, it is shown that an electric field will not penetrate the two-dimensional electron gas and that the capacitance of a two-plate capacitor made up of two-dimensional electron gases is the same as that for two classically conducting plates. The energetics of the two-dimensional electron gas, however, allows an alternate definition of the capacitance in which an intrinsic capacitance results. This intrinsic capacitance contributes in series, is large, and thus not expected to be an important component in real, physical devices.

Keywords: Quantum capacitance, intrinsice capacitance, two-dimensional electron gas

1. Introduction

The concept of quantum capacitance was first proposed in a paper by Luryi[1] in 1988. In that paper, a three-plate capacitor was devised in which the middle plate was a two-dimensional electron gas while the two outer plates where treated as classical conductors. Due to the quantum mechanical nature of the electron gas, Luryi came to the remarkable conclusion that an electric field would penetrate the middle plate, in apparent violation of classic electrostatic theory.[2] A key ingredient in that analysis was the energy dependence of the two-dimensional electron gas on the charge density, which is different from that of a classical conductor. This difference in energy properties led to a difference in capacitance properties for the device. An anomalous contribution to the capacitance was identified and labeled the *quantum capacitance*. A similar analysis was extended to the one-dimensional conductor by John, *et al.* [3]

Léonard[4] proposes a different name for this phenomenon. He discusses corrections to the classic values of the capacitance of a carbon nanotube and notes that these corrections are "not generally quantized or do not generally arise from quantization conditions". As a consequence, he favors the term *intrinsic capacitance* over *quantum capacitance*. In the interest of maintaining precision, that term will be used here as well.

Several simplifications and approximations were adopted in the analyses of Luryi[1] and John.[3] One of the more serious approximations is that "[c]orrections due to electron interactions have been neglected".[1] Since capacitance behavior is tied to the actual electric potential and thus to the interactions between charges in the system, it is important that this omission be remedied. It is, in fact, possible that this neglect could have led to the surprising predictions made. This paper presents a more careful analysis of the same system, insuring that all effects of electron interactions are represented.

2. The three-plate capacitor

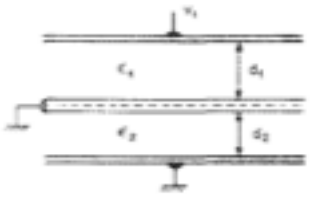

Figure 1: Diagram for the three-plate capacitor described by Luryi. Taken from reference 1.

The three-plate capacitor is presented in Figure 1, which is reproduced from Luryi's original paper.[1] Plate 1, on top, is set at a voltage, V_1. Plate 2, on the bottom, is grounded. The middle plate is referred to as a "quantum well" in Luryi's paper and is defined to be a two-dimensional electron gas. It will be labeled as plate q in this paper. Plate q is also grounded. The distance between the center plate and the upper plate is d_1 and that between the center plate and the lower plate is d_2. The spaces between the plates are filled with dielectric media with permitivities, ε_1 and ε_2. The system is treated as if it were infinite in extent in the lateral dimensions. Denote the direction perpendicular to the plates as the z-direction and let the positive z-direction point upwards (from plate 2 to plate 1) in Figure1. Then the system is invariant with respect to translations in the x,y-plane.

Some definite conclusions about this system can be made without probing the quantum mechanical nature of the middle plate. The voltage on plate 1 will generate a charge density, σ_1, on that plate. The resulting electric field will then induce a charge density on the middle plate and, potentially, also on plate 2. Let the charge density on the middle plate be denoted σ_q and that on plate 2 by σ_2. Due to the symmetry of the system, the electric field can have a non-zero component only in the z-direction. By constructing cylindrical volumes having their end surfaces perpendicular to the z-axis, the usual application of Gauss's law derive relates electric fields and these charges. If plates 1 & 2 are semi-infinite conducting slabs, then vanishing of the electric fields within those conductors implies that $(\sigma_1+\sigma_q+\sigma_2) = 0$. This condition then implies that the electric fields outside the device vanish.

The electric field in regions 1 and 2 are easily found to be $E_1 = -\sigma_1/\varepsilon_1$ and $E_2 = \sigma_2/\varepsilon_2$. Since the electric fields are independent of z in the two regions, the electric potential varies linearly in the two regions. The potential difference defined in region 1 leads to the relation $V_1 = -E_1 d_1$ and the fact that the middle and bottom plates are both grounded implies that $E_2 = 0$. The charge on the bottom plate must be zero and the electric field therefore does not penetrate the middle plate, whether it is treated as a quantum mechanical electron gas or not.

3. The two-plate capacitor

Deeper insights can be gained by considering a two-plate capacitor where *both* plates are treated as two-dimensional electron gases. The details of these considerations will be presented elsewhere. A principal consideration is the energy required to charge the parallel pair of 2D plates; analysis of that energy benefits from evaluations of energies of the two-dimensional electron gas that have been computed to a high degree of accuracy using quantum Monte Carlo methods.[5] The energy is decomposed into several analytic expressions plus a numerically computed exchange-correlation energy for which a functional fit is available. A principal conclusion is that the energy associated with the pair of charged plates relative to the neutral system contains a term which diverges unless $\sigma_1 = -\sigma_2$. If this requirement is applied, the electric field does not penetrate outside the plates. If the capacitance is defined as the ratio of the charge on one plate to the potential difference between the plates (the classic electrostatic definition), the classic result is obtained for this system, even if both plates are treated as quantum mechanical two-dimensional electron gases.

4. Intrinsic capacitance

It is possible to define capacitance alternatively in terms of the energy stored in the capacitor. By using the expressions for the energy of a two-dimensional electron gas, it is found that the capacitance of the two-plate capacitor has an additional contribution, the *intrinsic capacitance*. To summarize the principal results, the net capacitance per unit area (the *specific* capacitance) $\overline{C}_q$ is obtained as

$$\frac{1}{\overline{C}_q} = \frac{1}{\overline{C}_c} + \frac{1}{\overline{C}_i},$$

where $\overline{C}_c$ is the specific *classic* capacitance, and the specific *intrinsic* capacitance ($\overline{C}_i$) is given by

$$\frac{1}{\overline{C}_i} = \frac{2\hbar^2\pi}{m_e e^2} + \frac{2}{\sigma^2}\left\{\overline{E}_{xc}\left[\rho_0 + s\right] + \overline{E}_{xc}\left[\rho_0 - s\right] - 2\overline{E}_{xc}\left[\rho_0\right]\right\}.$$

Here σ is the charge on one plate and $s = \sigma / e$. For a pair of graphene sheets, this intrinsic capacitance can be computed (Figure 2). This intrinsic capacitance adopts values greater than 20 F/m^2. A significantly high value for the capacitance of an ultracapacitance device has been reported[6] as 1 F/m^2. The effect of the intrinsic capacitance on this would be less than 5%.

5. Conclusion

The intrinsic capacitance of a parallel plate capacitor containing two-dimensional electron gases has been carefully analyzed, taking into account all interactions in the system. It is concluded that the electric field will not

penetrate the electron gas and that the classic definition of the capacitance of the system leads to a result that is identical to that for the classical system. Defining the capacitance instead in terms of the energy of the system leads to an additional, *intrinsic* capacitance. This *intrinsic* capacitance contributes in series, is large, and is not expected to contribute significantly to the capacitance of physical devices.

6. Acknowledgments

The current work is funded by the NSF EPSCoR LA-SiGMA project under award #EPS-1003897.

7. References

[1] S. Luryi, *Appl. Phys. Lett.* **52**, 501-503 (1988).
[2] J. D. Jackson, *Classical Electrodynamics, Third Edition*, (John Wiley & Sons, Inc., New York, 1999).
[3] D. L. John, L. C. Castro, and D. L. Pulfrey, *J. Appl. Phys.* **96**, 5180-5184 (2004).
[4] F. Léonard, *The Physics of Carbon Nanotube Devices*, (William Andrew, Norwich, 2009).
[5] B. Tanatar and D. M. Ceperley, *Phys. Rev. B* **39**, 5005-5016 (1989).
[6] P. Bannerjee, I. Perez, L. Henn-Lecordier, S. B. Lee, and G. W. Rubloff, *Nature Nanotechnology* **4**, 292-296 (2009).

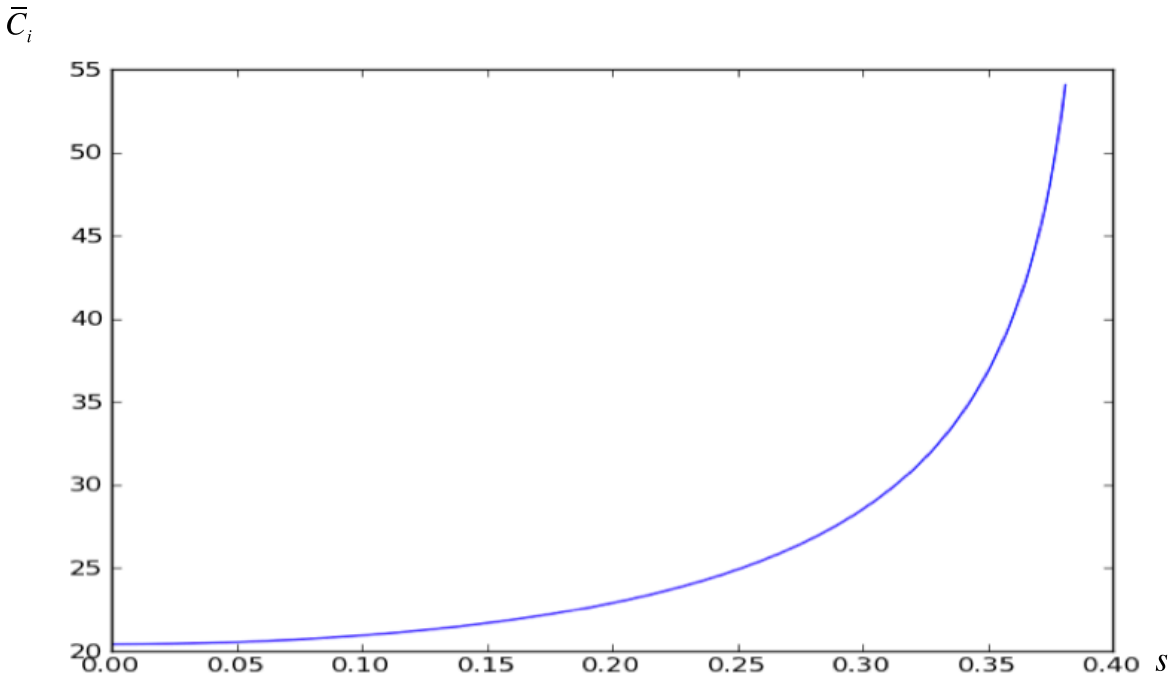

Figure 2: Intrinsic capacitance ($\overline{C}_i$, in F/m^2) of a parallel pair of graphene sheets as a function of charge (S , electrons/Å^2).

Virtual Cooperative Robots

Sanjay Kodiyalam[1], Duane Driggs[2], Sarat Paluri[2], Amitava Jana[1]

Department of [1]Mechanical / [2]Electrical Engineering, Southern University, Baton Rouge, LA 70813

Abstract: Motivated by the need to operate robots in environments not conducive for human presence a C/C++ project in Visual Studio is being developed for the display and control of Virtual Robots in the CAVE at Southern University's College of Engineering. The display, created using OpenGL, shows two robots attempting to cooperatively move a jointly held bar. The robots function in a master-slave configuration when a link's movement is selected, or both as slaves when the bar's movement is selected, for user control via a wand. When each of the two robots have six degrees of freedom they function well as a slave: being able to follow the master / user-controlled bar but not when tailored to a laboratory robot with only five degrees of freedom: Allowing one additional degree of freedom via linear base movement restores the slave's ability to follow in a limited workspace.

Keywords: Cooperative, Robot, CAVE.

1. Introduction

Cooperating robots have been envisioned in areas not conducive for human presence: For example for target searching in a war zone [1]. For task planning of cooperating robots in similar circumstances, as in bomb disposal or handling radioactive materials with more than one robot required for increasing the load carrying capacity [2], a virtual reality based approach is being developed. While such task planning for actual robots involves kinematics, dynamics, and control [2, 3], virtual task planning primarily involves only kinematics with the cooperating robots forming closed kinematic loops. The current work stereoscopically visualizes two robots in a Cave Automatic Virtual Environment (CAVE) and targets virtual task planning with the end goal of driving real robots in the Mechatronics laboratory at Southern University.

2. CAVE-Library Based Project

A generic CAVE-library [4] based project to stereoscopically visualize multiple robots with multi-axis links has been developed [5]. The primary development platform is a desktop with a single non-stereo perspective display called "CAVE simulator" and then tested in the CAVE with stereographic displays. In this project the fundamental constants of a particular robot configuration are the sizes of the links, the size of the bar to be held by the robots, the size of the robots' base, and the link angles that are fixed. The fundamental variables are the link angles that can be changed. A common data structure holds all of the constants and variables.

The CAVE library automatically spawns new synchronized threads, one for each display, in addition to the main thread that continues to operate asynchronously. The display threads also call a "navigation" routine which, in one of these threads, is for enabling navigation through the virtual world. By transforming the coordinate system of the virtual world relative to the fixed coordinate system of the CAVE the navigation routine currently provides for translations, rotations, and isotropic up/down scaling of the entire scene and eases user interaction with the virtual robots by helping in their global placement within the CAVE.

First (reference) case result [5]

In the first (reference) case, two virtual robots are operated in a master-slave configuration with the master moved directly by user input while the slave attempts to follow automatically. In this case both master and slave robot movement routines are called, in the display thread, at the end of the navigation routine. To test against arbitrary positioning of a bar by the master robot, that is to be cooperatively held by the slave while avoiding possible problems in the convergence of its movement, both robots have, in this first case, three 2-axis links *i.e.* a total of six degrees of freedom (DOF) - equal to the DOF of a sold body in three dimensions (Fig. 1 a & b). In this case it is found that the slave is able to follow the master everywhere as long as the bar is in its workspace (Fig. 1b). This cooperative movement happens "instantaneously"/interactively when the master is moved slowly – otherwise the movement of both robots "lag" the user input with differences in the bar's positioning by the two robots as evidenced by two non-overlapping displays for the bar. During this lag, as the master and slave movement routines are within the display thread, the display freezes. It results, in the CAVE, in a distortion of the perspective if the user's view is simultaneously changing. While the lag is acceptable visually as it does not lead to user frustration it illustrates that the algorithm for the slave's movement while being robust needs to be improved for better performance. It warrants a study of the magnitude of transient disagreement in the bars positioning by the two robots particularly because their motion is envisioned to eventually drive real robots in the Mechatronics laboratory.

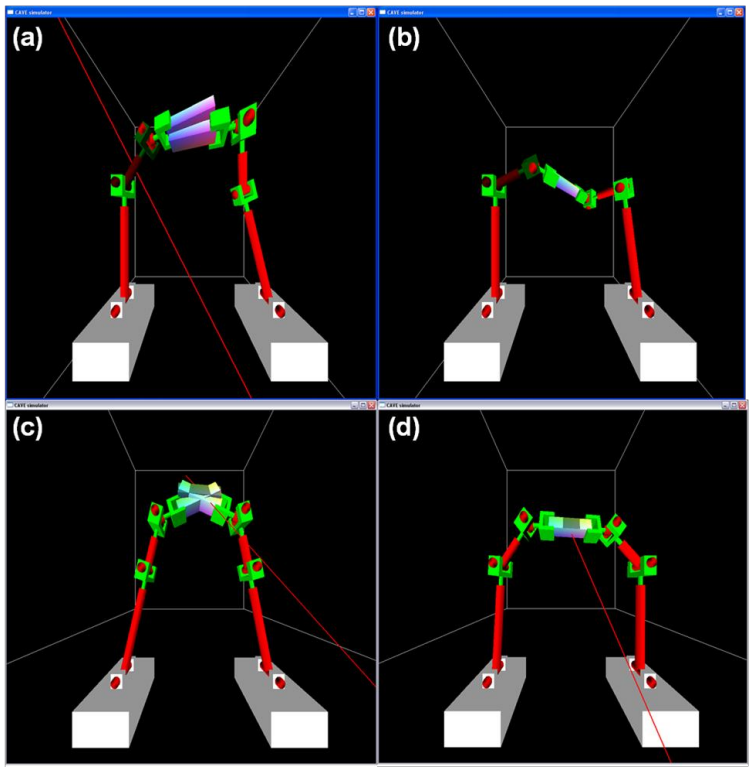

Figure 1. (a) and (b) show the reference case with robots in a master-slave configuration. (c) & (d) show the current configuration with an additional user-controlled bar. User-selection is enabled when (red) line emanating from wand intersects link / bar – that is identified in the display in dull colors. Subsequent movement of wand drives all the DOF of selected object. Disagreeing bar positions in (a) and (c) is simply to illustrate all the bars represented. (b) and (d) show perfect overlap of all the bars indicating cooperative action when user-controlled positioning of link /bar is within the workspace of the slave robot(s).

3. Project Development [6]

The virtual robot program is further developed in the following directions:

Separating robot movement and display operations

In order to avoid the freezing of the display routines moving both the master and slave have been transferred to the main thread of the CAVE library. As this thread does not have an OpenGL context code for the matrix operations required by these routines has been developed. The execution speed of this code is noticeably slower than the equivalent OpenGL code in the display thread –as evidenced with experience with the reference case configuration. Nevertheless the robot movement routines are operated in the main thread – with optimization of the matrix operations and the movement routines (particularly the slave) deferred to a later time.

Both robots as slaves to user controlled bar

For virtual task planning user control of the movement of the object cooperatively held by the robots is needed. This is accomplished with both robots serving as slaves to an independent bar – that is introduced via a robot with no links (Fig. 1 c & d). In order to translate this bar the project is modified to allow for any robot base to have translational DOF. These DOF are updated via coupling to changes in the joystick position: As the position relative to the robots changes upon navigation all positions are always evaluated in the navigated or world frame of reference. Enabling these DOF for the robot with no links and the corresponding bar's rotations enables arbitrary positioning of the bar by the user. The reference case robots, each with 6 DOF, are able to follow the bar's movements as long as the bar is within their respective workspaces (Fig. 1d).

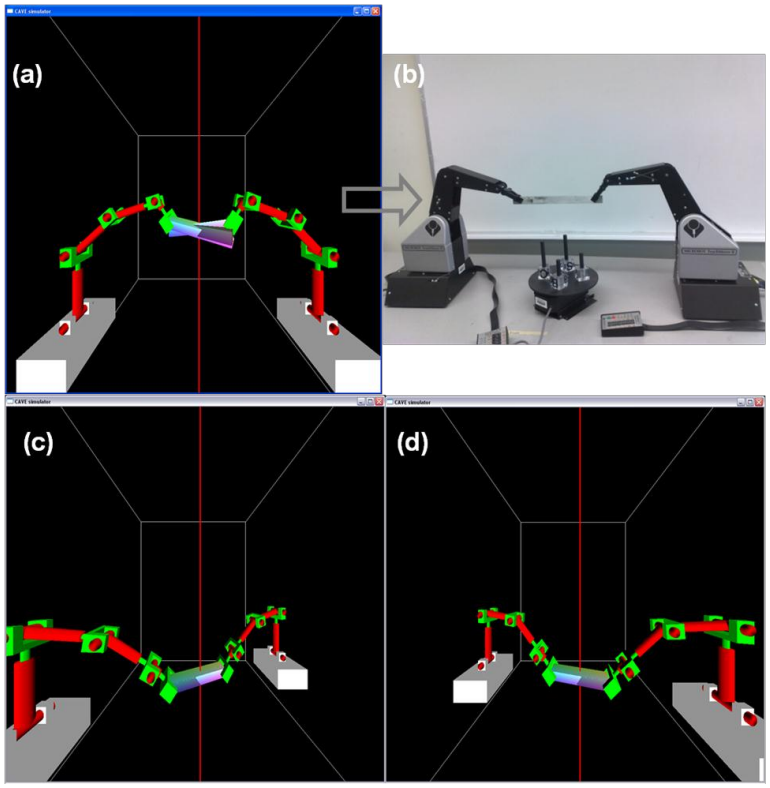

Figure 2. Virtual robots (a) tailored to Micorbots (b) by having 5 degrees of freedom (First three links with 1 DOF, last with 2 DOF), and link lengths proportional to Micorbot dimensions. (a) shows failure to follow user-controlled bar shown in dull colors. (c) and (d) illustrate successful convergence to user-controlled bar position provided the robots have an additional degree of freedom: linear base movement.

Tailoring to Laboratory robots: Convergence issues

As a first step in coupling the virtual and real worlds the virtual robots (Fig. 2a) have been tailored to two identical TeachMover II Microbots [7] (Fig. 2b) by having proportional link lengths. In this case the slave movement routine fails to converge to the users movement of the bar as each the robots have a total of only 5 DOF (Fig. 2a) – forcing the constraint of bar movement in a plane containing

the 1st link. The convergence can be achieved by having the base of the robots be movable in a direction perpendicular to their initial separation (Fig. 2 c & d): A movable base will be required for real-world applications involving movement over distances larger that in a fixed-robot workspace. Nevertheless, the domain of convergence is rather small warranting an additional DOF for the robot base.

4. Conclusions and Future Work

The VR environment of the CAVE provides a novel approach to task planning of cooperating robotic systems. The slave movement routine is to be optimized to have an acceptably small real-time strain measure of the cooperatively held bar. The virtual Microbots need to be tested for a larger domain /workspace of cooperative movement by having a base with two DOF *i.e.* with global *x-y* movement enabled. Coupling the virtual robots to and real laboratory robots is expected to reveal the advantages of this approach: As a first step the movement of a SCORBOT [8] interfaced to a computer has been modified by editing a file thereby demonstrating the possibility of file-based coupling of real and virtual robots. Subsequently dynamic coupling will be attempted with the virtual and real worlds linked over using network-based software analogous to that proposed in remote laboratory experiments [9].

5. Acknowledgement

Ongoing work is supported by LA-SiGMA (NSF EPS-1003897). The Center for Energy and Environmental Studies at Southern University is acknowledged for supporting hardware upgrades to the CAVE.

6. References

[1] Adam Ray, "Cooperative Robotics Using Wireless Communication," Master's Thesis, Auburn University, (2005).

[2] A. Jana, D. M. Auslander, R. N. Dave, S. S. Chehl, "Task Planning for Cooperating Robot Systems," *Proceedings of the First World Automation Congress*, Maui, Hawaii, (1994).

[3] H. P. Huang, and R. S. Chen, "Modelling and Adaptive Coordination control of a Two-robot System," *Journal of Robotic Systems*, 9 (1), 65-92, (1992).

[4] Dave Pape, Carolina Cruz-Neira, Marek Czernuszenko, *CAVE Library version 2.6*, Electronic Visualization Laboratory, University of Illinois at Chicago, (1997). Currently used: Version 3.2, CAVELib™, Mechdyne Corporation, Marshalltown, Iowa.

[5] D. Driggs, S. Baylor, B. M. S. Kuppala, S. Kodiyalam, K. Sekeroglu, A. Jana, "From Virtual to Laboratory Robots," *Proceedings of the 2011 ASEE-GSW Conference*, March 2011, Houston, Louisiana, Session FC1-1.

[6] IMETI

[7] D. Eavey, "Robotic Workcells and System Interfacing," *UMI-MICROBOT*, 1, UMI-MICROBOT Inc., Sunnyvale, CA, (1988). Currently used: Teachmover II, Questech Inc,

[8] *SCORBOT*, Intelitek Inc., Manchester, New Hampshire.

[9] S. Paluri, K. Sekeroglu, M. H. Yilmaz, A. Jana, "Web-based Experimentation for Efficient Learning," *Proceedings of the 2011 ASEE-GSW Conference*, March 2011, Houston, Louisiana, Session FC1-1, Pgs:1-6.

2011 Symposium Registered Attendees

Last name	First name	Affiliation
Abu Asal	Sameer	Louisiana State University
Ashbaugh	Henry	Tulane University
Bagayoko	Diola	Southern University and A&M College
Bishop	Thomas	Tulane University
Borill	Brandon	Louisiana State University
Butler	Les	Louisiana State University
Carman	Kevin	Louisiana State University
Chanda	Dipon	Louisiana State University
Chen	Bin	Louisiana State University
Davidson	Kerry	Louisiana Board of Regents
Derosa	Pedro	Grambling State/Louisiana Tech
Devireddy	Ram	Louisiana State University
DiTusa	John	Louisiana State University
Domingue	Jessica	Louisiana Board of Regents
Dunn	Cindi	Office of Educational Innovation and Evaluation- Kansas State University
Ekuma	Chinedu	Louisiana State University
Fattah	Kasra	Louisiana State University
Goloverda	Galina	Xavier University of Louisiana
Grayson	Scott	Tulane University
Guice	Leslie	Louisiana Tech University
Hall	Randall	Louisiana State University
Han	Fei	Louisiana Tech University
Henry	Laurence	Southern University and A&M College
Hilgendorf	Amy	Office of Educational Innovation and Evaluation- Kansas State University
Jarrell	Mark	Louisiana State University
Jernigan	Susan	Louisiana Board of Regents
Jones	DiOnetta	Massachusetts Institute of Technology
Joseph	Grace	Louisiana Tech University
Khonsari	Michael	Louisiana Board of Regents
King	Amber	Louisiana Board of Regents
Kiruri	Lucy	Louisiana State University
Kodiyalam	Sanjay	Southern University and A&M College
Kolesnichenko	Vladimir	Xavier University of Louisiana
Kucheryavy	Pavel	Xavier University of Louisiana
Kurnosov	Arkady	Tulane University
Lama	Meera	Louisiana Tech University
Lange	Shelia Edwards	University of Washington

Lee	Shelley	Louisiana State University
Lester Jr.	William A.	University of California, Berkeley
Li	Guoqiang	Southern University and A&M College
Lin	Jieqiong	Louisiana State University
Liu	Lixin	Tulane University
Liu	Shuai	Tulane University
Lvov	Yuri	Louisiana Tech University
Mainardi	Daniela	Louisiana Tech University
Mao	Zhiqiang	Tulane University
McFerrin	Cheri	Louisiana State University
McKoy	Vince	California Institute of Technology
Moldovan	Dorel	Louisiana State University
Moreno	Juana	Louisiana State University
Mukherjee	Rajib	Louisiana Tech University
Novak	Brian	Louisiana State University
Paluri	Sarat	Southern University and A&M College
Paudyal	Anjana	Louisiana Tech University
Perdew	John	Tulane University
Pesika	Noshir	Tulane University
Podduturi	Vishwa Priya	Louisiana Tech University
Poobal	Karthik	Louisiana Board of Regents
Pratt	Lawrence	Tulane University
Rajagopalan	Kaushik	Louisiana State University
Ramachandran	Ramu	Louisiana Tech University
Ramanujam	Jagannathan	Louisiana State University
Ranjitkar	Neelima	Louisiana Tech University
Rick	Steve	University of New Orleans
Roth	Judy	Office of Educational Innovation and Evaluation- Kansas State University
Ruzsinszky	Adrienn	Tulane University
Sabliov	Cristina	LSU Agricultural Center
Sekeroglu	Kazim	Southern University and A&M College
Silverman	Harold	Retired
Sinnott	Susan B.	University of Florida
Soto	Fernando	Louisiana Tech University
Spinu	Leonard	University of New Orleans
Stevens	Cheryl	Xavier University of Louisiana
Teamer	Dwayne	Louisiana Tech University
Thakur	Bhupender	Louisiana State University - CCT
Townsend	Leigh	Louisiana State University
Wang	Yi	Tulane University
Whaley	Meocha	Louisiana State University

Whittenburg	Scott	University of New Orleans
Wick	Collin	Louisiana Tech University
Xia	Kai	Louisiana State University